seit 1558

NUMERICAL SOLUTION TO THE EINSTEIN-MAXWELL EQUATIONS OF A ROTATING DISC OF CHARGED DUST

Numerische Lösung der Einstein-Maxwell-Gleichungen
für eine rotierende und geladene Staubscheibe

Dissertation
zur Erlangung des akademischen Grades
doktor rerum naturalium (Dr. rer. nat.)

vorgelegt dem Rat der Physikalisch-Astronomische Falkultät
der Friedrich-Schiller-Universität Jena

von Diplom Physikerin Yu-Chun Pynn (geb. Liu)
geboren am 08.11.1982 in Tainan City, TAIWAN

Jena, 26. Mai 2017

Gutachter

1. **Prof. Dr. rer. nat. habil. Reinhard Meinel**
   Theoretisch-Physikalisches Institut
   Friedrich-Schiller-Universität Jena

2. **Dr. rer. nat. habil. David Petroff**
   Zentrum für Klinische Studien
   Universität Leipzig

3. **Prof. Dr. rer. nat. habil. Wilhelm Kley**
   Institut für Astronomie und Astrophysik
   Eberhard Karls Universität Tübingen

Datum der Verteidigung: 15. Januar 2019

Contents

Summary **i**

Zusammenfassung **iii**

1 Introduction **1**

2 The Einstein-Maxwell Equation **5**
- 2.1 Field equations 5
- 2.2 Rotating charged fluid 7
- 2.3 Derivation of the field equations 8
  - 2.3.1 Tetrad basis 8
- 2.4 Boundary conditions 10
  - 2.4.1 Symmetry properties of the fields 10
  - 2.4.2 Derivation of the Boundary Conditions 11
- 2.5 Parameter Space (γ, ε) 14

3 Numerical Treatment **17**
- 3.1 Pseudo-Spectral Method 17
  - 3.1.1 Overview 17
  - 3.1.2 Compactification 18
  - 3.1.3 Newton-Raphson Method 20
- 3.2 Rescaling the potential 22
  - 3.2.1 Equation System 22
  - 3.2.2 Initial Guess 24
  - 3.2.3 Vector Field 26
  - 3.2.4 Analytical Mesh-Refinement 27

4 Physical Quantities and Ergosphere **29**
- 4.1 Physical Quantities 29
  - 4.1.1 Far Field Behaviour 29
  - 4.1.2 Normalising the physical quantities through Ω and ρ_0 31
  - 4.1.3 Parameter Relation and Error 34
  - 4.1.4 Gyromagnetic Factor g 34
- 4.2 Ergosphere 35
  - 4.2.1 Bisection Method 36

5 Results **39**
5.1 Fields $\tilde{\nu}$, $\tilde{\omega}$, A_φ and $\tilde{A}_t$ 39
5.2 Angular Velocity Ω 42
5.3 Physical Quantities 42
5.4 Error Calculation 44
5.5 Gyromagnetic Factor g 50
5.5.1 Post-Newtonian expansion for the gyromagnetic factor 51
5.5.2 Numerical Calculations for the gyromagnetic factor 53
5.5.3 Support and Comparison 53
5.6 Ergosphere 56

6 Conclusion and Outlook **61**

Appendices **65**

A Detailed Calculation to the Field Equations **67**
A.1 Overview 67
A.1.1 Einstein Equation 67
A.1.2 Maxwell Equation 68
A.1.3 Different Reference of Frame 68
A.1.4 Mathematica Code 69
A.2 Results 72
A.2.1 Obtained Directly through the Metric 72
A.2.2 Obtained via Tetrad-Basis 73

B Detailed calculations of the boundary conditions **75**
B.1 Pill-box integration on the disc 75
B.1.1 Difference between the pill-box integration and the "conventional" integration 75
B.1.2 Pill-box integration for the disc 76

C Potential and coordinate transformation **81**
C.1 Potential transformation 81
C.1.1 For $\tilde{\nu}$ and $\tilde{\alpha}$ 81
C.1.2 For $\tilde{\omega}$ and $\tilde{A}_t$ 81
C.2 Coordinate transformation 82

D Table of the data points of the appearance of the ergosphere **85**

Bibliography **87**

Ehrenwörtliche Erklärung **90**

Acknowledgements **92**

Curriculum Vitae and Publications **94**

Summary

In this work, the numerical solution of the Einstein-Maxwell equations of a rotating disc of charged dust and the extended application on its solution results are presented.

Firstly, the theoretical background of the Einstein-Maxwell equations and how they are formed into the field equations for the rotating charged fluid are discussed. The Lewis-Papapetrou metric provides the stationary and the axial-symmetric characters, while the energy-momentum tensor adds the electromagnetic and rotation factor into the system. The boundary conditions, which are derived subsequently from the field equations, provide the disc character. Combining the field equations and the boundary conditions yields an equation system describing a rotating disc of charged dust, which is subsequently solved by the numerical approach of the pseudo-spectral method.

A brief introduction of the pseudo-spectral method is given, followed by the demonstration of how the method is adapted to the model. This is accompanied by an explanation of the algorithm used to solve this specific field equation system. Further discussion of the improvement on the calculation speed, such as the analytical mesh-refinement is also included.

The outcome of the equation system consists of raw potential data and some additional byproducts such as the angular velocity obtained from the extra auxiliary equations of the system. The raw data are processed into a more straightforward and intuitive physical quantities, which can further be utilised to analyse the gyromagnetic character of the system. The gyromagnetic factor serves as an interesting outlook towards both the relativistic and quantum mechanic regions. Lastly, using the raw data, the ergosphere surface can be obtained by acquiring the zero point of the metric element g_{tt} using the bisection method.

All the results are summarised in the final chapters of this work. The discussion covers the whole parameter space (γ, ε): from the classical limit $\gamma \ll 1$ to the black hole limit, which approaches the Kerr-Newman solution from the external point of view $\gamma \to 1$, and from the non-charged limit $\varepsilon = 0$ to the electrical counterpoised limit $\varepsilon \to 1$.

The raw data and the auxiliary potentials are first compared under different degrees of relativistic parameter γ or specific charge density ε. The physical quantities are furhter presented from both the near-source and far-field perspectives, along with the treatment of the error calculation of the system. A detailed discussion of the gyromagnetic factor and different methods of its acquisition are compared. The configuration of the ergosphere surface is presented, as observed from both the near-source and far-field perspectives, under different charge and relativistic magnitudes. A complete survey from the point at which the ergosphere starts appearing is discussed, covering the whole parameter space (γ, ε). Possible further development of this work, such as its application to the differential rotation case, is discussed in the final chapter.

Zusammenfassung

Diese Arbeit untersucht die numerische Lösung der Einstein-Maxwell-Gleichungen für eine rotierende und geladene Staubscheibe. Die gewonnenen Ergebnisse werden in der Anwendung präsentiert.

Zunächst wird der theoretische Hintergrund der Einstein-Maxwell-Gleichung und deren Übertragung auf die Staubscheibe dargestellt. Die Lewis-Papapetrou-Metrik liefert die stationären und axialsymmetrischen Eigenschaften, während der Energie-Impuls-Tensor die Rotation und den elektromagnetischen Faktor in das System einfügt. Die Randbedingungen, die allmählich aus den Feldgleichungen abgeleitet werden, liefern die Scheibeneigenschaft. Aus der Kombination der Feldgleichungen und der Randbedingungen ergibt sich ein Gleichungssystem, das eine geladene rotierende Staubscheibe beschreibt und anschließend durch die Pseudo-Spektrale Methode gelöst wird. Zunächst wird die Pseudo-Spektrale-Methode in einer kurzen Einführung erklärt. Die darauf folgende Darstellung zeigt, wie die Methode an das Model angepasst wird. Gleichzeitig wird der für die Lösung dieses spezifischen Feldgleichungsystems verwendete Algorithmus erläutert. Eine weitere Diskussion zur Verbesserung der Berechnungsgeschwindigkeit, z.B. über die analytischen Gitterverfeinerung, ist ebenfalls enthalten.

Das Ergebnis des Gleichungssystems besteht aus Rohdaten und einigen zusätzlichen Nebenprodukten, wie der Winkelgeschwindigkeit, die aus den zusätzlichen Hilfsgleichungen des Systems gewonnen werden. Die Rohdaten werden in überschaubarere und intuitivere physikalische Größen verarbeitet. Diese können weiter genutzt werden, um den gyromagnetischen Charakter des Systems zu analysieren. Der gyromagnetische Faktor liefert einen interessanten Blick auf die relativistischen und quantenmechanischen Bereiche. Schließlich werden für den Erhalt der Ergosphärenoberfläche die Rohdaten in das metrische Element g_{tt} eingesetzt, und die Nullpunkte des g_{tt} nach dem Bisektionsverfahren erworben.

Alle Ergebnisse werden in den letzten Kapiteln dieser Arbeit zusammengefasst. Die Diskussion umfasst den gesamten Parameterraum (γ, ε): Vom klassischen Grenzfall $\gamma \ll 1$ bis zum extreme Kerr-Newman-Grenzfall $\gamma \to 1$, vom äußeren Standpunkt aus gesehen; als auch vom nicht geladenen Fall $\varepsilon = 0$ bis zur extrem geladenen Konfiguration $\varepsilon \to 1$.

Die Rohdaten und die Hilfspotentiale werden zunächst unter verschiedenen Ausmaßen des relativistischen Parameters γ und der spezifischen Ladungsdichte ε verglichen. Die physikalischen Größen werden nun aus der Nah- und Fernfeldperspektive dargestellt, gleichzeitig dienen sie der Behandlung der Fehlerberechnung des Systems. Eine detaillierte Diskussion zum gyromagnetischen Faktor und verschiedene Methoden seiner Akquisition werden verglichen. Schließlich wird die Konfiguration der Ergosphärenoberfläche aus der Nah- als auch Fernfeldperspektive unter verschiedenen Größen von γ und ε dargestellt. Die jeweilige Auftrittsstelle der Ergosphäre wird im gesamten Parameterraum vollständig untersucht. Eine mögliche Weiterentwicklung dieser Arbeit, z.B. die Anwendung auf den Differentialrotationsfall, wird im letzten Kapitel diskutiert.

Chapter 1

Introduction

Many of our celestial bodies have a disc-like configuration, especially those of the disc galaxies, which consist of a thick or thin disc, and often might contain a galactic nuclear bulge or some surrounding globular clusters. Different approaches have been used in order to simulate and understand more about the spacetime and physical characteristics of the disc-like celestial configurations. As well as observational investigations, theoretical studies, both analytically and numerically have been carried out for decades. The studies began with simpler structures, to which more factors were added so as to model more astrophysical-like systems.

Studies on uniformly rotating discs began in 1969 [1, 2]. Since then, simulations and comparisons of similar or more complicated models have been investigated, with the hope of providing more insight into the actual astrophysical objects.

From the early 90's, a series of research articles on rigidly rotating disc of dust were published, beginning with analytical studies of the boundary value problem formed into the Ernst equation and solved using inverse scattering methods [3, 4, 5, 6, 7]. These were followed by numerical studies with geodesic motion around the disc [8], the calculation of non-rigid rotating discs [9, 10] and the application with respect to the black hole limits [11]. Additionally the investigations via post-Newtonian approaches [12] and multiple moment [13] also provided another perspective on the topic.

In this work, we go a step further by adding the electromagnetic factor to the rotating disc model. The system thus become a charged rotating disc in electrovacuum. Post-Newtonian methods towards the model were provided for the model [14, 15]. We used the numerical approach for this work, in the hope that it might provide another basis for future studies on the analytical aspect, and furthermore for more complicated disc structures, for example, when including the surrounding globular structure (non-electrovacuum) or the nuclear bulge (quasi-disc like) into the system. As such the approach will tend towards the astrophysical-like configuration.

In this work, our aim is to solve the Einstein-Maxwell field equations of the rotating disc of charged dust using the numerical approach of the pseudo-spectral method, and discuss the outcome of the solution by transforming the direct raw field result into a more intuitive physical properties and aspects.

In Chapter 2, the theoretical background of the model, the derivation of the Einstein-Maxwell equations and the boundary conditions for our disc of charged dust applying the orthonormal tetrad basis, are discussed. The raw potentials used in the work are ν, ω and α, different from the use of U, a and k in the analytical work, since for the analytical work, the field equations were transformed into Ernst equation for further investigations, whereas in this work, the divergence of the fields in the region of the ergosphere can be avoided using the terms ν, ω and α. The outcome of the equation system can be neatly separated into the fluid part and the charged part. The fluid part is exactly the non-charged field equations, which have been thoroughly investigated both analytically and numerically as mentioned above. In this work, the discussion is extended to consider the charged fluid case using the numerical approach. The discussion covers the entire parameter space (γ, ε). The relativistic parameter γ represents the degree of relativity, $\gamma \ll 1$ in the classical Newtonian limit, and $\gamma \to 1$ to the ultra-relativistic or black hole limit, whereas the constant specific charge ε represents the intensity of the electromagnetism, with $\varepsilon = 0$ representing the non-charged case, to $\varepsilon \to 1$ to the electrically counterpoised dust (ECD) case.

Chapter 3 considers the numerical procedure used for solving the field equations. The pseudo spectral method is introduced and algorithms of the numerical technique are discussed. The equation system is adapted and applied to the numerical treatment. The communication between the model and the method are linked between a series of field and coordinate transformations, and the field equations and the boundary conditions are converted into the C-language algorithm. Additionally, due to the high gradient configuration of the raw field in the ultra-relativistic region, the analytical mesh-refinement method is introduced to prevent the algorithm from diverging at high γ's.

After the field solutions are obtained from the equation system via the numerical treatment, the raw field data are converted into more intuitive physical properties. Chapter 4 serves as a preparation for the discussion of the results presented the proceeding chapter, in which the quantities such as mass M, angular momentum J, magnetic dipole moment μ_B and charge Q, and how they are derived and applied from the data field, are discussed. The physical quantities can be further utilised to serve as an error inspection towards the calculation of the system, when combined with the parameter relation. The physical quantities, though remaining the same intrinsically, exhibit different configurations depending on the perspective of the observer. In other words, the normalisation of the system from the point of view of the observer must also be considered. The gyromagnetic factor g derived from the physical properties is also discussed. In many relativistic and quantum systems, there exists an interesting common characteristic: $g = 1$ in the Newtonian limit $\gamma \ll 1$, and $g = 2$ in the ultra-relativistic limit $\gamma \to 1$. The system described here will be inspected to see if this phenomenon also applies. This may in turn provide insight into the connection between the relativistic and quantum systems. Next, the possible tools needed to find the ergosphere of the system is discussed. The non-charged case has been inspected [16], the discussion of which is extended to the charged case.

Finally in chapter 5, the result of the work are presented by first exhibiting the raw data field ν, ω, A_φ and A_t, and comparing them with the known non-charged case. The raw data are transformed into the more intuitive physical quantities in the entire parameter space, and the properties are inspected at different γ's and ε's. Angular velocity Ω, being an unknown parameter in the field equation system, is solved together with the raw data. Its result is also presented, since Ω serves as a useful normalisation tool. The error distribution derived from the physical quantities is looked into, in order to be used as a control, not just for the result of the calculations, but also for the whole equation system setting. The gyromagnetic factor is investigated in detail, and compared with some known results and extended to the unknowns, especially at the ultra-relativistic region. The outcome of the ergosphere is presented at the end of chapter, and its configuration is shown in different regions of the parameter space. The criteria of when the ergosphere starts appearing relating to the level of relativistic and electromagnetic effect is also elegantly presented. Part of the result in this chapter is published in [17].

The work presented in this thesis uses the notation $G = c = 1$.

Chapter 2

The Einstein-Maxwell Equation

In this chapter, it is shown how the field equations and the boundary conditions for the model of rigidly rotating disc of charged dust is obtained. The field equations describing the spacetime distortion and electromagnetic field of the rotating disc of charged dust are expressed through the Einstein equation and the Maxwell equation.

Firstly, the Einstein and Maxwell field equations are discussed in general, after which focus is given to the rotating charged fluid by introducing the energy-momentum tensor and the corresponding four-velocity. Lastly, the disc character is introduced when dealing with the boundary conditions.

In the second part of this chapter, in preparation for the results presented in the coming chapters, parameters or variables that govern the physical characteristics of the system, such as the relativity parameter γ, specific charge parameter ε, the angular velocity Ω are discussed.

2.1 Field equations

Einstein equation

The Einstein field equation characterises the spacetime distortion created by the gravitational and electromagnetic influence of a source

$$R_{ik} - \frac{1}{2} R g_{ik} = 8\pi T_{ik}, \tag{2.1}$$

where the energy-momentum tensor T_{ik} governs the characteristics of the source, which will be discussed in the next section.

Additionally, by multiplying the Einstein equation with g^{ik},

$$\begin{aligned} g^{ik} R_{ik} - \frac{1}{2} g^{ik} g_{ik} R &= 8\pi g^{ik} T_{ik}, \\ R - \frac{4R}{2} &= 8\pi T, \end{aligned}$$

the trace equation

$$R = -8\pi T, \tag{2.2}$$

is obtained, where R is the Ricci scalar and T is the trace of the energy-momentum tensor.

Maxwell equation

The Maxwell equation describes the electromagnetic field produced by a source

$$F^{ik}{}_{;k} = 4\pi \jmath^i, \tag{2.3}$$

with the electromagnetic tensor

$$F_{ik} = A_{k,i} - A_{i,k}, \tag{2.4}$$

A_k being the four-potential(vector potential), and with the purely convective[1] four-current density

$$\jmath^i = \rho_{el} u^i, \qquad \rho_{el} = \varepsilon\mu, \tag{2.5}$$

with the mass density μ, the four-velocity u^i, and ρ_{el} being the charge density, a constant specific charge $\varepsilon \in [-1, 1]$ is assumed.

Lewis-Papapetrou metric

The spacetime of a stationarily rotating and axisymmetric perfect fluid body can be expressed through the Lewis-Papapetrou-Weyl metric [18, 19]

$$ds^2 = e^{2\alpha}(d\rho^2 + d\zeta^2) + \rho^2 e^{-2\nu}(d\varphi - \omega dt)^2 - e^{2\nu} dt^2. \tag{2.6}$$

Note that in the past work, most discussions were based on the (2.6) equivalent metric

$$ds^2 = e^{-2U}\left[e^{2k}(d\rho^2 + d\zeta^2) + \rho^2 d\varphi^2\right] - e^{2U}(dt - a d\varphi)^2, \tag{2.7}$$

which can be converted into the Ernst equation for analytical purposes [20, 21, 22].

The relationships between ν, ω, α and U, a, k are

$$e^{2U} = e^{2\nu} - \rho^2\omega^2 e^{-2\nu}, \tag{2.8}$$

$$a = \frac{\rho^2\omega}{e^{4\nu} - \rho^2\omega^2}, \tag{2.9}$$

$$\alpha = k - U, \tag{2.10}$$

With the fields U, a and k, one has to pay attention to the fact that inside the ergosphere where $e^{2U} < 0$, U is no longer a real function. Moreover, at the ergosphere's boundary where $e^{2U} = 0$, the field a tends to go to infinity. The reason why the solution still converges is because the field a is always coupled with U. Yet, choosing the metric with fields μ, ω and α avoids the ergosphere problem, since comparing the metric element g_{tt} of the two metrices in (2.8), there always exist a solution $e^{2\nu} = \frac{1}{2}\left(e^{2U} + \sqrt{e^{4U} + 4\rho^2\omega^2}\right) > 0$, which keeps ν a real function, even inside the ergosphere where $e^{2U} < 0$.

---

[1] The mass and charge elements have equal velocities.

2.2 Rotating charged fluid

Energy-momentum tensor

The energy-momentum tensor describes the source distribution and the characteristic of the material. For the perfectly charged fluid, the energy-momentum tensor is

$$T_{ik} = {T_{ik}}^{(fluid)} + {T_{ik}}^{(em)}, \tag{2.11}$$

with the fluid part

$${T_{ik}}^{(fluid)} = (\mu + p)u_i u_k + p g_{ik}, \tag{2.12}$$

where μ is the mass-energy density and p is the pressure. The electromagnetic part of the energy-momentum tensor is

$${T_{ik}}^{(em)} = \frac{1}{4\pi}\left(F_{ij}{F_k}^j - \frac{1}{4\pi}F^{mn}F_{mn}g_{ik}\right). \tag{2.13}$$

As shown in (2.4), the electromagnetic tensor F_{ij} can be charaterised by the partial derivative of the vector potential $A_{i,k}$. Due to the axial symmetry, the vector potential can be put in the form

$$\mathbf{A} = A_\varphi(\rho, \zeta)d\varphi + A_t(\rho, \zeta)dt.$$

Four velocity

For the stationary axialsymmetric rotating fluid, the four-velocity is

$$u^i = e^{-V}(\xi^i + \Omega\eta^i), \tag{2.14}$$

where ξ^i and η^i are the Killing vectors representing the stationarity and and axisymmetry respectively.

$$\xi^i = \delta^i_t, \quad \eta^i = \delta^i_\varphi.$$

Expressed in terms of the metric (2.6), the scalar products of the Killing vectors are thus

$$\xi^i\xi_i = g_{tt} = -e^{2\nu} + \omega^2\rho^2e^{-2\nu}, \tag{2.15a}$$
$$\eta^i\eta_i = g_{\varphi\varphi} = \rho^2e^{-2\nu}, \tag{2.15b}$$
$$\xi^i\eta_i = g_{t\varphi} = -\omega\rho^2e^{-2\nu}, \tag{2.15c}$$
$$\eta^i\xi_i = g_{\varphi t} = -\omega\rho^2e^{-2\nu}. \tag{2.15d}$$

As such the scalar product of the four-velocity is

$$u^iu_i = -c^2, \tag{2.16}$$

where $c = 1$ is the notation we use in this work. Combining (2.14) and (2.16), we have

$$e^{2V} = -\left(\xi^i + \Omega\eta^i\right)\left(\xi_i + \Omega\eta_i\right),$$

and together with (2.15a)-(2.15d), we get

$$e^V = e^\nu\sqrt{1 - \left[\frac{\rho}{e^{2\nu}}(\Omega - \omega)\right]^2}. \tag{2.17}$$

Angular velocity Ω

Ω is the angular velocty of the disc observed from infinity, with

$$\Omega = \frac{d\varphi}{dt} = \frac{u^{\varphi}}{u^{t}}.$$

Note: when discussing the rotating disc of charged dust, it can both be rigidly rotating or, since this work does not need to be done under the co-rotating frame such as that in [14] or [15], the model does not have to be narrowed to the rigidly rotating case, i.e. the angular velocity does not have to be restricted to be constant $\Omega = constant$[2], but can instead leave the disc the freedom of differential rotating $\Omega(\rho)$.

Disc configuration

The disc characteristic is later introduced, when the pill-box integration is adopted into the boundary conditions to the field equations. In the section below, the derivation of the field equations is discussed after which, the boundary conditions that satisfy the model of the rotating disc of charged dust are introduced.

2.3 Derivation of the field equations

2.3.1 Tetrad basis

The field equation is derived under the orthonormal tetrad basis (The basis that represents the frame of reference of the local Lorentz observer) using the transformation [2]

$$\lambda_{(\rho)}{}^{\hat{i}} = e^{-\alpha}\delta^{\hat{i}}_{(\rho)}, \quad \lambda_{(\zeta)}{}^{\hat{i}} = e^{-\alpha}\delta^{\hat{i}}_{(\zeta)}, \quad \lambda_{(\varphi)}{}^{\hat{i}} = \frac{e^{\nu}}{\rho}\delta^{\hat{i}}_{(\varphi)}, \quad \lambda_{(t)}{}^{\hat{i}} = e^{-\nu}\delta^{\hat{i}}_{(t)} + \omega e^{-\nu}\delta^{\hat{i}}_{(\varphi)}, \tag{2.18}$$

where " ˆ " indicates the index of the tetrad basis.

The Lewis-Papapetrou-Weyl metric describing the spacetime of a stationarily rotating and axisymmetric perfect fluid body

$$ds^2 = e^{2\alpha}(d\rho^2 + d\zeta^2) + \rho^2 e^{-2\nu}(d\varphi - \omega dt)^2 - e^{2\nu}dt^2,$$

will be turned into the orthonormal tetrad basis

$$ds^2 = dx_1^2 + dx_2^2 + dx_3^2 - dt^2$$

after the tetrad transformation.

---

[2] Only when working under the co-rotating frame does one have to assume that the disc is rigidly rotating, since the co-rotating frame (denoted with " ′ ") is defined as

$$\rho' = \rho, \quad \zeta' = \zeta, \quad \varphi' = \varphi - \Omega t, \quad t' = t,$$

where Ω is the constant angular velocity.

The field equations obtained directly through the metric and obtained via the tetrad basis only differ from the point of view of the observers, but the tetrad basis simplifies the configuration of the field equations. Whilst the field equations obtain directly through the metric are being regarded from the point of view of the distant observer, the field equations obtained via the tetrad basis are being regarded from the point of view of the local Lorentz observer.

This is supported by the calculation of the Ricci scalar, which should be invariant from the frame of reference. As shown in Appendix A, by calculating the Ricci scalar using the two basis independently, the same result is obtained.

The Einstein equation (2.1) and the Maxwell equation (2.3) under the tetrad basis[3] become(See the detailed derivation of the field equations in the Appendix A.)

Einstein $[\hat{4},\hat{4}]$:

$$\Delta\nu - \frac{1}{2}\rho^2 e^{-4\nu}(\nabla\omega)^2 - 4\pi e^{2\alpha}(\mu+p)\left[\frac{1+v^2}{1-v^2}\right] + \frac{1}{\rho^2}e^{-2\nu}\left[e^{4\nu}(\nabla A_\varphi)^2 + \rho^2(\nabla A_t + \omega\nabla A_\varphi)^2\right] = 0, \tag{2.19}$$

Einstein $[\hat{3},\hat{4}]$:

$$\nabla\cdot(\rho^2 + e^{-4\nu}\nabla\omega) + 16\pi\rho e^{2(\alpha-\nu)}\left[(\mu+p)\frac{v}{1-v^2} + 2p\right] - 4e^{-2\nu}\left[\nabla A_\varphi\nabla A_t + \omega(\nabla A_\varphi)^2\right] = 0, \tag{2.20}$$

Maxwell $[\hat{3}]$:

$$-\frac{4e^{2\alpha-3\nu}\pi\varepsilon\rho^2\mu(\Omega-\omega)}{\sqrt{1-e^{-4\nu}\rho^2(\Omega-\omega)^2}} + e^{-4\nu}\rho^2\left[\nabla A_t\nabla\omega + \omega(\nabla A_\varphi\nabla\omega)\right] - 2\nabla A_\varphi\nabla\nu - \Delta A_\varphi + \frac{2A_{\varphi,\rho}}{\rho} = 0, \tag{2.21}$$

Maxwell $[\hat{4}]$:

$$-\frac{4e^{2\alpha+\nu}\pi\varepsilon\mu}{\sqrt{1-e^{-4\nu}\rho^2(\Omega-\omega)^2}} - 2\nabla A_t\nabla\nu - 2\omega\nabla A_\varphi\nabla\nu + \nabla A_\varphi\nabla\omega + \Delta A_t + \omega\Delta A_\varphi = 0. \tag{2.22}$$

where

$$v := \rho e^{-2\nu}(\Omega-\omega).$$

As one can see, even though the charged field equations have a more complex configuration, they can be neatly separated into the fluid part and the charged part. The fluid part is exactly the non-charged case and has been discussed and investigated thoughly.

In the dust case where $p = 0$ and the exterior of the disc being electro-vacuum $\mu = 0$,

---

[3] Einstein $[\hat{i},\hat{k}]$ denotes $R_{\hat{i}\hat{k}} - \frac{1}{2}Rg_{\hat{i}\hat{k}} = 8\pi T_{\hat{i}\hat{k}}$, and Maxwell $[\hat{i}]$ denotes $F^{\hat{i}\hat{k}}{}_{;\hat{k}} = 4\pi j^{\hat{i}}$.

(2.19)-(2.22) are reduced to

$$\Delta\nu - \frac{1}{2}\rho^2 e^{-4\nu}(\nabla\omega)^2 + \frac{1}{\rho^2}e^{-2\nu}\left[e^{4\nu}(\nabla A_\varphi)^2 + \rho^2(\nabla A_t + \omega\nabla A_\varphi)^2\right] = 0, \tag{2.23}$$

$$\nabla\cdot(\rho^2 e^{-4\nu}\nabla\omega) - 4e^{-2\nu}\left[\nabla A_\varphi \nabla A_t + \omega(\nabla A_\varphi)^2\right] = 0, \tag{2.24}$$

$$e^{-4\nu}\rho^2\left[\nabla A_t\nabla\omega + \omega(\nabla A_\varphi\nabla\omega)\right] - 2\nabla A_\varphi\nabla\nu - \Delta A_\varphi + \frac{2A_{\varphi,\rho}}{\rho} = 0, \tag{2.25}$$

$$-2\nabla A_t\nabla\nu - 2\omega\nabla A_\varphi\nabla\nu + \nabla A_\varphi\nabla\omega + \Delta A_t + \omega\Delta A_\varphi = 0. \tag{2.26}$$

Furthermore we have two equations from

Einstein $[\hat{1},\hat{1}]$:

$$\begin{aligned}\alpha_{,\rho} = {} & \rho\left[(\nu_{,\rho})^2 - (\nu_{,\zeta})^2\right] - \frac{1}{4}e^{-4\nu}\rho^3\left[(\omega_{,\rho})^2 - (\omega_{,\zeta})^2\right] - \nu_{,\rho} \\ & + \frac{e^{2\nu}}{\rho}\left[(A_{\varphi,\rho})^2 - (A_{\varphi,\zeta})^2\right] - e^{-2\nu}\rho\left[(\omega A_{\varphi,\rho} + A_{t,\rho})^2 - (\omega A_{\varphi,\zeta} + A_{t,\zeta})^2\right],\end{aligned} \tag{2.27}$$

and Einstein $[\hat{1},\hat{2}]$:

$$\alpha_{,\zeta} = 2\rho\nu_{,\rho}\nu_{,\zeta} - \frac{1}{2}e^{-4\nu}\rho^3\omega_{,\rho}\omega_{,\zeta} - \nu_{,\zeta} + \frac{2e^{2\nu}}{\rho}(A_{\varphi,\rho} + A_{\varphi,\zeta}) - 2e^{-2\nu}\rho(\omega A_{\varphi,\rho} + A_{t,\rho})(\omega A_{\varphi,\zeta} + A_{t,\zeta}). \tag{2.28}$$

Additionally from the trace equation $R^{\hat{i}}{}_{\hat{i}} + 8\pi T^{\hat{i}}{}_{\hat{i}} = 0$, we get

$$\begin{aligned}8\pi\mu - \frac{1}{2\rho}e^{-2\alpha-4\nu}\{ & \rho^3\left[{\omega_{,\rho}}^2 + {\omega_{,\zeta}}^2\right] \\ & - 4e^{4\nu}\left[-\nu_{,\rho} + \rho\left({\nu_{,\rho}}^2 + {\nu_{,\zeta}}^2 + \alpha_{,\rho\rho} + \alpha_{,\zeta\zeta}\right)\right]\} = 0.\end{aligned} \tag{2.29}$$

These are the non-trivial Einstein-Maxwell field equations for the stationary and axialsymmetric perfect dust in an electrovacuum. In order to introduce the disc characteristics into our system, we have to take a further look at the boundary conditions.

2.4 Boundary conditions

2.4.1 Symmetry properties of the fields

Setting $(\rho,\zeta) = (0,0)$ as our disc centre, with the ζ-axis as the rotating axis and the disc lying on the plane $\zeta = 0$, and with $\rho = \rho_0$ being the radius of the disc, we divide the spacetime of the stationary rotating disc of charged dust, as shown in figure 2.1 into five parts: The ζ-axis, the surface of the disc, the equatorial plane outside of the disc, infinity and the rest of spacetime.

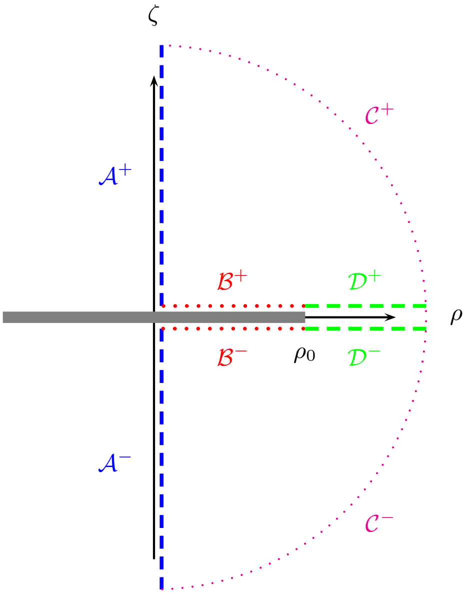

Figure 2.1: The rotating disc of charged dust shown in the Weyl coordinates. The thick black line denotes the infinite thin disc with radius ρ_0. The areas illustrated in the figure imply each particular part of the boundary conditions: $\mathcal{A}$: ζ-axis, $\mathcal{B}$: On the disc surface, $\mathcal{C}$: Infinity, $\mathcal{D}$: The equatorial plane outside of the disc.

Reflectional symmetry

Due to the reflectional symmetry of the metric coefficient of (2.6) on the equatorial plane $\rho = 0$, all four fields in the upper and lower areas with respect to the equatorial plane have the symmetric characteristic

$$\nu_+ = \nu_-, \qquad \omega_+ = \omega_-, \qquad \alpha_+ = \alpha_-, \qquad A_{\varphi_+} = A_{\varphi_-}, \qquad A_{t+} = A_{t-}, \tag{2.30}$$

with the subscripts "+" implying the fields at (ρ, ζ) and "−" at $(\rho, -\zeta)$. For our infinitly thin disc of dust, the regularity condition is therefore supported through the equatorial symmetry

$$\lim_{\delta\to 0} \{\nu, \omega, \alpha\} |_{\zeta=+\delta} = \lim_{\delta\to 0} \{\nu, \omega, \alpha\} |_{\zeta=-\delta} = \{\nu(\rho, 0), \omega(\rho, 0), \alpha(\rho, 0)\}$$

Without loss of generality, due to the equatorial symmetry (2.30), the discussion can be focused on one single side of the equatorial plane, which will omit the + and − sign from now on and focus on the upper part of the coordinate $\zeta \geq 0$.

2.4.2 Derivation of the Boundary Conditions

- $\mathcal{A}$: $\rho = 0$
  Area $\mathcal{A}$ represents the ζ axis where $\rho = 0$. Substituting $\rho = 0$ into the field equations (2.23)-(2.26), however, is not sufficient to obtain the boundary conditions, since some non-trivial terms that are embedded with ρ would disappear after introducing $\rho = 0$. The way to solve the problem is to take the ρ derivatives of the

field equaitons in order to elimintate the embedding ρ on the non trivial terms, before substituting $\rho = 0$.

The actual calculation will be demonstrated in section 3.2.1 with another coordinate[4].

- $\mathcal{B}$: $0 \leq \rho \leq \rho_0$, $\zeta \to 0$
  The disc is axialsymmetric along $\zeta = 0$, since the configuration is an infinitly thin layer, whose mass density can be defined as

$$\mu := e^{-\alpha(\rho,\zeta)}\sigma_p(\rho)\delta(\zeta), \tag{2.31}$$

where $\sigma_p(\rho)$ is the surface density along the ρ-axis and $\delta(\zeta)$ is the delta function along the ζ-axis.

The charge and energy-momentum element distribution are analogous to the Gauss surface charge in the electrodynamics. We can therefore apply the Gauss-integration, also known as the “pill-box” integration on (2.19)-(2.22) and (2.29).

The following is the result of the pill-box integration, whose detailed calculation is in Appendix B:

$$\text{from Einstein } [\hat{4},\hat{4}]: \quad \frac{2e^{\alpha}\pi\sigma_p[1 + e^{-4\nu}\rho^2(\Omega - \omega)^2]}{1 - e^{-4\nu}\rho^2(\Omega - \omega)^2} = \nu_{,\zeta}, \tag{2.32}$$

$$\text{from Einstein } [\hat{3},\hat{4}]: \quad -\frac{8e^{\alpha+2\nu}\pi\sigma_p(\Omega - \omega)}{\rho[1 - e^{-4\nu}\rho^2(\Omega - \omega)^2]} = \omega_{,\zeta}, \tag{2.33}$$

$$\text{from Maxwell } [\hat{3}]: \quad -\frac{2e^{\alpha-3\nu}\pi\varepsilon\rho^2\sigma_p(\Omega - \omega)}{\sqrt{1 - e^{-4\nu}\rho^2(\Omega - \omega)^2}} = A_{\varphi,\zeta}, \tag{2.34}$$

$$\text{from Maxwell } [\hat{4}]: \quad \frac{2e^{\alpha+\nu}\pi\varepsilon\sigma_p}{\sqrt{1 - e^{-4\nu}\rho^2(\Omega - \omega)^2}} = A_{t,\zeta} + \omega A_{\varphi,\zeta}, \tag{2.35}$$

$$\text{and from Trace equation:} \quad -2\pi e^{\alpha}\sigma_p = \alpha_{,\zeta}. \tag{2.36}$$

Combining any two of (2.32)-(2.35) to eliminate α, the first three boundary conditions

$$-4(\Omega - \omega)\nu_{,\zeta} - [1 + e^{-4\nu}\rho^2(\Omega - \omega)^2]\omega_{,\zeta} = 0, \tag{2.37}$$

$$\rho^2(\Omega - \omega)A_{t,\zeta} + [e^{4\nu} + \rho^2(\Omega - \omega)\omega]A_{\varphi,\zeta} = 0, \tag{2.38}$$

$$-4e^{3\nu}A_{\varphi,\zeta} + \varepsilon\rho^2\sqrt{1 - e^{-4\nu}\rho^2(\Omega - \omega)^2}\,\omega_{,\zeta} = 0, \tag{2.39}$$

---

[4] The spectral coordinates, which we will discuss in section 3.1.2

are obtained, and combing (2.32)-(2.36) with (2.28), the forth boundary condition is acquired

$$
\begin{aligned}
-\rho(\Omega-\omega)^2 - e^{3\nu}\varepsilon\sqrt{1-e^{-4\nu}\rho^2(\Omega-\omega)^2}\left(A_{t,\rho}-\Omega A_{\varphi,\rho}\right)& \\
+ e^{4\nu}\nu_{,\rho} + \rho^2(\Omega-\omega)\left[(\Omega-\omega)\nu_{,\rho}+\omega_{,\rho}\right] &= 0. \qquad (2.40)
\end{aligned}
$$

In the case where Ω and ε are constant, integrating (2.40) along the disc with $0 \leq \rho \leq \rho_0$ and $\zeta = 0$

$$
D := e^{\nu}\sqrt{1-\frac{\rho^2\left(\Omega-\omega\right)^2}{e^{4\nu}}} - \varepsilon\left(A_t+\Omega A_{\varphi}\right) = constant. \qquad (2.41)
$$

is obtained[5]. At the centre of the disc $\rho = 0$ where $A_{\varphi} = 0$,

$$
D = e^{\nu^c} - \varepsilon A_t^c = constant, \qquad (2.42)
$$

where $\nu^c = \nu(\rho = 0, \zeta = 0)$ and $A_t^c = A_t(\rho = 0, \zeta = 0)$.

(2.41) can also serve as an alternative boundary condition to (2.40), which simplifies both the analytical and numerical calculations, however this will then be restricted to the case of constant angular velocities. Therefore keeping (2.40) as the boundary condition permits the discussion of the case of the differential rotating disc $\Omega(\rho)$.

- $\mathcal{C}$: $\rho^2 + \zeta^2 \to \infty$
  At spacial infinity, i.e. $r^2 = \rho^2 + \zeta^2 \to \infty$, asymptotic flatness is assumed. The Lewis-Papapetrou metric thus reduces to Minkowski metric in cylindrical coordinate $ds^2 = d\rho^2 + d\zeta^2 + \rho^2 d\varphi^2 - dt^2$, which means

$$
\nu \to 0, \qquad \omega \to 0, \qquad \alpha \to 0. \qquad (2.43)
$$

The electromagnetic fields vanish in infinity

$$
A_{\varphi} \to 0, \qquad A_t \to 0. \qquad (2.44)
$$

---

[5] It is easier to perform the integration of the boundary condition obtained under the co-rotating frame using the metric (2.7)[23]

$$
\left(e^{U'} - \varepsilon A_{t'}\right)_{,\rho} = 0,
$$

which gives

$$
e^{U'} - \varepsilon A_{t'} = constant.
$$

With “ ′ ” denoting the co-rotating frame

$$
e^{2U'} = e^{2U}\left[(1+a\Omega)^2 - \Omega^2\rho^2 e^{-4U}\right], \qquad A_{\varphi'} = A_t + \Omega A_{\varphi},
$$

and the relation between the potentials ν, ω and the potentials U, a in (2.8) and (2.9), we get (2.41).

- $\mathcal{D}$: $\rho > \rho_0$, $\zeta = 0$
  Since the fields are even functions with respect to the equatorial plane (2.30), their normal derivative are antisymmetric

  $$\lim_{\delta\to 0}\{\nu_{,\zeta}, \omega_{,\zeta}, A_{\varphi_{,\zeta}}, A_{t,\zeta}\}|_{\zeta=+\delta} = -\lim_{\delta\to 0}\{\nu_{,\zeta}, \omega_{,\zeta}, A_{\varphi_{,\zeta}}, A_{t,\zeta}\}|_{\zeta=-\delta}$$

  Due to the regularity condition, here meaning that the fields have to be continuous at $\zeta = 0$, the fields are thus

  $$\nu_{,\zeta} = 0, \qquad \omega_{,\zeta} = 0, \qquad A_{\varphi_{,\zeta}} = 0, \qquad A_{t,\zeta} = 0. \tag{2.45}$$

- $\mathcal{A} \cap \mathcal{B}$: Centre of the disc $\rho = 0$, $\zeta = 0$
  At the centre of the disc,

  $$e^{\nu} \equiv e^{\nu^c} \tag{2.46}$$

  is related to the relative redshift z of zero angular momentum photons emitted from the centre of the disc received by a static observer in infinity [24], according to $e^{\nu^c} = \frac{1}{1+z}$. At the Newtonian limit $z \to 0$, we have $e^{\nu^c} = 1$, whereas at the ultra-relativistic limit $z \to \infty$, $e^{\nu^c} = 0$.

The potential α, as shown in (2.27) and (2.28), is expressed explicitly in the differential terms and is decoupled from the other potentials, meaning that it can be obtained independently after the coupled equation system, containing electrovacuum field equations and the boundary conditions, is solved for the potentials ν, ω, A_φ and A_t.

2.5 Parameter Space (γ, ε)

The potential e^{ν^c} mentioned in the previous section describes the relative redshift of the photons, which can thus be regarded as an index describing the degree of relativity. We introduce a relativity parameter γ here

$$\gamma := 1 - e^{\nu^c}, \tag{2.47}$$

with $\gamma \in [0, 1]$. $\gamma \to 0$ implying the Newtonian limit and $\gamma \to 1$ indicating the ultra-relativistic limit, to which our rotating charged disc becomes an extreme Kerr-Newman black hole from the external point of view.

For the constant specific charge $\varepsilon \in [-1, 1]$, $\varepsilon = 0$ describes the uncharged configurations, whereas $|\varepsilon| = 1$ describes the electrically counterpoised dust (ECD) configurations[25], where the gravitational and the electrical forces are counter-balanced, i.e. $\rho_{el} = \mu$ in (2.5), and the angular velocity Ω thus becomes 0. The plus-minus sign implies a positive or negative charge, since they do not effect behaviour in terms of the magnitude of the charge of interest. Without loss of generality, the discussion is set at $\varepsilon \in [0, 1]$.

The two parameters γ and ε form a complete parameter space and are discussed in [23, 14, 15]. Figures 1 and 2 in [14] depict the parameter space describing the relationship between these two parameters and the corresponding systems.

Since (γ, ε) form a complete parameter space, all the other parameters can be regarded as (γ, ε)-dependent and cannot be randomly defined. This is particularly important when setting up the numerical procedure, as can be seen later on in the next chapter.

Chapter 3

Numerical Treatment

In this chapter, the numerical method used in this work is presented, along with how it is applied to the system. The procedure of the Pseudo-spectral method is first introduced, followed by the method to this equation system, by presenting a compactificated coordinate and rescaling the potentials of the equations. The new equation system can then be formed in to vector fields which, after introducing suitable initial data, can be iterated through the Newton-Raphson method. Finally, some numerical issues that might be encountered during the process are discussed along with how to solve them.

3.1 Pseudo-Spectral Method

3.1.1 Overview

For the numerical solution, the spectral approximation [26] is applied by setting the field functions into a linear combination of Chebyshev polynomials

$$T_m(x) = \cos[m \arccos x]. \tag{3.1}$$

In a 1-D case, the expansion can be written as

$$f(x_j) = \frac{1}{2}c_0 + \sum_{m=1}^{N} c_m T_m(2x_j - 1), \tag{3.2}$$

where the spectral coordinates x_j runs from 0 to 1.

$$x_j = \frac{1}{2}\left[1 + \cos\left(\frac{\pi j}{N}\right)\right] \quad (j = 0, \cdots, N),$$

and spectral coefficient

$$c_m = \frac{2 - \delta_{mN}}{N}\left[f(1) + (-1)^m f(0) + 2\sum_{j=1}^{N-1} f(x_j) T_m(2x_j - 1)\right]. \tag{3.3}$$

with m the order of expansion, j the order of the grid point, and $N+1$ the total number of the grid points, since j starts with 0.

The Pseudo-spectral method works as follows: an initial guess $\vec{f}^{(0)}$ for the system is given[1], and the initial guess expressed in terms of Chebyshev polynomials through (3.3), where the spectral coefficient $\vec{c}^{(0)}$ is obtained. The derivatives of the spectral coefficients $\vec{c}^{(0)\prime}$, $\vec{c}^{(0)\prime\prime}$ are obtained via an differential operator $\hat{D}$ [26], and the derivatives of the Chebyshev polynomial fields $\vec{f}^{(0)\prime}$, $\vec{f}^{(0)\prime\prime}$ via $\vec{c}^{(0)\prime}$, $\vec{c}^{(0)\prime\prime}$ respectively using (3.2). An overview of the procedure is shown in Table 3.1.

After obtaining $\vec{f}^{(0)}$, $\vec{f}^{(0)\prime}$, and $\vec{f}^{(0)\prime\prime}$, the fields are substituted into the field equations $\vec{F}(\vec{f}, \vec{f}', \vec{f}'')$:

(i) If $\vec{F}(\vec{f}^{(0)}, \vec{f}^{(0)\prime}, \vec{f}^{(0)\prime\prime}) < \delta \to 0$: $f^{(0)}$ is thus the field in question.

(ii) If $\vec{F}(\vec{f}^{(0)}, \vec{f}^{(0)\prime}, \vec{f}^{(0)\prime\prime}) > \delta \to 0$: the procedure is first iterated to get $\vec{f}^{(1)}$ via

$$\vec{f}^{(1)} = \vec{f}^{(0)} - \hat{J}(\vec{f}^{(0)})\vec{F}(\vec{f}^{(0)}),$$

with $\hat{J}$ being the Jacobi-matrix.

From $\vec{f}^{(1)}$, we get $\vec{c}^{(1)}$, $\vec{c}^{(1)\prime}$, $\vec{c}^{(1)\prime\prime}$ then $\vec{f}^{(1)}$, $\vec{f}^{(1)\prime}$, $\vec{f}^{(1)\prime\prime}$, which can again be iterated by substitution into $\vec{F}(\vec{f}, \vec{f}', \vec{f}'')$. More detail of the iteration is discussed in section 3.1.3.

Table 3.1 show the comparison between the spectral method and the pseudo-spectral method. Both start with the initial guess $\vec{f}$ and obtain $\vec{c}$ from (3.2). The difference becomes apparent afterwards, where the spectral method first obtains $\vec{f}'$, $\vec{f}''$ then $\vec{c}'$, $\vec{c}'$, and the pseudo-spectral method first acquires $\vec{c}'$, $\vec{c}'$ then $\vec{f}'$, $\vec{f}''$. The pseudo-spectral method is used as shown in Table 3.1, since this method obtain the derivatives of $\vec{c}$ with just one step, whereas the spectral method requires two steps[2].

3.1.2 Compactification

The spectral coordinates is adapted to the system, by performing the following coordinate transformation [27]

$$\rho = \frac{\rho_0\sqrt{1-\tau}}{\cos\left(\frac{\pi}{2}\sigma\right)}, \qquad \zeta = \rho_0\sqrt{\tau}\tan\left(\frac{\pi}{2}\sigma\right), \tag{3.4}$$

which converts $(\rho, \zeta) \in [0, \infty]$ to $(\sigma, \tau) \in [0, 1]$. Figure (2.1) shows the system in Weyl coordinatess, whereas Figure (3.2) displays the comparison between the spectral coordinates and the Weyl coordinatess.

---

[1] Note that the superscript "(n)" does not imply the polynomial order of f, instead it signifies the number of iterations, differentiating from the subscript "j", which signifies the position of the grid and from the subscript "m", the order of expansion.

[2] Or rather, the spectral method has to use two operators $\hat{T}$ and $\hat{D}$ instead of one $\hat{D}$, as in the pseudo-spectral method.

Spectral method	Pseudo-spectral method
$$\begin{tikzcd} \vec{f} \arrow[r, "\vec{c}=\hat{T}^{-1}\vec{f}"] & \vec{c} \arrow[d, "\begin{array}{l}(\hat{T}'=\hat{D}\hat{T})\\ \hat{f}'=\hat{T}'\vec{c}=\hat{D}\hat{T}\vec{c}\end{array}"'] & \\ & \vec{f'} \arrow[r, "\vec{c'}=\hat{T}^{-1}\vec{f'}"] \arrow[d, "\begin{array}{l}\hat{f}''=\hat{T}'\vec{c'}=\hat{D}\hat{T}\vec{c'}\\ \text{or}\\ (\hat{T}''=\hat{D}\hat{D}\hat{T})\\ \hat{f}''=\hat{T}''\vec{c}=\hat{D}\hat{D}\hat{T}\vec{c}\end{array}"'] & \vec{c'} \\ & \vec{f''} \arrow[r, "\vec{c''}=\hat{T}^{-1}\vec{f''}"] & \vec{c''} \\ & \vdots & \end{tikzcd}$$	$$\begin{tikzcd} \vec{f} \arrow[r, "\vec{c}=\hat{T}^{-1}\vec{f}"] & \vec{c} \arrow[d, "\vec{c'}=\hat{D}\vec{c}"'] & \\ & \vec{c'} \arrow[r, "\vec{f'}=\hat{T}\vec{c'}"] \arrow[d, "\vec{c''}=\hat{D}\vec{c'}"'] & \vec{f'} \\ & \vec{c''} \arrow[r, "\vec{f''}=\hat{T}\vec{c''}"] & \vec{f''} \\ & \vdots & \end{tikzcd}$$

Table 3.1: Comparison between the procedures of the spectral method and the pseudo-spectral method. $\vec{f}$ represents the field function; $\vec{c}$ is the expansion coefficient; $\hat{T}$ is the base of the expansion as in (3.1) in the above; $\hat{D}$ is the differential operator. Both methods begin by giving an initial guess $\vec{f}$ and obtain $\vec{c}$ via (3.3). The difference starts once $\vec{c}$ is obtained: the spectral method first acquires $\vec{f'}$ from the differential and base operator $\hat{D}$ and $\hat{T}$, then from $\vec{f'}$ one uses the inverse base operator $\hat{T}^{-1}$ as in (3.3) to obtain $\vec{c'}$; whereas for the pseudo-spectral method, one deduces $\vec{c'}$ directly from $\vec{c}$, then from $\vec{c'}$ to $\vec{f'}$. The respective procedures carry on for higher derivatives.

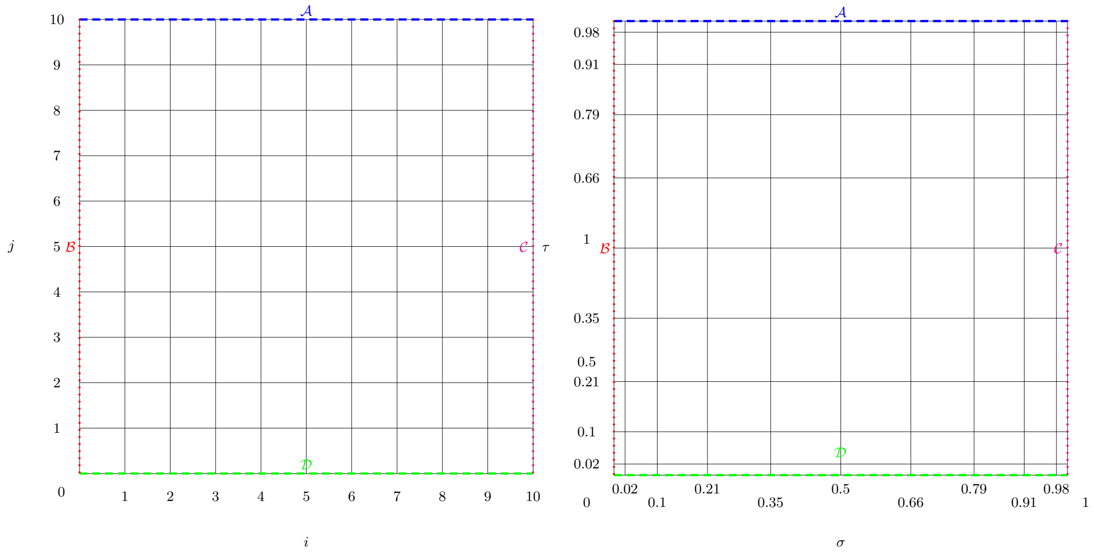

(a) (b)

Figure 3.1: Diagramatic sketch of the two grid, here with $N = 10$. (a) Numerical grid (b) Spectral grid.

In the 2-D case presented here, the Chebyshev expansion of the fields of every single grid points (σ_i, τ_j) can then be expressed as

$$
\begin{aligned}
f(\sigma_i,\tau_j) &= \left(\frac{1}{2}c_0(\tau) + \sum_{k=1}^{N_\sigma} c_k(\tau) T_k(2\sigma_i - 1)\right) \cdot \left(\frac{1}{2}c_0(\sigma) + \sum_{m=1}^{N_\tau} c_m(\sigma) T_m(2\tau_j - 1)\right) \\
&= \frac{1}{4}c_0(\sigma)c_0(\tau) + \frac{1}{2}c_0(\sigma)\sum_{k=1}^{N_\sigma} c_k(\tau)T_k(2\sigma_i - 1) + \frac{1}{2}c_0(\tau)\sum_{m=1}^{N_\tau} c_m(\sigma)T_m(2\tau_j - 1) \\
&\quad + \sum_{k=1}^{N_\sigma}\sum_{m=1}^{N_\tau} c_m(\sigma)c_k(\tau)T_k(2\sigma_i - 1)T_m(2\tau_j - 1), \qquad (3.5)
\end{aligned}
$$

with

$$
\begin{aligned}
\sigma_i &= \frac{1}{2}\left[1 + \cos\left(\frac{\pi i}{N_\sigma}\right)\right] \quad (i = 0, \cdots, N_\sigma), \\
& \qquad\qquad\qquad\qquad\qquad\qquad (3.6) \\
\tau_j &= \frac{1}{2}\left[1 + \cos\left(\frac{\pi j}{N_\tau}\right)\right] \quad (j = 0, \cdots, N_\tau).
\end{aligned}
$$

The numerical grid and the spectral grid thus look as in figure 3.1. In the plot, the sketch of the two grids with $N = 10$ are shown. In our actual grid, $N = 50$ is applied.

3.1.3 Newton-Raphson Method

The expansion (3.5) is substituted into the field equations and boundary conditions, building up a differential equation system with all unknown fields on every collocation

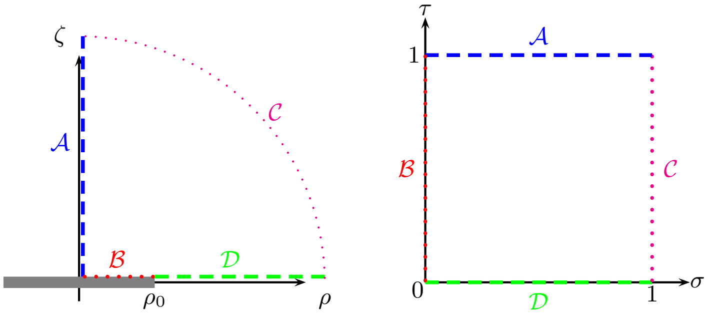

Figure 3.2: The rotating disc of charged dust is shown on the left: Weyl coordinatess and right: spectral coordinates. The boundary conditions imply respectively: $\mathcal{A}$ ($\rho = 0$; $\tau = 1$): ζ-axis of the Weyl coordinates, $\mathcal{B}$ ($\zeta = 0, 0 < \rho \leq \rho_0$; $\sigma = 0$): On the disc surface, $\mathcal{C}$ ($\rho^2 + \zeta^2 \to \infty$; $\sigma = 1$): Infinity, $\mathcal{D}$ ($\zeta = 0, \rho > \rho_0$; $\tau = 0$): Equatorial plane outside of the disc.

points (i, j) in the $(N_\sigma + 1) \times (N_\tau + 1)$ grid[3]. The total number of equations or fields is

$$N_{total} = N_{fields}(N_\sigma + 1)(N_\tau + 1) + N_{aux}, \tag{3.7}$$

where N_{fields} is the number of the field, and N_{aux} is the number of the auxiliary parameter of the system.

Using the Newton-Raphson method to solve the equation system by forming the unknown fields into a column of vector field $\vec{f}(\sigma_i, \tau_j)$, the goal is to find $\vec{f}$, such that when substituted into the differential equation system $\vec{F}$, it satisfies

$$\vec{F}(\vec{f}) = 0.$$

The iteration

$$\vec{f}_{m+1} = \vec{f}_m - \left[\hat{J}(\vec{f}_m)\right]^{-1} \vec{F}(\vec{f}_m) \tag{3.8}$$

is started by giving an initial guess $\vec{f}_0$, and iterating until $\vec{F}(\vec{f}_{m+1}) < \delta$, where $\delta \to 0$, as discussed in section 3.1.1.

The Jacobi matrix is obtained through

$$\hat{J} = \frac{\vec{F}}{\vec{f}}, \qquad J_{ij} = \frac{F_i}{f_j}. \qquad (i, j = 0, \cdots, N_{total} - 1),$$

where its inverse matrix $\left[\hat{J}(\vec{f}_m)\right]^{-1}$ can be obtained by $LU - decomposition$ for small resolutions and by further numerical methods, such as $BiCGSTAB$[28], for large resolutions.

---

[3] C-language starts its serial from 0.

3.2 Rescaling the potential

3.2.1 Equation System

Since ν always comes in an exponential form, and moreover at the ultra-relativistic limit, the e^{ν^c} in the auxiliary equation (2.46) tends to 0, which makes $\nu \to -\infty$, new potentials are therefore rescaled [27]

$$\tilde{\nu} := e^{\nu}, \tag{3.9}$$

and

$$\tilde{\omega} := \frac{\rho_0}{e^{\nu^c}}\omega.$$

Furthermore ω and α are also rescaled in a similar way

$$\tilde{A}_t := \frac{\rho_0}{e^{\nu^c}}A_t, \qquad \tilde{\alpha} := e^{\alpha},$$

the metric (2.6) expressed in the new potential thus becomes

$$ds^2 = \tilde{\alpha}(d\rho^2 + d\zeta^2) + \frac{\rho^2}{\tilde{\nu}^2}(d\varphi - \frac{e^{\nu^c}}{\rho_0}\tilde{\omega}dt)^2 - \tilde{\nu}dt^2. \tag{3.10}$$

Apart from the potential transformation, the coordinates are transformed from Weyl coordinatess to the spectral coordinates (3.4)

$$\rho = \frac{\rho_0\sqrt{1-\tau}}{\cos\left(\frac{\pi}{2}\sigma\right)}, \qquad \zeta = \rho_0\sqrt{\tau}\tan\left(\frac{\pi}{2}\sigma\right)$$

With the detailed calculation shown in the appendix C, the field equations thus become

- Einstein $[\hat{4},\hat{4}]$ $F_{\tilde{\nu}} = -\frac{1}{2}{\rho_0}^2(1-\tau)\tilde{\nu}F_{\tilde{\nu}}^{(dust)} + F_{\tilde{\nu}}^{(em)} = 0$, with

$$\begin{aligned} F_{\tilde{\nu}}^{(dust)} &= (1-3\tau)\tilde{\nu}_{,\tau} + 2\Delta'\tilde{\nu} - \frac{2}{\tilde{\nu}}\left(\nabla'\tilde{\nu}\right)^2 - \frac{(1-\tau)e^{2\nu^c}}{\cos^2\left(\frac{\pi}{2}\sigma\right)\tilde{\nu}^3}\left(\nabla'\tilde{\omega}\right)^2, \\ F_{\tilde{\nu}}^{(em)} &= \left[\cos^2\left(\frac{\pi}{2}\sigma\right)\tilde{\nu}^4 + e^{2\nu^c}(1-\tau)\tilde{\omega}^2\right]\left(\nabla'A_{\varphi}\right)^2 + e^{2\nu^c}(1-\tau)\left[2\tilde{\omega}\nabla'A_{\varphi}\nabla'\tilde{A}_t + \left(\nabla'\tilde{A}_t\right)^2\right] \end{aligned} \tag{3.11}$$

- Einstein $[\hat{3},\hat{4}]$ $F_{\tilde{\omega}} = -\frac{e^{\nu^c}{\rho_0}^2(1-\tau)}{8\cos^2\left(\frac{\pi}{2}\sigma\right)\tilde{\nu}^2}F_{\tilde{\omega}}^{(dust)} + F_{\tilde{\omega}}^{(em)} = 0$, with

$$\begin{aligned} F_{\tilde{\omega}}^{(dust)} &= \frac{1}{\pi}\sin(\pi\sigma)\tilde{\omega}_{,\sigma} + (1-5\tau)\tilde{\omega}_{,\tau} - \frac{8}{\tilde{\nu}}\nabla'\tilde{\nu}\nabla'\tilde{\omega} + 2\Delta'\tilde{\omega}, \\ F_{\tilde{\omega}}^{(em)} &= e^{\nu^c}\left[\nabla'A_{\varphi}\nabla'\tilde{A}_t + \tilde{\omega}\left(\nabla'A_{\varphi}\right)^2\right], \end{aligned} \tag{3.12}$$

- Maxwell $[\hat{3}]$

$$\begin{aligned}F_{A_\varphi} =&\frac{1}{2\pi}\cos^2\left(\frac{\pi}{2}\sigma\right)\tilde{\nu}^4\big[\sin(\pi\sigma)A_{\varphi,\sigma}-\pi(1-\tau)A_{\varphi,\tau}\big]\\ &-2\cos^2\left(\frac{\pi}{2}\sigma\right)\tilde{\nu}^3\nabla'\tilde{\nu}\nabla' A_\varphi + e^{2\nu^c}(1-\tau)\tilde{\omega}\nabla'\tilde{\omega}\nabla' A_\varphi\\ &+e^{2\nu^c}\left[(1-\tau)\nabla'\tilde{\omega}\nabla'\tilde{A}_t\right]-\cos^2\left(\frac{\pi}{2}\sigma\right)\tilde{\nu}^4\Delta' A_\varphi = 0.\end{aligned} \tag{3.13}$$

- Maxwell $[\hat{4}]$

$$\begin{aligned}F_{\tilde{A}_t} =& \frac{1}{2}(1-3\tau)\tilde{\nu}e^{\nu^c}\left(\tilde{\omega}A_{\varphi,\tau}+\tilde{A}_{t,\tau}\right)\\ &-2e^{\nu^c}\tilde{\omega}\nabla'\tilde{\nu}\nabla' A_\varphi + e^{\nu^c}\tilde{\nu}\nabla'\tilde{\omega}\nabla' A_\varphi - 2e^{\nu^c}\nabla'\tilde{\nu}\nabla'\tilde{A}_t + e^{\nu^c}\tilde{\nu}\tilde{\omega}\Delta' A_\varphi + e^{\nu^c}\tilde{\nu}\Delta'\tilde{A}_t = 0.\end{aligned} \tag{3.14}$$

where

$$\begin{aligned}\nabla' a\nabla' b &:= \frac{1}{\pi^2}\cos^2\left(\frac{\pi}{2}\sigma\right)a_{,\sigma}b_{,\sigma}+\tau(1-\tau)a_{,\tau}b_{,\tau},\\ \Delta' a &:= \frac{1}{\pi^2}\cos^2\left(\frac{\pi}{2}\sigma\right)a_{,\sigma\sigma}+\tau(1-\tau)a_{,\tau\tau},\end{aligned}$$

all of which can also be explicitly separated into the charged part and the non-charged part.

For the respective boundary conditions,

- $\mathcal{A}$: $\tau = 1$

  Substituting $\tau = 1$ into the field equations (3.11)-(3.14). However, it is observed that the left-hand-side of (3.11) and (3.12) become 0, and in order to avoid this triviaity, the τ-derivative of these two equations is used instead, which gives

$$\begin{aligned}F^{\mathcal{A}}_{\tilde{\nu}} = \{F_{\tilde{\nu},\tau}\}\,|_{\tau=1} = \frac{1}{2}{\rho_0}^2\tilde{\nu}F^{dust}_{\tilde{\nu}} + F^{em}_{\tilde{\nu},\tau} = 0, \quad \text{with}&\\ F^{dust}_{\tilde{\nu}} = -2\tilde{\nu}_{,\tau}+2\Delta'\tilde{\nu}-\frac{2}{\tilde{\nu}}\left(\nabla'\tilde{\nu}\right)^2,&\\ F^{em}_{\tilde{\nu},\tau} = \cos^2\left(\frac{\pi}{2}\sigma\right)\left[\tilde{\nu}^4(\nabla' A_\varphi)^2\right]_{,\tau}&\\ -e^{2\nu^c}\tilde{\omega}\left[\tilde{\omega}\left(\nabla' A_\varphi\right)^2+2\left(\nabla' A_\varphi\nabla'\tilde{A}_t\right)\right]-\frac{e^{2\nu^c}}{\rho_0}\left(\nabla'\tilde{A}_t\right)^2.&\\ F^{\mathcal{A}}_{\tilde{\omega}} = \{F_{\tilde{\omega},\tau}\}\,|_{\tau=1} = \frac{e^{\nu^c}\rho_0^2}{8\cos^2\left(\frac{\pi}{2}\sigma\right)\tilde{\nu}^2}F^{dust}_{\tilde{\nu}} + F^{em}_{\tilde{\nu},\tau} = 0, \quad \text{with}&\\ F^{dust}_{\tilde{\omega}} = \frac{1}{\pi}\sin(\pi\sigma)\tilde{\omega}_{,\sigma}-4\tilde{\omega}_{,\tau}-\frac{8}{\tilde{\nu}}\nabla'\tilde{\nu}\nabla'\tilde{\omega}+2\Delta'\tilde{\omega},&\\ F^{em}_{\tilde{\omega},\tau} = e^{\nu^c}\left(\nabla' A_\varphi\nabla'\tilde{A}_t\right)_{,\tau}+e^{\nu^c}\left[\tilde{\omega}\left(\nabla' A_\varphi\right)^2\right]_{,\tau},&\end{aligned}$$

  where

$$\left\{\left(\nabla' a\nabla' b\right)_{,\tau}\right\}|_{\tau=1} := \frac{1}{\pi^2}\cos^2\left(\frac{\pi}{2}\sigma\right)\left(a_{,\sigma}b_{,\sigma}\right)_{,\tau}+a_{,\tau}b_{,\tau}$$

- $\mathcal{B}$: $\sigma = 0$
  The $\sigma = 0$ substitution of (2.37)-(2.40) in (σ, τ)-coordinates yields

$$F^{\mathcal{B}}_{\tilde{\nu}} = 4W\tilde{\nu}^3\tilde{\nu}_{,\sigma} + e^{\nu^c}(\tilde{\nu}^4 + (1-\tau)W^2)\tilde{\omega}_{,\sigma} = 0,$$

$$F^{\mathcal{B}}_{\tilde{\omega}} = e^{\nu^c}(1-\tau)W\tilde{A}_{t,\sigma} + (\tilde{\nu}^4 + e^{\nu^c}(1-\tau)W\tilde{\omega})A_{\varphi,\sigma} = 0,$$

$$F^{\mathcal{B}}_{A_\varphi} = -4\tilde{\nu}^5 A_{\varphi,\sigma} + e^{\nu^c}\varepsilon(1-\tau)\rho_0\sqrt{\tilde{\nu}^4 - (1-\tau)W^2}\,\tilde{\omega}_{,\sigma} = 0,$$

$$\begin{aligned} F^{\mathcal{B}}_{\tilde{A}_t} = {} & 2\varepsilon\tilde{\nu}^2\sqrt{\tilde{\nu}^4 - (1-\tau)W^2}\left(e^{\nu^c}\tilde{A}_{t,\tau} + \rho_0\Omega A_{\varphi,\tau}\right) - 2\rho_0\tilde{\nu}_{,\tau}\left[\tilde{\nu}^4 + (1-\tau)W^2\right] \\ & - \rho_0 W\tilde{\nu}\left[W + 2e^{\nu^c}(1-\tau)\tilde{\omega}_{,\tau}\right] = 0, \end{aligned}$$

  where

$$W := \rho_0\Omega - e^{\nu^c}\tilde{\omega}.$$

- $\mathcal{C}$: $\sigma = 1$

$$F^{\mathcal{C}}_{\tilde{\nu}} = \tilde{\nu} = 1, \quad F^{\mathcal{C}}_{\tilde{\omega}} = \tilde{\omega} = 0, \quad F^{\mathcal{C}}_{A_\varphi} = A_\varphi = 0, \quad F^{\mathcal{C}}_{\tilde{A}_t} = \tilde{A}_t = 0.$$

- $\mathcal{D}$: $\tau = 0$
  For Area $\mathcal{D}$, substituting $\tau = 0$ into (3.11)-(2.22) does not lead to triviality, the outcome of which can be used in this equation system.

- $\mathcal{B} \cap \mathcal{D}$: $(\sigma, \tau) = (0, 0)$
  On the rim of the disc $\rho = \rho_0$, (2.45) can be used as the transition equation between the disc and the electro-valcuum on ρ-axis in figure 2.1. Written in the (σ, τ)-coordinates, it gives

$$F^{\mathcal{BD}}_{\tilde{\nu}} = \tilde{\nu}_{,\sigma} = 0, \qquad F^{\mathcal{BD}}_{\tilde{\omega}} = \tilde{\omega}_{,\sigma} = 0, \qquad F^{\mathcal{BD}}_{A_\varphi} = A_{\varphi,\sigma} = 0, \qquad F^{\mathcal{BD}}_{\tilde{A}_t} = \tilde{A}_{t,\sigma} = 0.$$

- $\mathcal{A} \cap \mathcal{B}$: $(\sigma, \tau) = (0, 1)$
  In (σ, τ)-coordinates, (2.46) at the centre of the disc becomes

$$F^{\mathcal{AB}} = \tilde{\nu} - e^{\nu^c} = 0. \tag{3.15}$$

3.2.2 Initial Guess

Although the spectral method provides a good approximation, the choice of initial guess is essential since if the initial guess is too far off from the actual solution, it leads to a divergence of the Newton-Raphson solver. For small γ and ε values, the post-Newtonian expansion of the potentials [14] are used as the initial data $\vec{f^{(0)}}$.

$$
\begin{aligned}
\phi &= 1 - \left[\frac{8}{3\pi}\text{arccot}\xi + \frac{4}{3\pi}\left(\frac{3\xi^2+1}{2}\text{arccot}\xi - \frac{3}{2}\xi\right)\left(3\eta^2-1\right)\right]\gamma, \\
a &= -\frac{\rho_0\sqrt{1-\varepsilon^2}}{\pi}\left(\eta^2-1\right)\left[\xi - 13\eta^2\xi + (3-15\eta^2)\xi^3 + (\xi^2+1)\left(3\eta^2(5\xi^2+1) - 3\xi^2+1\right)\text{arccot}\xi\right]\gamma^{\frac{3}{2}}, \\
A_\varphi &= \frac{a\varepsilon}{4}, \\
&= -\frac{\varepsilon\sqrt{1-\varepsilon^2}}{4\pi}\left(\eta^2-1\right)\left[\xi - 13\eta^2\xi + (3-15\eta^2)\xi^3 + (\xi^2+1)\left(3\eta^2(5\xi^2+1) - 3\xi^2+1\right)\text{arccot}\xi\right]\gamma^{\frac{3}{2}}, \\
A_t &= \frac{\varepsilon}{2}\left(\phi - 1\right), \\
&= -\varepsilon\left[\frac{4}{3\pi}\text{arccot}\xi + \frac{2}{3\pi}\left(\frac{3\xi^2+1}{2}\text{arccot}\xi - \frac{3}{2}\xi\right)\left(3\eta^2-1\right)\right]\gamma,
\end{aligned}
$$

with

$$
\tilde{\nu} = \sqrt{\frac{\phi\rho^2}{\rho^2 - a^2\phi^2}}, \qquad \tilde{\omega} = \frac{\rho_0}{e^{\nu c}}\left(\frac{a\phi^2}{\rho^2 - a^2\phi^2}\right), \qquad \tilde{A}_t = \frac{\rho_0}{e^{\nu c}}A_t. \tag{3.16}
$$

Here (η, ξ) is the elliptical coordinate, with $0 \leq \eta \leq 2\pi$ and $-\infty < \xi < \infty$, which is related to the Weyl coordinates as

$$
\begin{aligned}
\rho &= \rho_0\sqrt{1-\eta^2}\sqrt{1+\xi^2}, \\
\zeta &= \rho_0\eta\xi.
\end{aligned}
$$

The areas of the boundary conditions expressed in the elliptical coordinate are shown in figure 3.3, with plot (a) showing the whole space of the system. However, as discussed in section 2.4.1, due to the equatorial symmetry, only one side of the equatorial plane requires consideration, where the upper part is chosen, and the boundary conditions can thus be expressed in plot (b) as

- $\mathcal{A}$: $\eta = 1$, $0 \leq \xi < \infty$,
- $\mathcal{B}$: $0 \leq \eta \leq 1$, $\xi = 0$,
- $\mathcal{C}$: $r^2 = \rho^2 + \zeta^2 = {\rho_0}^2\left(1 - \eta^2 + \xi^2\right) \to \infty$, with $\eta \in [-1, 1]$, we have $\xi \to \infty$,
- $\mathcal{D}$: $\eta = 0$, $0 \leq \xi < \infty$),

The transformation between the elliptical coordinates (η, ξ) and the spectral coordinates (σ, τ) are [27]

$$
\eta = \sqrt{\tau}, \qquad \xi = \tan\left(\frac{\pi}{2}\sigma\right).
$$

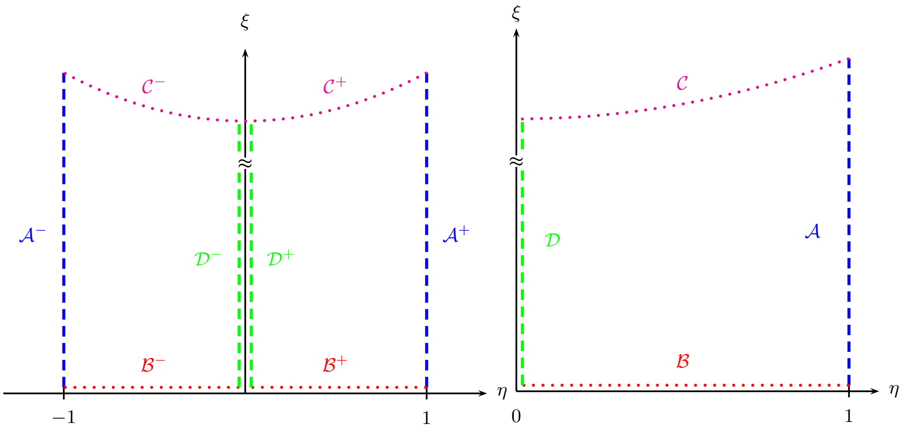

(a) (b)

Figure 3.3: Boundary conditions expressed in the elliptical coordinate. (a) The whole area. (b) The upper part of the equatorial plane. Area $\mathcal{A}$ (ζ-axis in Weyl coordinates): $\eta = 0$, $\xi \in [0, \infty)$; Area $\mathcal{B}$ (On the disc): $\eta \in [0, 1]$, $\xi = 0$; Area $\mathcal{C}$ (Infinity): $\eta \in [0, 1]$, $\xi \to \infty$; Area $\mathcal{D}$ (On the ρ-axis outside of the disc): $\eta = 0$, $\xi \in [0, \infty)$.

The initial data expressed in the spectral coordinates are thus

$$\begin{aligned}
\phi &= \frac{1}{2\pi\cos^2}\Big\{\pi + 4\pi\gamma(\sigma-1)\tau + \pi\big[1-2\gamma(\sigma-1)(\tau-1)\big]\cos(\pi\sigma) + 2\gamma(3\tau-1)\sin(\pi\sigma)\Big\},\\
a &= -\frac{\gamma^{3/2}\rho_0(\tau-1)\sqrt{1-\varepsilon^2}}{2\pi\cos^4}\cdot\\
&\qquad \Big\{\pi(\sigma-1)\left[(6\tau-2)\cos(\pi\sigma) - 9\tau + 1\right] + \big[(\tau-1)\cos(\pi\sigma) - 14\tau + 2\big]\sin(\pi\sigma)\Big\},\\
A_\varphi &= \frac{a\varepsilon}{4},\\
A_t &= \frac{\varepsilon}{2}(\phi - 1),
\end{aligned}$$

and together with (3.16), the initial data for the code is obtained.

For larger γ or ε, the Post-Newtonian initial data is not sufficient enough to be used as an initial guess, instead, iteration towards larger γ and ε by using the results generated from the previous smaller γ and ε are used as the new initial guess.

3.2.3 Vector Field

The system has 4 fields $\tilde{\nu}$, $\tilde{\omega}$, A_φ, $\tilde{A}_t$ in 2 dimensions (σ, τ), plus 1 additional field contributed to by the angular velocity Ω. The total number of equations or fields is thus according to (3.7)

$$N_{total} = 4(N_\sigma + 1)(N_\tau + 1) + 1.$$

All the unknown fields can be built up into a column vector

$$\vec{f} = \Big(\tilde{\nu}(i,j)\ \tilde{\omega}(i,j)\ A_\varphi(i,j)\ \tilde{A}_t(i,j)\ |\ \Omega\Big)^{\mathrm{T}} \text{ for } i = 0\cdots N_\sigma, j = 0\cdots N_\tau.$$

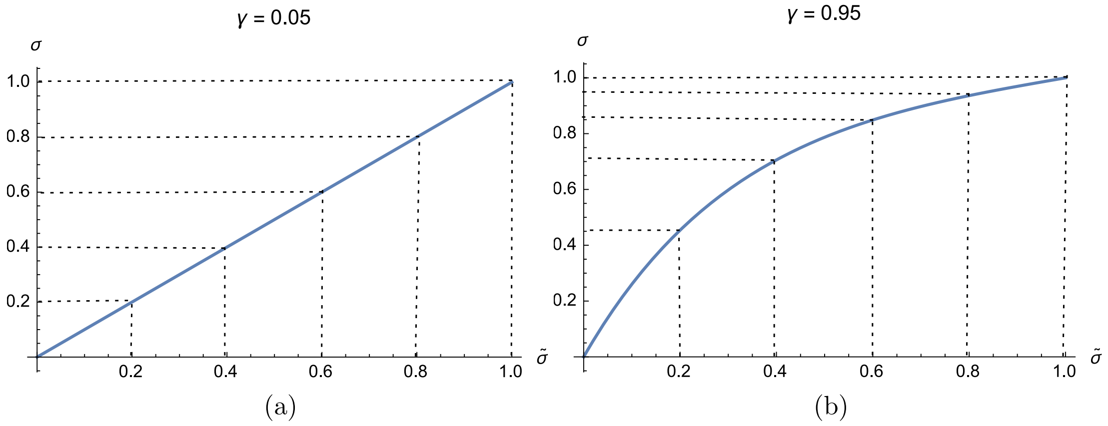

(a) (b)

Figure 3.4: Analytical mesh-refinement, with $\sigma(\tilde{\sigma}) = 1 - \frac{\sinh[\kappa(1-\tilde{\sigma})]}{\sinh(\kappa)}$ with $\kappa \sim |\ln(1-\gamma)|$. As the model goes more relativistic, i.e. as γ grows larger, the new-mesh points are distributed more densely near $\sigma = 1$. (a): Near the Newtonian limit, the grid point distribution is near equidistance. (b): At the relativistic limit, the distribution of the mesh points are more concentrated near $\sigma = 1$.

Note that the angular velocity Ω depends on γ and ε, and can therefore not be treated as a free parameter but as an auxiliary unknown. It comes into the field equation system from (2.14) and (2.17). The other variable σ_p is connected with Ω via (2.32)-(2.35), and can be gathered after Ω is obtained.

Using the initial data in section 3.2.2, a vector $\vec{f_0}$ is built up, which can be used as the initial guess for the Newton-Raphson method.

3.2.4 Analytical Mesh-Refinement

At the ultra-relativistic limit $\gamma \to 1$, the functions change drastically and thus form a steep gradient near $\sigma = 1$, unless one applies a finer grid on the area where the functions drastically change, the steep gradient will lead to the divergence of the solver.

There are two ways of dealing with this problem, one is to increase the grid points N_σ, which however will slow down the speed of the solver, since higher number of grid points means larger Jacobi matrix, in which inverting its matrix $\left[\hat{J}(\vec{f_m})\right]^{-1}$ in (3.8) is the crucial step in terms of the calculation time of the code.

This is the reason why the other method, the analytical mesh-refinement method, is more suitable for solving the numerical gradient problem. It keeps the number of the grid $N_{\tilde{\sigma}} = N_\sigma$, but redistributes the distance between the grid points. The spectral grid is no longer just being distributed via (3.6), but also depends on the specific need in terms of the configuration of the function.

In the case presented here, the grid is redistributed in a such way such that, while still running from 0 to 1, more grid points are concentrated near $\sigma \to 1$, the following alternation of mesh points thus satisfy the criteria[29]

$$\sigma(\tilde{\sigma}) = 1 - \frac{\sinh[\kappa(1-\tilde{\sigma})]}{\sinh(\kappa)}, \quad \text{with} \quad \kappa \sim |\ln(1-\gamma)|, \tag{3.17}$$

which rescales the spectral coordinates and thus “smoothens” the gradient, which prevents the divergence. Like σ-coordinate, $\tilde{\sigma}$ also runs between 0 and 1, but the behaviour of the curve near 1 changes according to the degree of relativity γ.

As shown in figure 3.4, near the Newtonian limit, σ and $\tilde{\sigma}$ has a similar curve behaviour, when however approaching the relativistic limit, the $\tilde{\sigma}$ curve creates a smoother gradient near $\tilde{\sigma} \to 1$, which enables the possibility of condensing more grid points near $\sigma = 1$.

Chapter 4

Physical Quantities and Ergosphere

In order to present the results in a more straightforward manner, in this chapter the raw data obtained from the field equations are converted into the more intuitive properties such as mass M, angular momentum J, magnetic dipole moment μ_B and charge Q, and are discussed from the different perspectives of the observers. Applications of the physical properties such as the error application and gyromagnetic factor g are further discussed. Finally, the ergosphere and how to extract numerically from the raw field are discussed.

4.1 Physical Quantities

4.1.1 Far Field Behaviour

The physical quantities are the asymptotic far-field behaviour of the potential which are obtained by the multipole expansion.

$$\begin{aligned}
&\nu = -\frac{M}{r} + \mathcal{O}(r^{-2}), \qquad \omega = \frac{2J}{r^3} + \mathcal{O}(r^{-4}), \qquad \alpha = -\nu + \mathcal{O}(r^{-2}) \\
&A_\varphi = \frac{\mu_B \sin^2\theta}{r} + \mathcal{O}(r^{-2}), \qquad A_t = -\frac{Q}{r} + \mathcal{O}(r^{-2}),
\end{aligned}$$

Expressed in the rescaled potentials as in section 3.2.1

$$\tilde{\nu} := e^{\nu}, \qquad \tilde{\alpha} := e^{\alpha}, \qquad \tilde{\omega} := \frac{\rho_0}{e^{\nu_c}}\omega, \qquad \tilde{A}_t := \frac{\rho_0}{e^{\nu_c}}A_t,$$

we have

$$\begin{aligned}
&\tilde{\nu} = 1 - \frac{M}{r} + \mathcal{O}(r^{-2}), \qquad \tilde{\omega} = \frac{2J}{r^3} + \mathcal{O}(r^{-4}), \qquad \tilde{\alpha} = -\tilde{\nu} + \mathcal{O}(r^{-2}) \\
&A_\varphi = \frac{\mu_B \sin^2\theta}{r} + \mathcal{O}(r^{-2}), \qquad \tilde{A}_t = -\frac{Q}{r} + \mathcal{O}(r^{-2}),
\end{aligned}$$

In other words

$$\begin{aligned} M &= -\lim_{r\to\infty}(r\nu) = -\lim_{r\to\infty}\left[r\left(\tilde{\nu}-1\right)\right], \\ J &= \lim_{r\to\infty}\left(\frac{r^3\omega}{2}\right) = \lim_{r\to\infty}\left(\frac{r^3\tilde{\omega}}{2}\right), \\ Q &= -\lim_{r\to\infty}(rA_t) = -\lim_{r\to\infty}\left(r\tilde{A}_t\right), \\ \mu_B &= \lim_{r\to\infty}\left(\frac{rA_\varphi}{\sin^2\theta}\right), \end{aligned}$$

Since the far-field behaviour is spherically symmetric, without loss of generality, the properties on the equatorial plane $\theta = \frac{\pi}{2}$: $\rho = r, \zeta = 0$ with

$$\rho = r\sin\theta, \qquad \zeta = r\cos\theta$$

are discussed. The physical quantities in cylindrical coordinate is thus

$$\begin{aligned} M &= -\lim_{\rho\to\infty}(\rho\nu) = -\lim_{\rho\to\infty}\left[\rho\left(\tilde{\nu}-1\right)\right], \\ J &= \lim_{\rho\to\infty}\left(\frac{\rho^3\omega}{2}\right) = \lim_{\rho\to\infty}\left(\frac{\rho^3\tilde{\omega}}{2}\right), \\ Q &= -\lim_{\rho\to\infty}(\rho A_t) = -\lim_{\rho\to\infty}\left(\rho\tilde{A}_t\right), \\ \mu_B &= \lim_{\rho\to\infty}\left(\frac{\rho A_\varphi}{\sin^2\theta}\right). \end{aligned} \tag{4.1}$$

The quantities in the spectral coordinates (σ, τ) are expressed for numerical purposes

$$\rho = \frac{\rho_0\sqrt{1-\tau}}{\cos\left(\frac{\pi}{2}\sigma\right)}, \qquad \zeta = \rho_0\sqrt{\tau}\tan\left(\frac{\pi}{2}\sigma\right).$$

Therefore, the physical properties are again transformed into spectral coordinates, which leads to the following discussion:

As mentioned above, without loss of generality, the discussion can be concentrated the equatorial plane. The infinity in the equatorial plane $(\rho \to \infty, \zeta = 0)$ is in area $\mathcal{D}$ of figure 3.2, which, expressed in the spectral coordinates is $(\sigma = 1, \tau = 0)$. Here, the physical quantities are individually discussed:

- Mass M:

$$M = -\lim_{r\to\infty}(r\nu) \overset{\theta=\frac{\pi}{2}}{=} -\lim_{\rho\to\infty}(\rho\nu) \overset{\tau=1}{=} -\lim_{\sigma\to 1}\frac{\rho_0\nu}{\cos\left(\frac{\pi}{2}\sigma\right)}.$$

  As discussed in previous chapters, at infinity $\nu = 0$, with both numerator and denominator tending to 0 when $\sigma \to 1$, the l'Hôpital rule can be applied, which yields

$$M \overset{\text{L'Hôpital}}{=} -\lim_{\sigma\to 1}\frac{\rho_0\nu_{,\sigma}}{-\frac{\pi}{2}\sin\left(\frac{\pi}{2}\sigma\right)} = \frac{2}{\pi}\rho_0\nu_{,\sigma}(1,0)\left[= \frac{2}{\pi}\rho_0\frac{\tilde{\nu}_{,\sigma}}{\tilde{\nu}}(1,0)\right].$$

- Angular momentum J:

$$
\begin{aligned}
J &= \lim_{r\to\infty}\left(\frac{r^3\omega}{2}\right) \overset{\theta=\frac{\pi}{2}}{=} -\lim_{\rho\to\infty}\left(\frac{\rho^3\omega}{2}\right) \overset{\tau=1}{=} -\lim_{\sigma\to 1}\frac{{\rho_0}^3\omega}{\cos^3\left(\frac{\pi}{2}\sigma\right)} \\
&\overset{\text{L'Hôpital}}{=} \lim_{\sigma\to 1}\frac{\rho^3\omega_{,\sigma}}{-3\frac{\pi}{2}\cos^2\left(\frac{\pi}{2}\sigma\right)\sin\left(\frac{\pi}{2}\sigma\right)} \\
&\overset{\text{L'Hôpital}}{=} \lim_{\sigma\to 1}\frac{\rho^3\omega_{,\sigma\sigma}}{-\frac{3}{4}\pi^2\cos^3\left(\frac{\pi}{2}\sigma\right)+\frac{3}{2}\pi^2\cos\left(\frac{\pi}{2}\sigma\right)\sin^2\left(\frac{\pi}{2}\sigma\right)} \\
&\overset{\text{L'Hôpital}}{=} \lim_{\sigma\to 1}\frac{\rho^3\omega_{,\sigma\sigma\sigma}}{\frac{21}{8}\pi^3\cos^2\left(\frac{\pi}{2}\sigma\right)\sin\left(\frac{\pi}{2}\sigma\right)-\frac{3}{4}\pi^3\sin^3\left(\frac{\pi}{2}\sigma\right)} \\
&= -\frac{4{\rho_0}^3}{3\pi^3}\omega_{,\sigma\sigma\sigma}(1,0)\left[= -\frac{4e^{\nu^c}{\rho_0}^2}{3\pi^3}\tilde{\omega}_{,\sigma\sigma\sigma}(1,0)\right].
\end{aligned}
$$

- Magnetic dipole moment μ_B:

$$
\begin{aligned}
\mu_B &= \lim_{r\to\infty}\left(\frac{rA_\varphi}{\sin^2\theta}\right) \overset{\theta=\frac{\pi}{2}}{=} -\lim_{\rho\to\infty}\left(\rho A_\varphi\right) \overset{\tau=1}{=} -\lim_{\sigma\to 1}\frac{\rho_0 A_\varphi}{\cos\left(\frac{\pi}{2}\sigma\right)} \\
&\overset{\text{L'Hôpital}}{=} \lim_{\sigma\to 1}\frac{\rho_0 A_{\varphi,\sigma}}{-\frac{\pi}{2}\sin\left(\frac{\pi}{2}\sigma\right)} = -\frac{2}{\pi}\rho_0 A_{\varphi,\sigma}(1,0).
\end{aligned}
$$

- Charge Q:

$$
\begin{aligned}
Q &= -\lim_{r\to\infty}\left(rA_t\right) \overset{\theta=\frac{\pi}{2}}{=} -\lim_{\rho\to\infty}\left(\rho A_t\right) \overset{\tau=1}{=} -\lim_{\sigma\to 1}\frac{\rho_0 A_t}{\cos\left(\frac{\pi}{2}\sigma\right)}. \\
&\overset{\text{L'Hôpital}}{=} -\lim_{\sigma\to 1}\frac{\rho_0 A_{t,\sigma}}{-\frac{\pi}{2}\sin\left(\frac{\pi}{2}\sigma\right)} = \frac{2}{\pi}\rho_0 A_{t,\sigma}(1,0)\left[= \frac{2}{\pi}e^{\nu^c}\tilde{A}_{t,\sigma}(1,0)\right].
\end{aligned}
$$

The physical proprieties expressed in the spectral coordinates and in terms of the rescaled fields $(\tilde{\nu}, \tilde{\omega}, A_\varphi, \tilde{A}_t)$ are obtained. Using the coordinate transformation (3.4) and the fact that for the far-field equatorial plane, $(\rho \to \infty, \zeta = 0)$ corresponds to $(\sigma \to 1, \tau = 0)$, yields the solutions

$$
\begin{aligned}
M &= \frac{2}{\pi}\rho_0\frac{\tilde{\nu}_{,\sigma}}{\tilde{\nu}}(1,0), \qquad J = -\frac{4e^{\nu^c}{\rho_0}^2}{3\pi^3}\tilde{\omega}_{,\sigma\sigma\sigma}(1,0), \\
Q &= \frac{2}{\pi}e^{\nu^c}\tilde{A}_{t,\sigma}(1,0), \qquad \mu_B = -\frac{2}{\pi}\rho_0 A_{\varphi_\sigma}(1,0).
\end{aligned}
\tag{4.2}
$$

4.1.2 Normalising the physical quantities through Ω and ρ_0

Depending on which perspective one observes for the system, that is, from the asymptotic-flat region or the region near the disc, one chooses different parameters of normalisation.

From the perspective of the asymptotic-flat region, one tends to normalise the angular velocity of the disc Ω, whereas at the near-source region, one tends to normalise the coordinate radius of the disc ρ_0. However, the choice is merely the matter of normalisation, and does not effect the the outcome of the result, as shown in the following, but in order to obtain an explicit expression, it depends on the point of view from which one observes the system, as is shown in the next chapter. Since the physical quantities are derived from the far-field behaviour, one should also observe them through the far-field perspective in order to gain a meaningful expression.

Parametrisation and Normalisation

The solution of the model is formed in the Lewis-Papapetrou-Weyl metric (2.6)

$$ds^2 = e^{2\alpha}(d\rho^2 + d\zeta^2) + W^2 e^{-2\nu}(d\varphi - \omega dt)^2 - e^{2\nu}dt^2.$$

Expressing the metric in the new rescaled potentials as in section 3.2.1

$$\tilde{\nu} := e^{\nu}, \qquad \tilde{\alpha} := e^{\alpha}, \qquad \tilde{\omega} := \frac{\rho_0}{e^{\nu_c}}\omega,$$

the new metric form becomes

$$ds^2 = \tilde{\alpha}^2(d\rho^2 + d\zeta^2) + \frac{\rho^2}{\nu^2}(d\varphi - \frac{e^{\nu_c}}{\rho_0}\tilde{\omega}dt)^2 - \tilde{\nu}^2 dt^2.$$

Parametrising the potentials and coordinates to be

$$\tilde{\nu} = \bar{\nu}, \qquad \tilde{\omega} = \frac{\bar{\omega}}{\lambda}, \qquad \tilde{\alpha} = \frac{\bar{\alpha}}{\lambda}, \tag{4.3}$$

and

$$\rho = \lambda\bar{\rho}, \qquad \zeta = \lambda\bar{\zeta}, \qquad \varphi = \frac{\bar{\varphi}}{\lambda}, \qquad t = \bar{t}, \tag{4.4}$$

the parametrised metric becomes

$$\begin{aligned} ds^2 &= \frac{\bar{\alpha}^2}{\lambda^2}\left(\lambda^2 d\bar{\rho}^2 + \lambda^2 d\bar{\zeta}^2\right) + \frac{\lambda^2\bar{\rho}^2}{\bar{\nu}^2}\left(\frac{d\bar{\varphi}}{\lambda} - \frac{e^{\nu_c}}{\rho_0}\frac{\bar{\omega}}{\lambda}d\bar{t}\right)^2 - \bar{\nu}^2 d\bar{t}^2 \\ &= ds^2 = \bar{\alpha}^2(d\bar{\rho}^2 + d\bar{\zeta}^2) + \frac{\bar{\rho}^2}{\bar{\nu}^2}(d\bar{\varphi} - \frac{e^{\nu_c}}{\rho_0}\bar{\omega}d\bar{t})^2 - \bar{\nu}^2 d\bar{t}^2, \end{aligned}$$

which preserves the same form as before.

Furthermore, inspecting the four-velocity in (2.14)

$$u = e^{-V}\left(\frac{\partial}{\partial t} + \Omega\frac{\partial}{\partial\varphi}\right),$$

with

$$\frac{\partial}{\partial t} = \frac{\partial\bar{t}}{\partial t}\frac{\partial}{\partial\bar{t}} = \frac{\partial}{\partial\bar{t}}, \qquad \frac{\partial}{\partial\varphi} = \frac{\partial\bar{\varphi}}{\partial\varphi}\frac{\partial}{\partial\bar{\varphi}} = \frac{\partial}{\partial\bar{\varphi}},$$

the four-velocity becomes

$$u = e^{-V}\left(\frac{\partial}{\partial\bar{t}} + \Omega\lambda\frac{\partial}{\partial\bar{\varphi}}\right),$$

The new angular velocity can thus be extracted

$$\bar{\Omega} \equiv \Omega\lambda. \tag{4.5}$$

Comparing the product of the angular velocity Ω and the coordinates (ρ, φ)

$$\bar{\rho}\bar{\Omega} = \frac{\rho}{\lambda}\Omega\lambda = \rho\Omega, \qquad \bar{\zeta}\bar{\Omega} = \frac{\zeta}{\lambda}\Omega\lambda = \zeta\Omega, \tag{4.6}$$

one sees that they remain invariant under the parametrisation, meaning that the choice of normalisation of either Ω or ρ_0 does not influence the outcome of the result. The expression of the result however depends on the point of view of the observer, as will be shown in the next chapter when the result is discussed.

Parametrising the physical quantities

The parametrisation for mass M and angular momentum J are derived from (4.1), (4.3) and (4.4), which yields

$$\bar{M} = \frac{M}{\lambda}, \qquad J = \frac{\bar{J}}{\lambda^2}.$$

For Charge Q and Magnetic dipole moment μ_B, which are obtained from the far-field behaviour of A_t and A_φ, the vector potential

$$\mathbf{A} = A_\varphi d\varphi + A_t dt = \bar{A}_\varphi d\bar{\varphi} + \bar{A}_t d\bar{t} = \bar{A}_\varphi \lambda d\varphi + \bar{A}_t dt$$

must first be inspected, yielding

$$A_\varphi = \lambda\bar{A}_\varphi, \qquad A_t = \bar{A}_t. \tag{4.7}$$

It is thus possible to obtain the parametrisation of charge Q and magnetic dipole moment μ_B via (4.1), (4.4) and (4.7), which gives

$$\bar{Q} = \frac{Q}{\lambda}, \qquad \mu_B = \frac{\bar{\mu_B}}{\lambda^2}.$$

Normalisation

One chooses different normalisations depending on the perspective of the observer. For the far field observer, one normalises with Ω, whereas for the near-source observer one normalises with ρ_0. The following is the discussion of the two normalisations.
From (4.6), one has

$$\rho_0\Omega = \bar{\rho}_0\bar{\Omega}. \tag{4.8}$$

- For the far-field perspective: $\bar{\Omega} = 1$, with (4.8) and (4.4), one gets

$$\Omega = \frac{\bar{\rho}_0}{\rho_0} = \frac{1}{\lambda}. \tag{4.9}$$

- For the near-source perspective: $\bar{\rho}_0 = 1$, with (4.8) and (4.4), one gets

$$\rho_0 = \frac{\bar{\Omega}}{\Omega} = \lambda. \tag{4.10}$$

Normalising the physical quantities

The physical quantities are normalised according to the perspective of the observer. As discussed previously,

- For the far-field observer with (4.9), the normalisation for the physical proprieties are thus
$$\bar{M} = \Omega M, \qquad \bar{J} = \Omega^2 J, \qquad \bar{\mu_B} = \Omega^2 \mu_B, \qquad \bar{Q} = \Omega Q. \tag{4.11}$$
- For the near-source observer with (4.10), one has the normalisation as
$$\bar{M} = \frac{M}{\rho_0}, \qquad \bar{J} = \frac{J}{{\rho_0}^2}, \qquad \bar{\mu_B} = \frac{\mu_B}{{\rho_0}^2}, \qquad \bar{Q} = \frac{Q}{\rho_0}. \tag{4.12}$$

The physical quantities deliver a more meaningful expression when observed from the far-field perspective, since they are derived from the asymptotic behaviour of the fields $\tilde{\nu}$, $\tilde{\omega}$, A_φ and $\tilde{A}_t$, as will be seen in the next chapter.

4.1.3 Parameter Relation and Error

From [23, 14, 15] and using (2.42) and (2.47), these physical quantities have the following relation

$$\begin{aligned} M &= 2\Omega J + D\frac{Q}{\varepsilon} \\ &= 2\Omega J + \left(\frac{1-\gamma}{\varepsilon} + A_t^c\right) Q, \end{aligned} \tag{4.13}$$

with the baryonic mass $M_0 = \frac{Q}{\varepsilon}$ and A_t^c the field A_t at the centre of the disc.

Since (4.13) consists of the physical quantities, which are derived from the raw field $\tilde{\nu}$, $\tilde{\omega}$, A_φ, and $\tilde{A}_t$, which are in turn derived from the field equations and the boundary conditions, it can be served as an accuracy test. The relation can thus be rewritten into

$$Error = \left| 1 - \left[\frac{2\Omega J}{M} + \left[\frac{1-\gamma}{\epsilon} - A_t^c \right] \frac{Q}{M} \right] \right|. \tag{4.14}$$

If the Error tends to 0, showing that the physical quantities provides an accurate result, it will also indirectly justify the correctness of the choice of the raw potential and the formation of the equation system. The results and discussion are shown in the next chapter.

4.1.4 Gyromagnetic Factor g

The gyromagnetic factor(g-factor), defined by

$$g = 2\frac{M}{Q}\frac{\mu_B}{J},$$

is a dimensionless quantity that describes the ratio between the physical quantities of a system, in this case the physical quantities are the mass M, charge Q, angular momentum J and magnetic moment μ_B.

Originally, the g-factor was used to describe the characteristics of a particle in classical electrodynamics and quantum mechanics. In the classical limit, all convective systems[1] have $g = 1$ [30]. Notable is the g-factor of a spin-$\frac{1}{2}$ particle, for instance a single isolated electron or a muon in which both have a gyromagnetic factor of $g \approx 2$, and from the Dirac equation, the spin of the electron automatically fulfills $g = 2$. [31, 32].

The gyromagnetic factor also coincidentally has $g = 2$ in many cases in general relativity [33, 34, 35, 36, 37], implying a possible aspect of investigating the link between the general relativistic and quantum regimes.

In fact, there are some studies devoted specifically to this topic, in which systems have both relativistic and quantum characteristics. Systems including gravitational fields and non-negligible strong field effects are investigated in [38].

For Einstein-Maxwell equations, any electro-vacuum solution which can be obtained from a pure vacuum solution via an $SU(2,1)$ invariance transformation also has the value of $g = 2$ [21, 39, 40]. The charged disc solution cannot however be obtained directly from the non-charged disc case via the invariance transformation, however, with the help of the numerical method applied in this work, it is possible to see how the g-factor of the system evolves.

For the case of rotating disc of charged dust, this argument is also supported by [15] at the near Newtonian limit. For the more relativistic region and up to the ultra-relativistic region, the numerical result delivers high precision, as will be seen in the next chapter.

4.2 Ergosphere

The ergosphere can be considered as the area within a static limit surface of a black hole $\xi_i \xi^i = g_{tt} = 0$, beyond which the local inertial frames of reference are dragged round the surface of the horizon

$$\xi_i \xi^i = g_{tt} \geq 0. \tag{4.15}$$

Inside the ergosphere, all timelike geodesics rotate with the graviational source and the Killing vector representing stationarity ξ_i becomes spacelike.

For the case of stationarity and axissymmetric, the surface of ergosphere according to (2.15a) is expressed as

$$g_{tt} = -e^{2\nu} + \omega^2 \rho^2 e^{-2\nu} \overset{!}{=} 0.$$

Written in the rescaled potentials as in section 3.2.1

$$\tilde{\nu} := e^{\nu}, \qquad \tilde{\alpha} := e^{\alpha}, \qquad \tilde{\omega} := \frac{\rho_0}{e^{\nu_c}} \omega, \qquad \tilde{A}_t := \frac{\rho_0}{e^{\nu_c}} A_t,$$

---

[1] Systems where the ratio of charge and mass density is constant, and where the mass and charge elements have equal velocities, which satisfy $v \ll c$.

and in the spectral coordinates

$$\rho = \frac{\rho_0\sqrt{1-\tau}}{\cos\left(\frac{\pi}{2}\sigma\right)}, \qquad \zeta = \rho_0\sqrt{\tau}\tan\left(\frac{\pi}{2}\sigma\right),$$

produces

$$g_{tt} = -\tilde{\nu}^2 + \frac{e^{2\nu^c}(1-\tau)}{\cos^2\left(\frac{\pi\sigma}{2}\right)}\frac{\tilde{\omega}^2}{\tilde{\nu}^2} \overset{!}{=} 0.$$

The field equations in section 3.2.1 first has to be solved in order to obtain $\tilde{\nu}(\sigma,\tau)$ and $\tilde{\omega}(\sigma,\tau)$ of the whole area. Then using the bisection method, which will be discussed in the following section, it was possible to find out the surface of the ergosphere, i.e. the $(\sigma_{ergo},\tau_{ergo})$'s, where $g_{tt}(\sigma_{ergo},\tau_{ergo})$=0 was obtained.

After obtaining the $(\sigma_{ergo},\tau_{ergo})$'s, the spectral coordinates can be converted back to the Weyl coordinates $(\rho_{ergo},\zeta_{ergo})$'s to obtain the more intuitive astrophysical position of the ergosphere.

The ergosphere of the non-charged case has been discussed in [16], in this work the calculation is extended to the charged case ranging all the way up to the ECD case.

4.2.1 Bisection Method

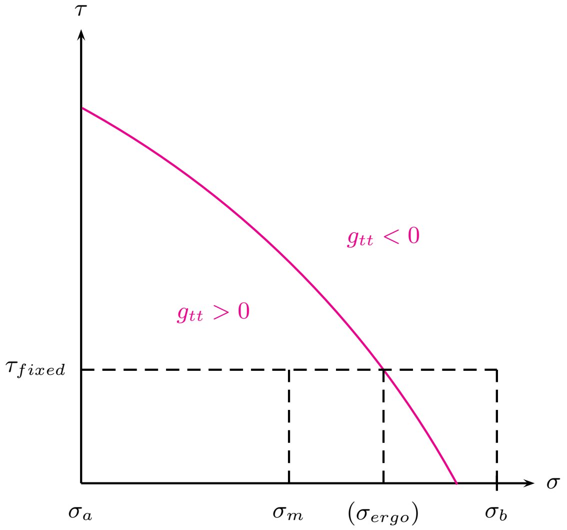

For a certain fixed τ, the σ_{ergo} is required, such that $g_{tt}(\sigma_{ergo},\tau_{fixed}) = 0$ is fulfilled. There are several numerical methods to obtain it[2], amongst these is the bisection method, which is sufficient to achieve this purpose. A brief description follows on how the method was applied to the method to the model.

Step (I): Between two known ends of σ_a and σ_b, in this case is $\sigma_a = 0$ and $\sigma_b = 1$, the middle point is taken

$$\sigma_{m0} = \frac{\sigma_a + \sigma_b}{2}$$

---

[2] Such as linear interpolation methods, Muller's method, fixed-point iteration method, Newton's method,...etc..

and obtain its g_{tt}

$$g_{tt}^{m0} = g_{tt}(\sigma_{m0}, \tau_{fixed}).$$

Additionally, the g_{tt}'s of σ_a is known

$$g_{tt}^{a} = g_{tt}(\sigma_a, \tau_{fixed}), \qquad g_{tt}^{b} = g_{tt}(\sigma_b, \tau_{fixed}).$$

Step (II): The comparison can be started as follows

(i) If $g_{tt}^{m0} \cdot g_{tt}^{a} < 0$, meaning g_{tt}^{m0} and g_{tt}^{a} have different plus-minus sign, it is known that σ_{ergo} lies between σ_a and σ_{m0}. As such, the new σ_b can be set to be σ_{m0}.

(ii) If $g_{tt}^{m0} \cdot g_{tt}^{a} > 0$, meaning that σ_{ergo} lies outside of the area between σ_a and σ_{m0}, and is instead within σ_{m0} and σ_b, the new σ_a can thus be set to be σ_{m0}.

Step (III): Now having new $\sigma_a^{(new)}$ and $\sigma_b^{(new)}$ depending on the two cases discussed in Step (II), the new σ_{m1} can be obtained

$$\sigma_{m1} = \frac{\sigma_a^{(new)} + \sigma_b^{(new)}}{2},$$

and the new g_{tt}

$$g_{tt}^{m1} = g_{tt}(\sigma_{m1}, \tau_{fixed}).$$

(i) If $g_{tt}^{m1} < \delta$, with $\delta \to 0$, which can be defined numerically, then σ_{ergo} is found.

(ii) If $g_{tt}^{m1} > \delta$, the iteration is repeated with the new σ_{m1}.

After obtaining the σ_{ergo} where $g_{tt}(\sigma_{ergo}, \tau_{fixed}) = 0$, the calculation moves on to the next fixed τ in order to find the corresponding σ_{ergo}, until all the region of τ has been scanned through. In this case, τ runs from 0 to 1.

With all the $(\sigma_{ergo}, \tau_{ergo})$ obtained, the spectral coordinates can be converted to the Weyl coordinates $(\rho_{ergo}, \zeta_{ergo})$ in order to get a more intuitive physical perspective of the ergosphere. All the results will be shown in the next chapter.

Chapter 5

Results

Initially, the raw data of the equation system, where $\tilde{\nu}$, $\tilde{\omega}$, A_φ and $\tilde{A}_t$ are directly obtained will be looked at. Through the raw data, information about the physical quantities such as mass M, charge Q, angular momentum J and magnetic moment μ_B is acquired through far field expansions, which will be served as an accuracy test using the parameter relation (4.13). Furthermore, the physical quantities can be used to extract the gyromagnetic factor g.

Moreover, using the raw data, the information g_{tt} is obtained through (4.15), which helps find the configutation of the ergospheres and helps to discuss under what circumstances they are created.

Part of the results of the physical quantities, from the parameter relation and the gyromagnetic factor are published in [17].

5.1 Fields $\tilde{\nu}$, $\tilde{\omega}$, A_φ and $\tilde{A}_t$

The raw data are the information gathered directly from the outcome of the numerical calculation for the equation system in section 3.2.1, using the pseudo-spectral method and iterated with the Newton-Raphson method. Applying the analytical mesh-refinement, the convergence of the numerical code enhances from $\gamma \approx 0.8$ up to $\gamma \approx 0.99$.

Figure 5.1 shows a comparison of the field distribution between the charged and the uncharged discs, i.e. comparing different ε's with a fixed γ. In the figure we use $\gamma = 0.7$. The reason why a larger γ is chosen as a displaying example is due to the fact that, especially for the raw data $\tilde{\nu}$, one does not see a huge distinction between the charged and uncharged case, unless the γ is large enough. The ε, however, has a greater impact on the other raw potentials. For the non-charged case $\varepsilon = 0$, there are no A_φ and $\tilde{A}_t$. Once the parameter ε is triggered, one sees that the electromagnetic effect starts kicking in, which can also be seen in plot (c) and (d) in figure 5.1 .

For figure 5.2, different γ's are compared with the same ε, here $\varepsilon = 0.5$ was chosen. The $\gamma = 0.1$ case is again shown in the upper-left of every figure, since its curvature is graphically subdued by the larger γ's in the main diagrams. As one can see in the upper right plot of figure 5.2, the larger the γ, the greater the gradient of the plot. This is also the reason why a larger γ was chosen in 5.1 when different ε's are compared with a fixed γ, so that more significant changes can be seen in the fields.

Also as a reminder, and as shown in figure 3.2, $\sigma = 0$ represents the surface of the disc, $\sigma = 1$ implies infinity, $\tau = 0$ denotes the equatorial plane outside of the disc, and $\tau = 1$ is the area along the rotating axis $\zeta = 0$. As a coarse check up to see if the raw data give the correct outcome, it is seen that the fields fulfill the boundary condition (2.43) and (2.44) at infinity $\sigma = 1$.

Another possible check is at the centre of the disc, i.e., at $(\sigma, \tau) = (0, 1)$, acquired from (2.47) and (3.15), the raw data $\tilde{\nu}$ should have the following relation

$$\tilde{\nu} = 1 - \gamma, \tag{5.1}$$

which, for the results presented here also corresponds to plot (a) of figure 5.1, $\tilde{\nu}(0,1) = 0.3$ for $\gamma = 0.7$, and for plot (a) of figure 5.2, $\tilde{\nu}(0,1) = 0.9$, $\tilde{\nu}(0,1) = 0.3$ and $\tilde{\nu}(0,1) = 0.1$, for $\gamma = 0.1$, $\gamma = 0.7$ and $\gamma = 0.9$ respectively.

Moreover, the result also agrees with [14], where the post-Newtonian expansion was being carried out accurately for small γ and ε. An advantage of the numerical method is thus the higher precision of γ and ε up to 1, which will be discussed in section 5.5.

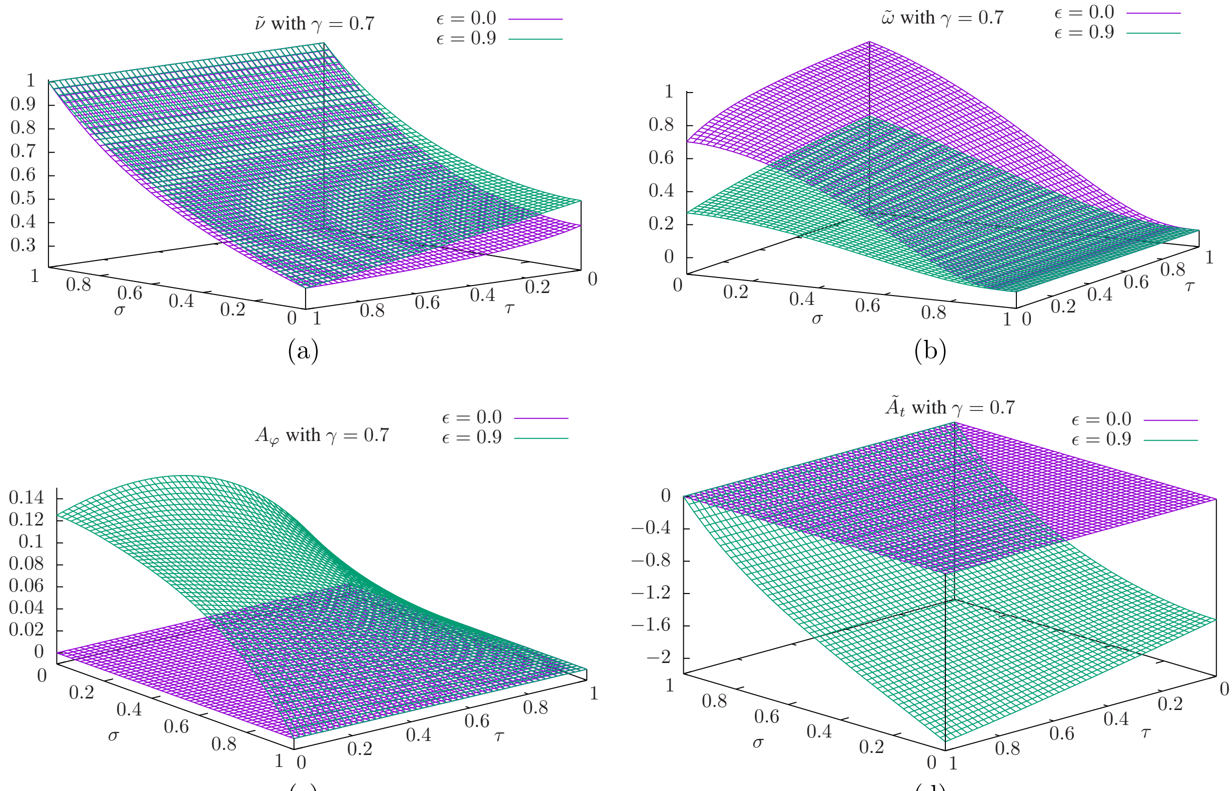

(a) (b) (c) (d)

Figure 5.1: Comparing the raw data $\tilde{\nu}$, $\tilde{\omega}$, A_φ and $\tilde{A}_t$ between the charged case (here $\varepsilon = 0.9$) and non-charged case ($\varepsilon = 0$), with $\gamma = 0.7$.

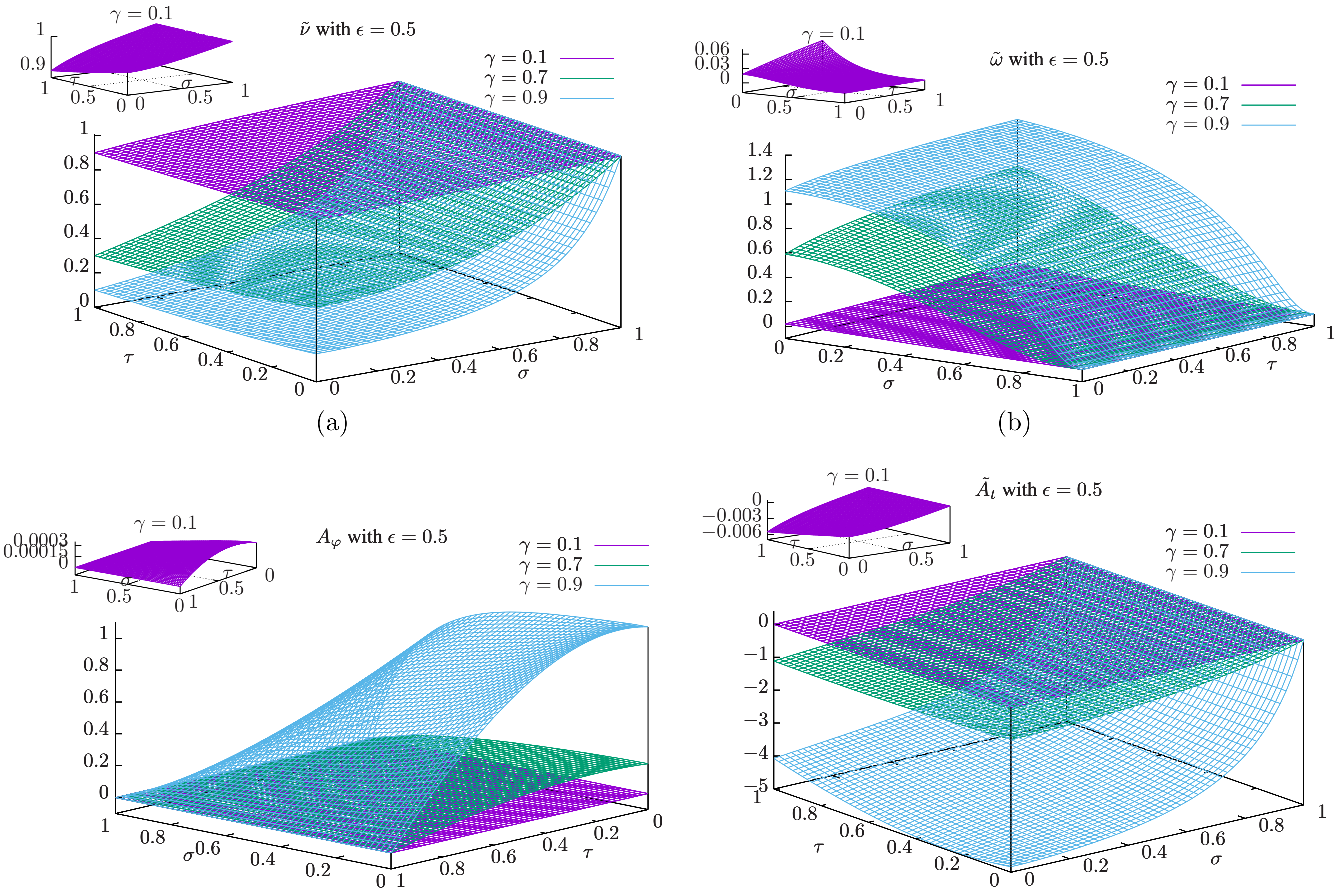

(a) (b)

(c) (d)

Figure 5.2: Comparing different γ's of the raw data $\tilde{\nu}$, $\tilde{\omega}$, A_φ and $\tilde{A}_t$ for $\varepsilon = 0.5$. Upper left of each figure is again highlighting the $\gamma = 0.1$ case.

5.2 Angular Velocity Ω

The other direct outcome from the equation system is the auxiliary parameter Ω, which represents the angular velocity. Ω is embedded in the boundary conditions of the disc(2.37) - (2.40) of the equation system.

Ω can be expressed in the parameter space (γ, ε), Figure 5.3 displays Ω in the complete (γ, ε).

As discussed in section 3.2.4, the analytical mesh-refinement for higher γ's is used. Applying the analytical mesh-refinement to the numerical code enhance the convergence value of the relativistic factor from $\gamma \approx 0.8$ up to $\gamma \approx 0.99$. Additionally, running the numerical code in smalller steps of γ and ε also helps prevent divergence of the calculations, which is why starting from $\gamma = 0.9$ in plot (a) of figure 5.3, the data grid appears to be denser, since $\Delta\gamma = \Delta\varepsilon = 0.01$ is used instead of 0.05.

For the rigid rotating disc, every fixed set of (γ, ε) gives a constant Ω. Plot (b) of figure 5.3 shows how Ω reacts with different ε's. One sees that an increase of the constant specific charge ε corresponds to a decrease of Ω, implying that the electromagnetic effect subdues the rotation of the disc. Plot (c) of figure 5.3 indicates the Ω with respect to different γ's. Note that at the beginning, Ω grows with an increase of γ until $\gamma \approx 0.39$, where Ω reaches its maximum. Afterwards it starts to decrease again, until the point which the system tends towards an ultra-relativistic $\gamma \to 1$, where the angular velocity decreases to almost 0.

5.3 Physical Quantities

As discussed in section 4.1, the physical quantities mass M, angular momentum J, magnetic moment μ_B and charge Q reflect the far-field behaviours of ν, ω, A_φ and A_t. Figures 5.5 to 5.8 show the physical quantities in the whole parameter space (γ, ε).

As discussed in the previous chapter, the expression of the physical quantities depends on the perspective of the observer. Since the physical quantities are derived from the far-field behaviour of the raw field, it makes more sense to observe them through the far-field perspective, meaning that they should be normalised by (4.11), i.e. $\lambda = \frac{1}{\Omega}$.

Normalising via ρ_0

Firstly, the case of observing the quantities from the near-source area by normalising via (4.12), i.e. $\lambda = \rho_0$ is examined. As shown in figure 5.4, at the Newtonian limit $\gamma \ll 0$, all physical quantities tend towards 0, whereas near the ultra-relativistic area, the physical quantities tend towards infinity, which cannot be physically interpreted, and thus it is shown that it is not suitable to interpret the physical quantities from a near-source perspective. Note that in the figures, due to the drastic increase of the properties near the ultra-relativistic region $\gamma \to 1$, the data are plotted in the logarithm form.

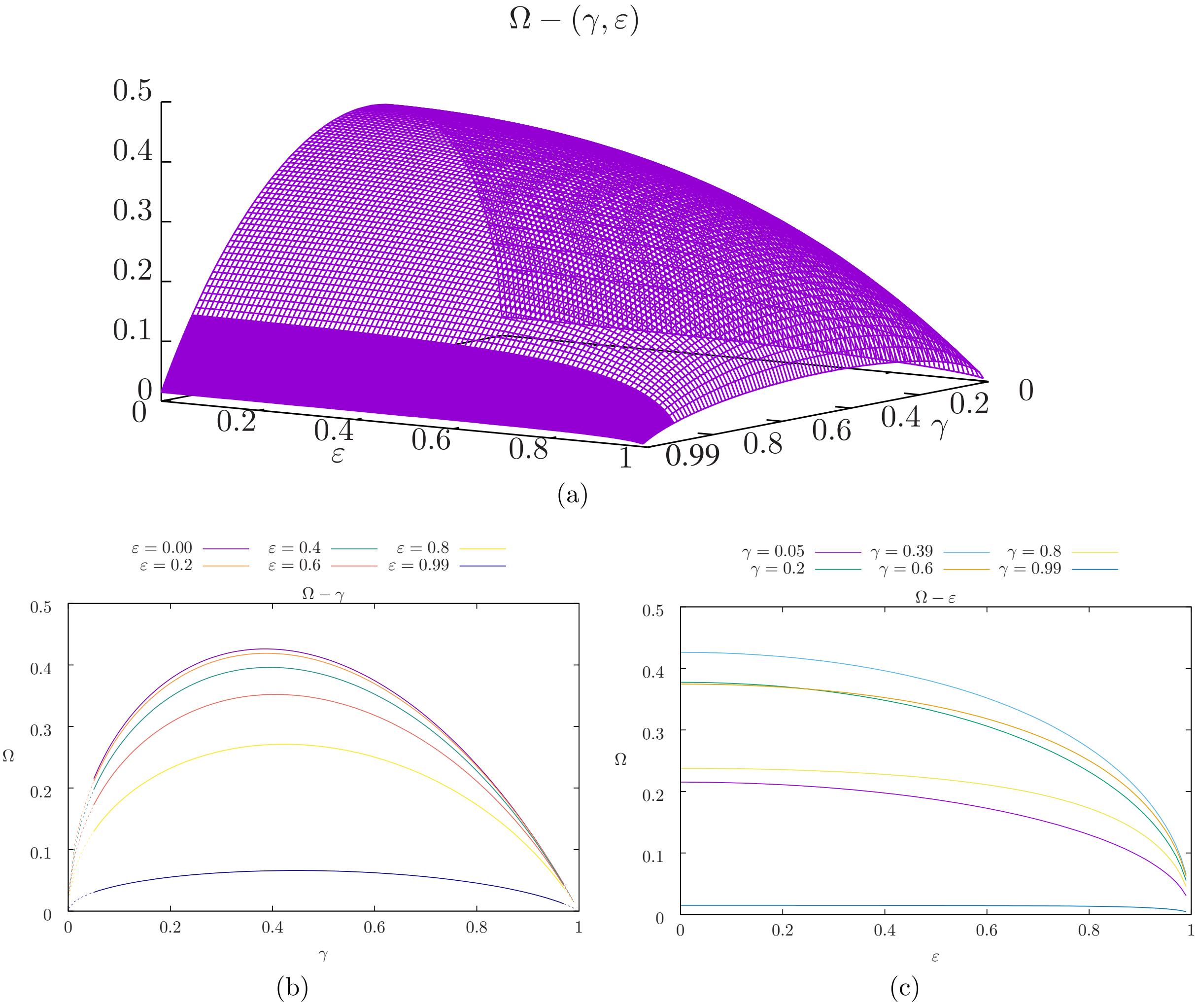

(a)

(b)

(c)

Figure 5.3: Angular velocity Ω. (a) Ω in the complete parameter space (γ, ε). (b) Ω - γ with different fixed ε's. (c) Ω - ε with different fixed γ's.

Normalising via Ω

On the other hand, if the physical quantities are normalised in terms of Ω, the results remain finite at the ultra-relativistic limit, as shown in figures 5.5 to 5.8. Note that the $\varepsilon = 0.0$ part of the result also coincides with the existing non-charged results, e.g. in [41], $\Omega M \to 0.5$ and $\Omega^2 \to 0.25$ at $(\varepsilon = 0, \gamma \to 1)$.

As for the electromagnetic influence, it is seen that the changing of the constant specific charge ε, even though influencing the quantity, does not influence the quality of the value. As can be seen from Figures 5.5(c) to 5.8(c), even though the magnitude changes, the form of the curves does not change significantly.

Inspecting the influence of the constant specific charge ε, it is interesting to see that for the cases of an uncharged rotating disc $\varepsilon \to 0$ and electrically counterpoised case $\varepsilon \to 1$, the physical quantities converge. Figures 5.5 to 5.8 show that for the case of $\varepsilon \to 0$, $Q = \mu_B = 0$ is observed as would be expected, since Q and μ_B are derived from A_t and A_φ, which contribute an electromagnetic effect and which when observed from Figure 5.2, one see that $A_t = A_\varphi = 0$. As for the case where $\varepsilon \to 1$, one notices that $J = \mu_B = 0$, which supports the fact that in the ECD case, the rotation of the disc ceases.

5.4 Error Calculation

As mentioned in section 4.1.3, the relationship of the physical quantities are connected through (4.13). Moreover, since the physical quantities M, J, μ_B and Q are acquired from the raw data field ν, ω, A_φ and A_t, and the raw data are in turn calculated directly from the field equations and the boundary conditions, and furthermore, the angular velocity Ω is also embedded in (4.13), which is an unknown parameter of the numerical code. Therefore, if (4.13) is satisfied, one can be assured that the result of the calculations, tracing all the way back to the equation system derivation, are consistent and correct, and that the numerical code has considered its purpose. (4.14) can therefore be served as an accuracy test for our results

$$Error = \left|1 - \left[\frac{2\Omega J}{M} + \left[\frac{1-\gamma}{\epsilon} - A_t^c\right]\frac{Q}{M}\right]\right|.$$

Figure 5.4 illustrates the result of (4.14), showing that the numerical method we used kept the accuracy up to

$$Error \leq 10^{-8}.$$

Above this order, the saturation is due to the machine precision.

The numerical accuracy of the spectral method depends on the higher derivatives of the variables. Amongst all the physical quantities, the angular momentum J, derived in 4.1.1, is obtained by the third derivatives of the spectral coordinates (γ, ε) of the raw data $J = -\frac{4e^{\nu^c}{\rho_0}^2}{3\pi^3}\tilde{\omega}_{,\sigma\sigma\sigma}$ as shown in (4.2), which is then the critical factor for the numerical errors.

Figure 5.10 presents the logarithm error for the accuracy test (4.2) with respect to γ. Until $\gamma \approx 0.90$, the error stays below 10^{-8}, then the machine error starts kicking

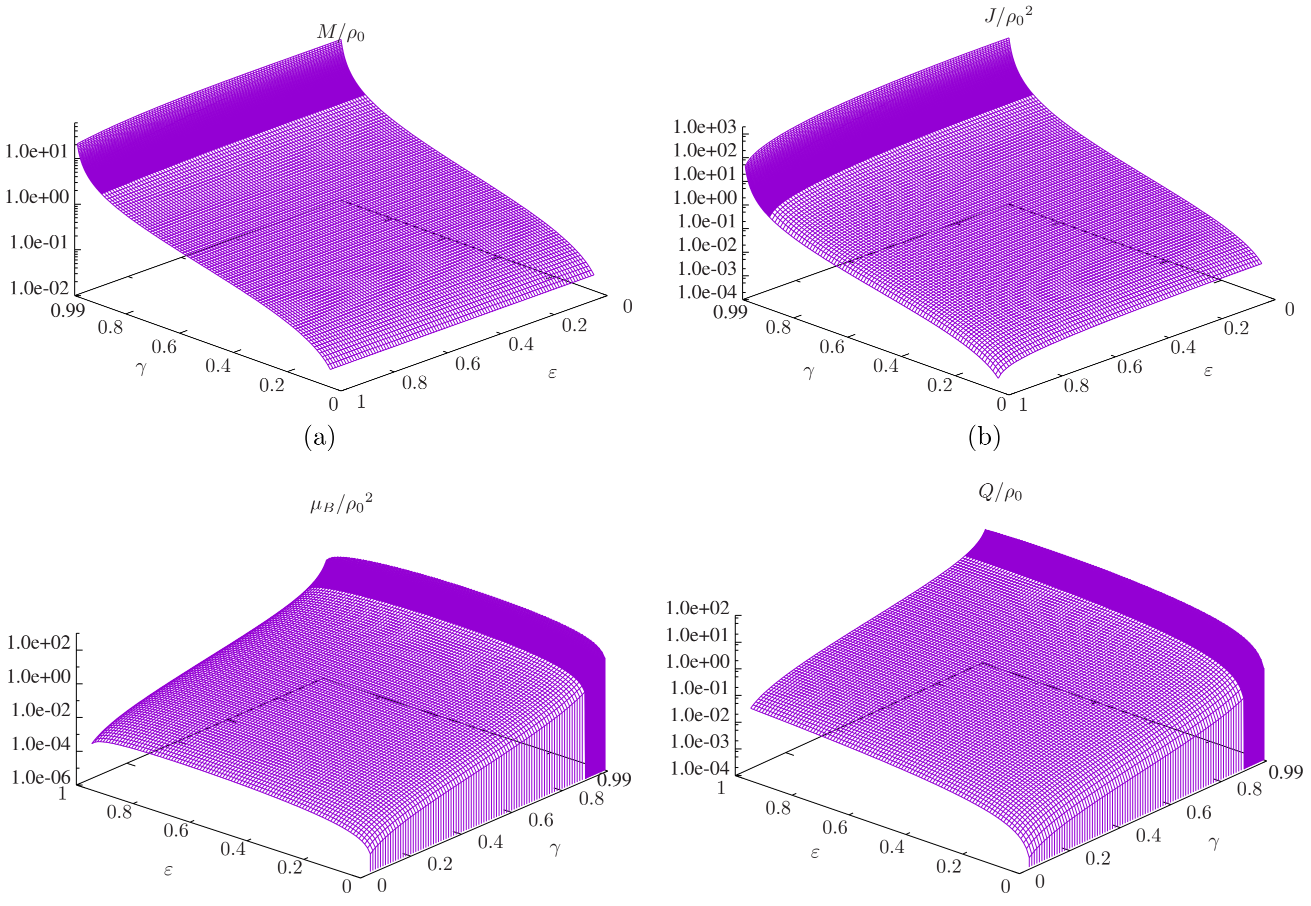

(a) (b) (c) (d)

Figure 5.4: Physical quantities normalised by ρ_0, due to the drastic increase in the proprieties at the ultra-relativistic region $\gamma \to 1$, the plots are shown in logarithm scale, with (a) mass (b) angular momentum (c) magnetic moment (d) charge.

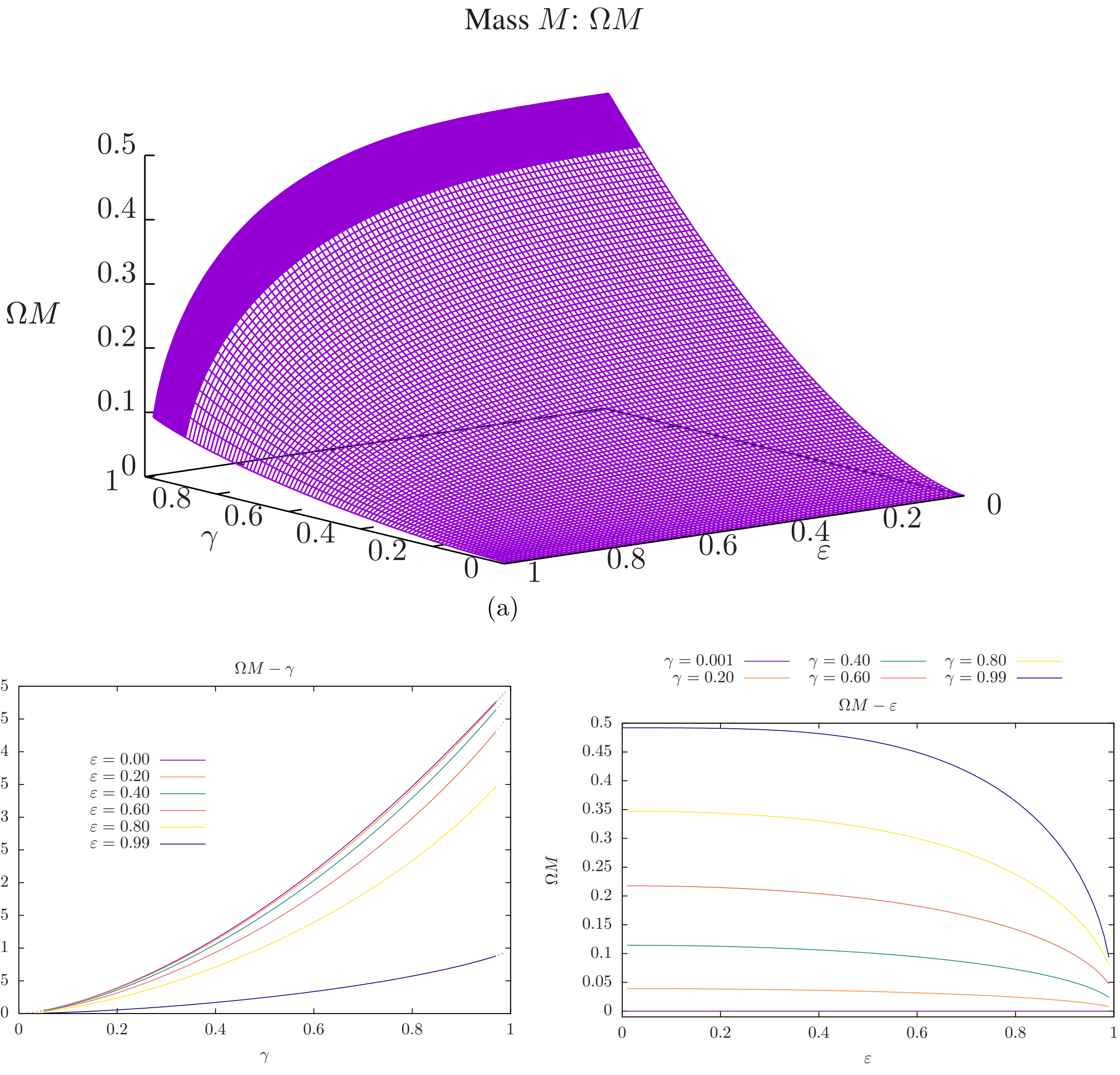

(a)

(b)

(c)

Figure 5.5: Mass M normalised by Ω. (a) ΩM in the complete parameter space (γ, ε). (b) ΩM - γ with different fixed ε's. The dotted lines imply the Newtonian and the ultra-relativistic limits. (c) ΩM - ε with different fixed γ's.

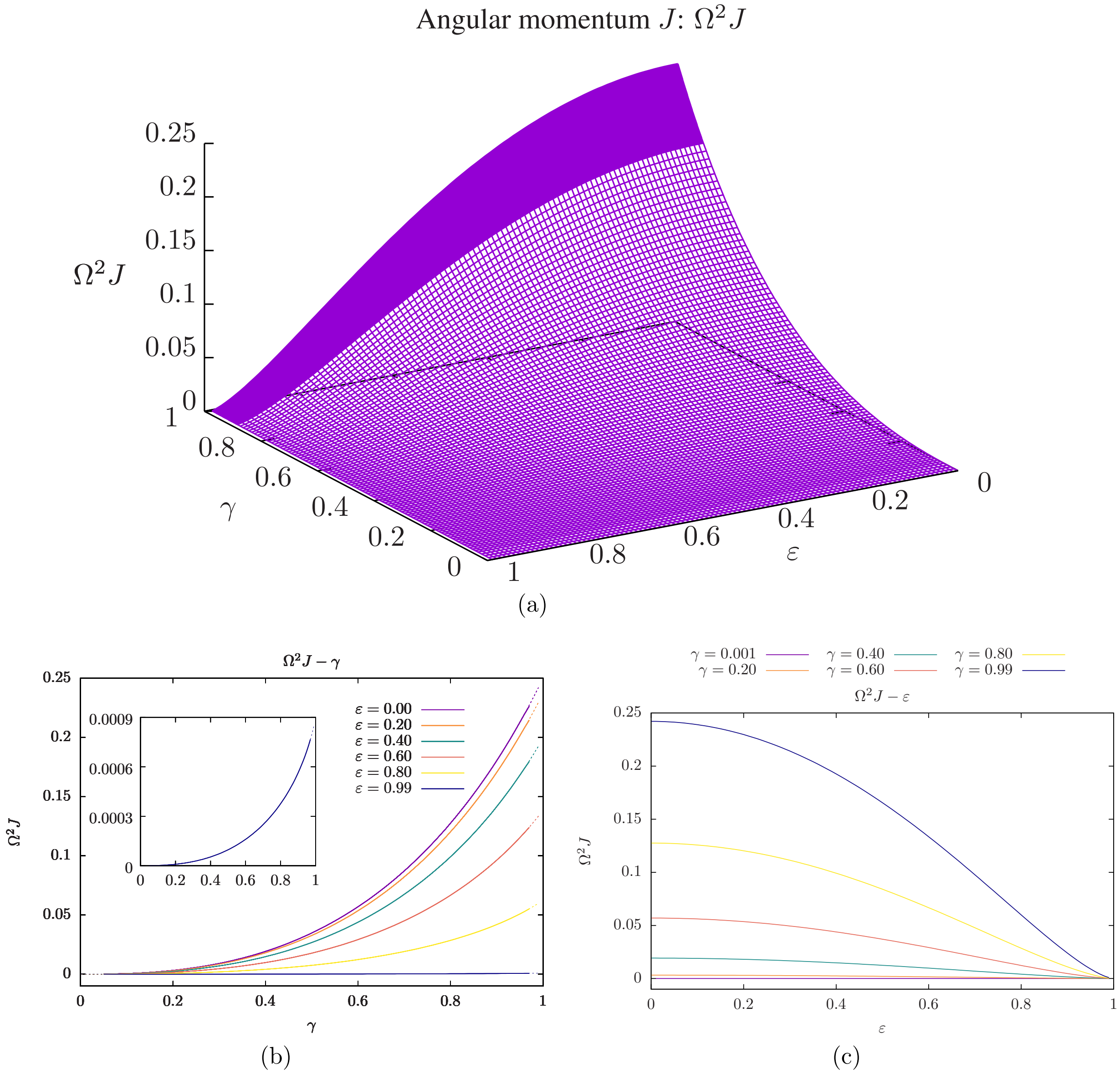

(a)

(b)

(c)

Figure 5.6: Angular momentum J normalised by Ω^2. (a) $\Omega^2 J$ in the complete parameter space (γ, ε). (b) $\Omega^2 J$ - γ with different fixed ε's. The dotted lines imply the Newtonian and the ultra-relativistic limits. The subplot again highlights the $\Omega^2 J$ where $\varepsilon = 0.99$, since the curve is marginal compared to the other curves and its values have been subdued in the main plot. (c) $\Omega^2 J$ - ε with different fixed γ's.

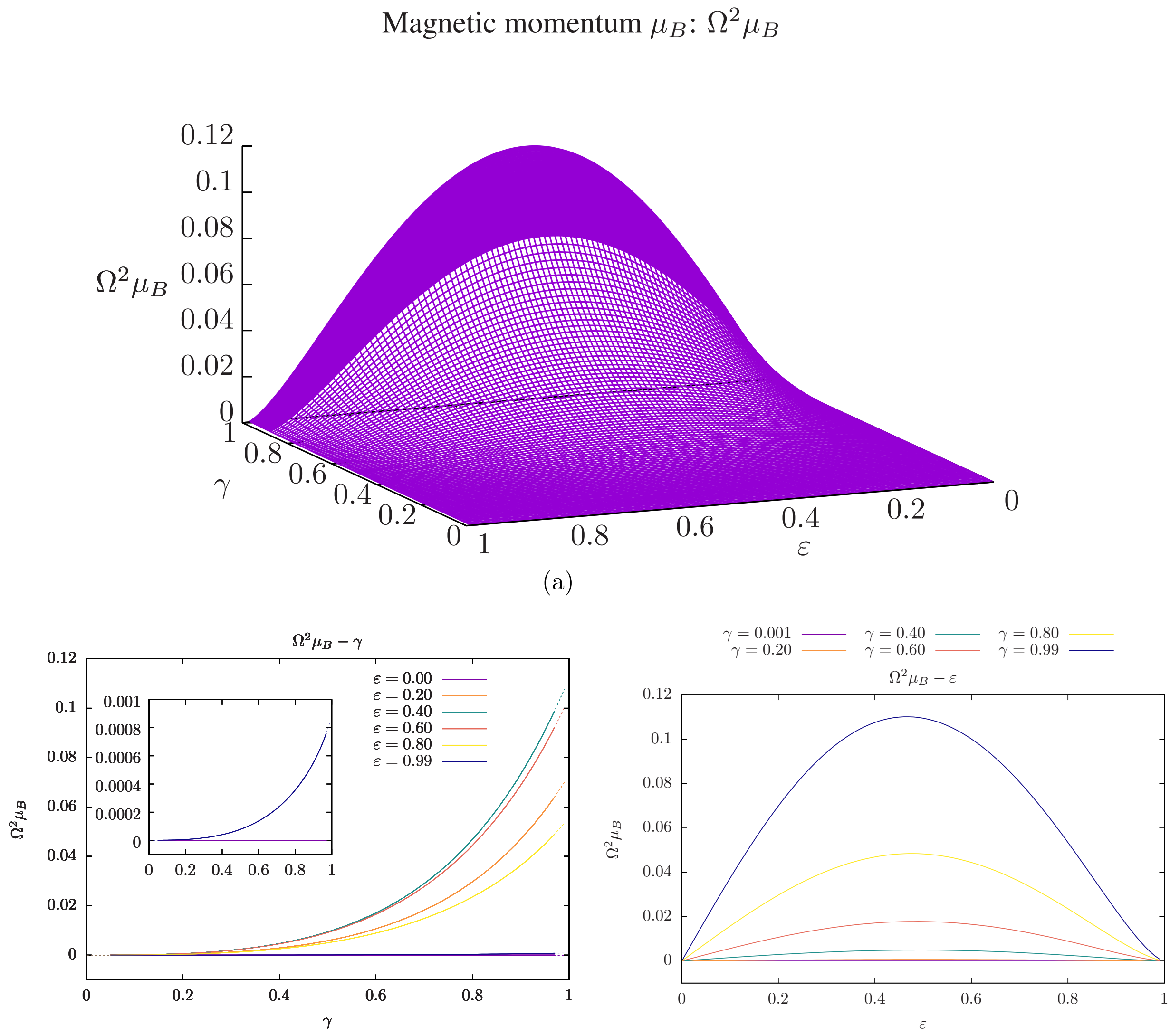

(a)

(b)

(c)

Figure 5.7: Magnetic momentum μ_B normalised by Ω^2. (a) $\Omega^2\mu_B$ in the complete parameter space $\Omega^2\mu_B$. (b) $\Omega^2\mu_B$ - γ with different fixed ε's. The dotted lines imply the Newtonian and the ultra-relativistic limits. The subplot again highlights the $\Omega^2\mu_B$ where $\varepsilon = 0.0$ and $\varepsilon = 0.99$, since their curves are marginal compared to the other curves and their values have been subdued in the main plot.(c) $\Omega^2\mu_B$ - ε with different fixed γ's.

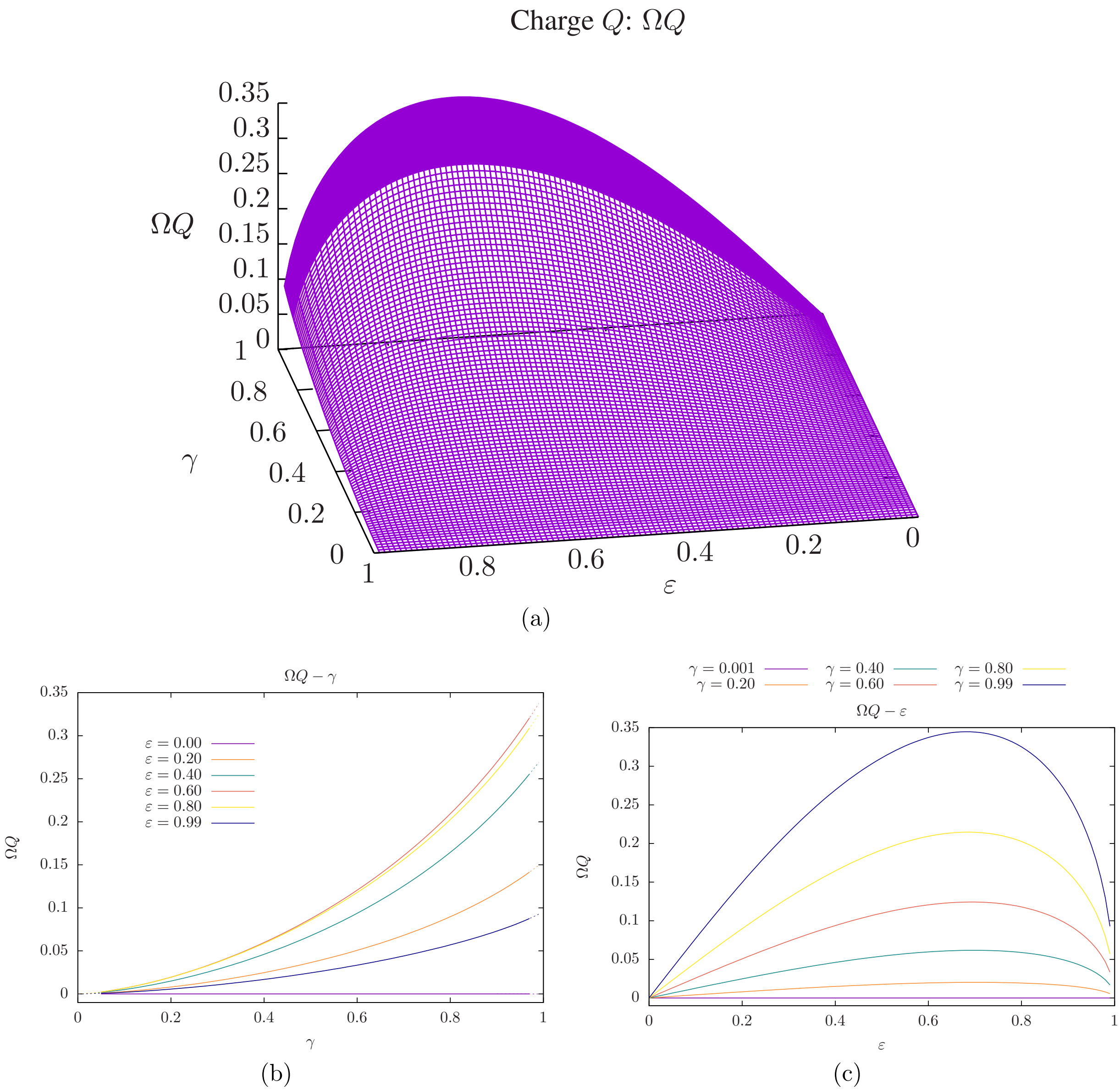

(a)

(b)

(c)

Figure 5.8: Charge Q normalised by Ω. (a) ΩQ in the complete parameter space (γ, ε). (b) ΩQ - γ with different fixed ε's. The dotted lines imply the Newtonian and the ultra-relativistic limits. (c) ΩQ - ε with different fixed γ's.

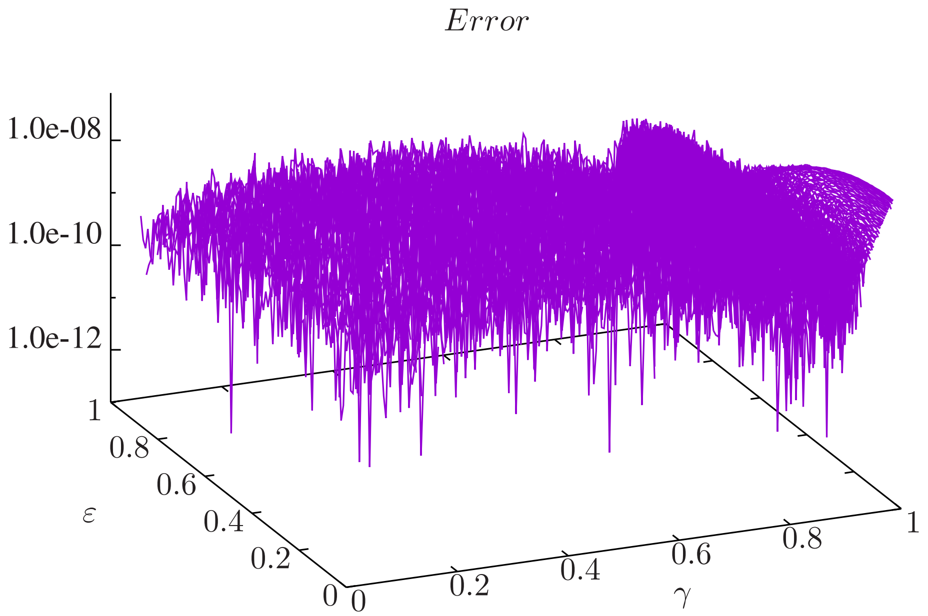

Figure 5.9: Error in the logarithm scale for the accuracy test of physical properties using (4.14) in (γ, ε) parameter space with $0 \leq \varepsilon \leq 1$ and $0 \leq \gamma \leq 0.99$.

in. The analytical mesh-refinement method discussed in 3.2.4 was used to rectify the problem, as shown in the inset of figure 5.10, the dashed line representing the numerical error after applying the analytical mesh-refinement, which is again able to maintain the accuracy to 10^{-8}.

5.5 Gyromagnetic Factor g

In the previous section, it was shown that the numerical error that describes the accuracy of the physical properties M, J, μ_B, Q and the angular velocity Ω has a high precision of up to 10^{-8}. A further inspection was carried out for the gyromagnetic factor g of the model of a rotating disc of charged dust, whose classical value is $g = 1$ and whose ultra-relativistic limit is presumed to be $g = 2$, like some of the relativistic or quantum systems mentioned in section 4.1.4. Although it can be acquired by the post-Newtonian expansion, the spectral method provides a higher precision in the relativistic region, as will be shown in this section.

The result with the post-Newtonian procedure is first demonstrated, then the result with the numerical method, after which the performance of the two are compared. It is also shown how the gyromagnetic factor is distributed in the whole parameter space, and the respective influence from γ and ε are discussed.

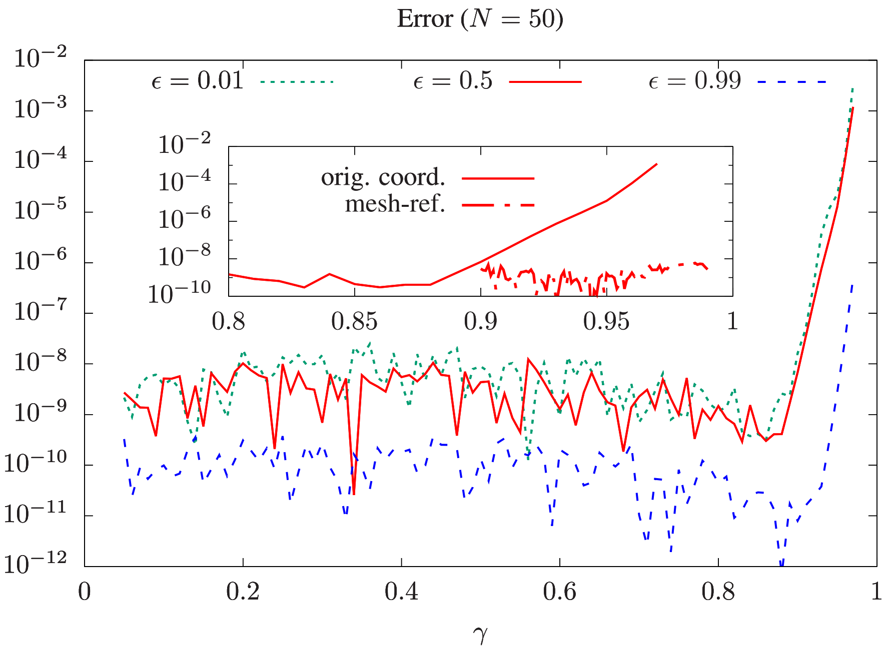

Figure 5.10: Error for the accuracy test of physical properties using (4.14) with respect to γ, with $\varepsilon = 0.01$, 0.5 and 0.99 respectively. Additionally, the subplot shows the effect and the accuracy enhancement using the analytical mesh-refinement from $\gamma \approx 0.90$, which assures the higer numerical accuracy in the ultra-relativistic limit $\gamma \to 1$.

5.5.1 Post-Newtonian expansion for the gyromagnetic factor

The gyromagnetic factor (g-factor) is defined as

$$g := 2\frac{M}{Q}\frac{\mu_B}{J} = \frac{2}{\psi}\frac{\mu_B}{J}.$$

Using the post-Newtonian expansion of $J(\gamma, \psi)$, $\mu_B(\gamma, \psi)$ in [15][1] and the expansion of $E_B^{(rel)}$ in [14], plus the relation

$$\psi = \frac{Q}{M} = \varepsilon \left(1 - E_B^{(rel)}\right)^{-1}, \qquad E_B^{(rel)} : \text{Relative binding energy},$$

which transforms $J(\gamma, \psi)$, $\mu_B(\gamma, \psi)$ into $J(\gamma, \varepsilon)$, $\mu_B(\gamma, \varepsilon)$, the following approximation is achieved

$$g(\gamma, \varepsilon) = 1 + \sum_{k=0}^{\infty} \sum_{\ell=0}^{k} c_{k,\ell}\, \epsilon^{2\ell} \gamma^k,$$

---

[1] A misprint in eq.(A.23) in [15]: The coefficient term of Ψ^4 should read "$\left(\frac{9}{22400} + \frac{4}{9\pi^2}\right)$" instead of "$\left(\frac{9}{86400} + \frac{4}{9\pi^2}\right)$"

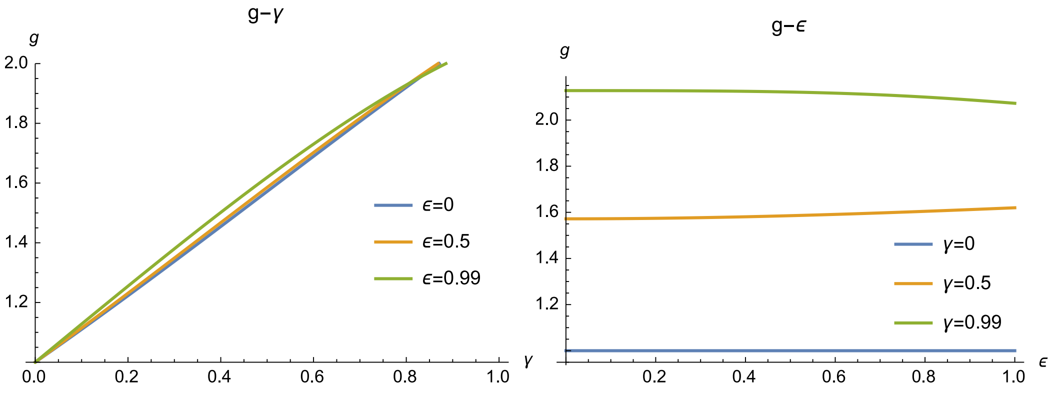

(a) (b)

Figure 5.11: The post-Newtonian results of the gyromagnetic factor up to the forth order. (a): gyromagnetic factor versus γ. (b): gyromagnetic factor verus ε.

with the coefficients $c_{k,\ell}$ up to the forth order as

$$c_{1,0} = \frac{38}{35}, \quad c_{1,1} = \frac{1}{5}, \quad c_{2,0} = -\frac{1181}{1575} + \frac{80}{9\pi^2}, \quad c_{2,1} = \frac{20789}{66150} - \frac{40}{9\pi^2}, \quad c_{2,2} = -\frac{19}{675},$$

$$c_{3,0} = -\frac{19277}{808500} - \frac{592}{3465\pi^2}, \quad c_{3,1} = \frac{8891257}{16632000} - \frac{2936}{495\pi^2},$$

$$c_{3,2} = -\frac{539977931}{1629936000} + \frac{2152}{693\pi^2}, \quad c_{3,3} = \frac{260177}{12936000} - \frac{8}{45\pi^2}$$

$$c_{4,0} = -\frac{7978729279}{22702680000} + \frac{22923716}{868725\pi^2} - \frac{56320}{243\pi^4}, \quad c_{4,1} = \frac{369388881091199}{488198430720000} - \frac{41255480963}{1021620600\pi^2} + \frac{26240}{81\pi^4}$$

$$c_{4,2} = -\frac{579496867964537}{976396861440000} + \frac{36234236351}{2043241200\pi^2} - \frac{29120}{243\pi^4},$$

$$c_{4,3} = \frac{1320650497820209}{10252167045120000} - \frac{3807395827}{2043241200\pi^2} + \frac{640}{81\pi^4} \quad c_{4,4} = -\frac{5474341391}{715134420000} + \frac{104}{1215\pi^2}.$$

Figure 5.11 displays the graphical expression of the post-Newtonian result up to the forth order. Higher order of the expansion will be shown and compared in further figures. Using the post-Newtonian method, the classical limit $\gamma \ll 1$ yields the outcome $g = 1$. It is however seen that at the ultra-relativistic limit $\gamma \to 1$, the convergence of the result is yet to be improved, since the post-Newtonian calculation is accurate for smaller γ's and ε's. The numerical results provide a more accurate description for larger γ's and ε's, as will be seen in the following section.

5.5.2 Numerical Calculations for the gyromagnetic factor

The result of the spectral method is shown in figure 5.12. Plot (a) shows the gyromagnetic factor in the whole parameter space (γ, ε), where plots (b) and (c) illustrate the individual influences of γ and ε. The result confirms that the gyromagnetic factor of the rotating disc of charged dust performs a smooth monotonic interpolation between $g = 1$ of the Newtonian limit and the $g = 2$ of the ultra-relativistic limit. Note that at $\gamma \to 1$, the g-factor approaches 2 with its slope tending to 0, irrelevant of the value of ε, as shown in plot (b).

$$\lim_{\gamma \to 1} g_{,\gamma} = 0.$$

The handling of the ultra-relativistic limit is fairly sensitive and has to be treated with care and high precision, therefore the use of an even higher grid and an additional technique such as mesh-refinement and eventually the analytical solution can provide a more definite conclusion regarding this proposition.

At the same time, it is seen that the constant specific charge ε has little influence on the g-factor compared to the relativity parameter γ as seen in plots (b) and (c), the non-charged case $\varepsilon = 0.00$ and the near electrically counterpoised case $\varepsilon = 0.99$ do not deviate drastically from each other.

5.5.3 Support and Comparison

As mentioned in the previous section 5.5.2, the constant specific charge ε does not contribute drastically to the change of the g-factor. However, one interesting fact to notify is that the g-factor has a non-0 finite limit at both the uncharged case $\varepsilon \to 0$ and electrical counterpoised case $\varepsilon \to 1$, even though as mentioned at the end of section 5.3, the physical proprieties have $Q = \mu_B = 0$ at $\varepsilon \to 0$ and $J = \mu_B = 0$ at $\varepsilon \to 1$. The explanation can be best supported by the post-Newtonian expressions, as shown in [14, 15] with the expansion of the angular momentum, magnetic moment and the charge-mass ratio given as $J \sim \sqrt{1-\varepsilon^2}$, $\mu_B \sim \varepsilon\sqrt{1-\varepsilon^2}$ and $\psi = Q/M \sim \varepsilon$, the ratio $\mu_B/(\psi J)$ of the gyromagnetic factor is thus finite in both limits.

As shown in figure 5.13, it is seen the post-Newtonian expansion offers a precise reproduction of the g-factor at the lower γ, which provides the support of $g \to 1$ at the Newtonian limit $\gamma \ll 1$. However, the post-Newtonian method is not so accurate in predicting the g-factor in the higher γ, as seen in figure 5.13, where the numerical result provides a more accurate convergence of $g \to 2$ at $\gamma \to 1$. In [15], two methods were used for extrapolating larger γ, one is the post-Newtonian expansion and the other is the post-Newtonian expansion plus the Padé extrapolation. The two techniques are compared with the numerical result and the detailed comparison displayed in figure 5.14, and as discussed previously, the numerical method again shows its significant advantage, especially at higher γ. As seen in the figure, it shows that the post-Newtonian method is accurate until $\gamma \approx 0.26$ and the refined post-Newtonian method with Padé extrapolation delivers accuracy until $\gamma \approx 0.5$ onwards, whilst the numerical result delivers a higher precision of the order of 10^{-3} at the ultra-relativistic limit.

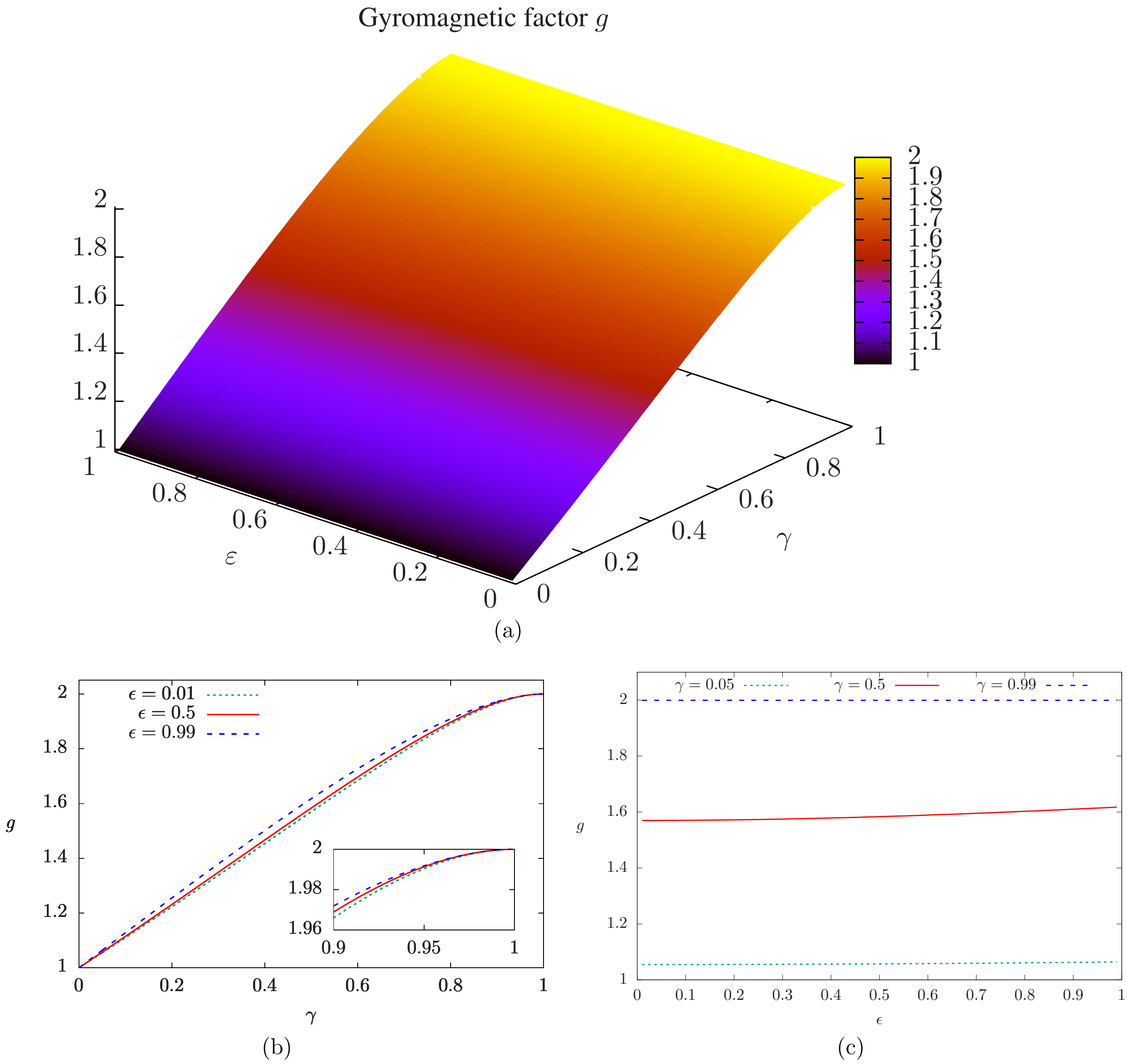

(a)

(b)

(c)

Figure 5.12

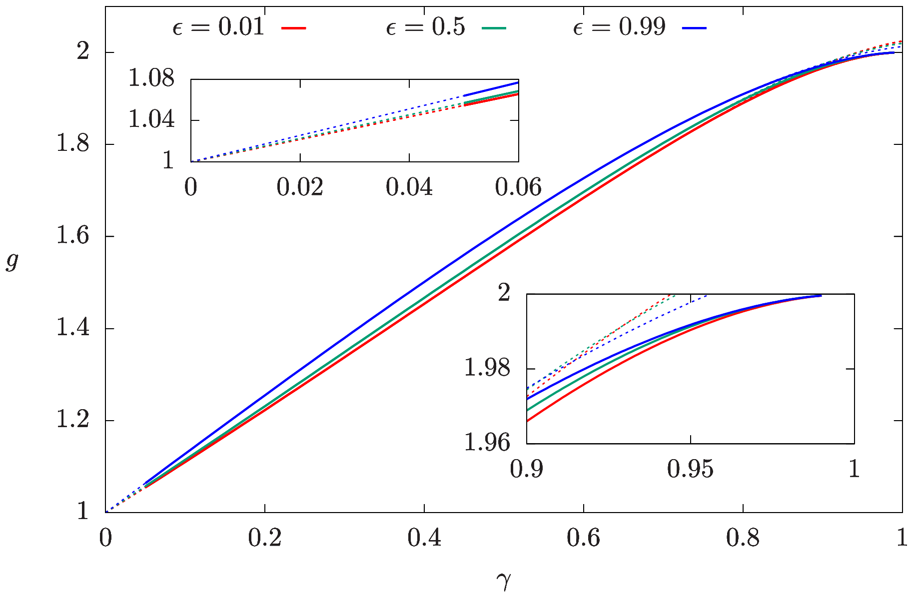

Figure 5.13: Comparison of the numerical and post-Newtonian result. The upper left window shows the detail of the g-factor at the near Newtonian limit $\gamma \to 0$, whereas the lower right inset highlights the result near the ultra-relativistic limit $\gamma \to 1$.

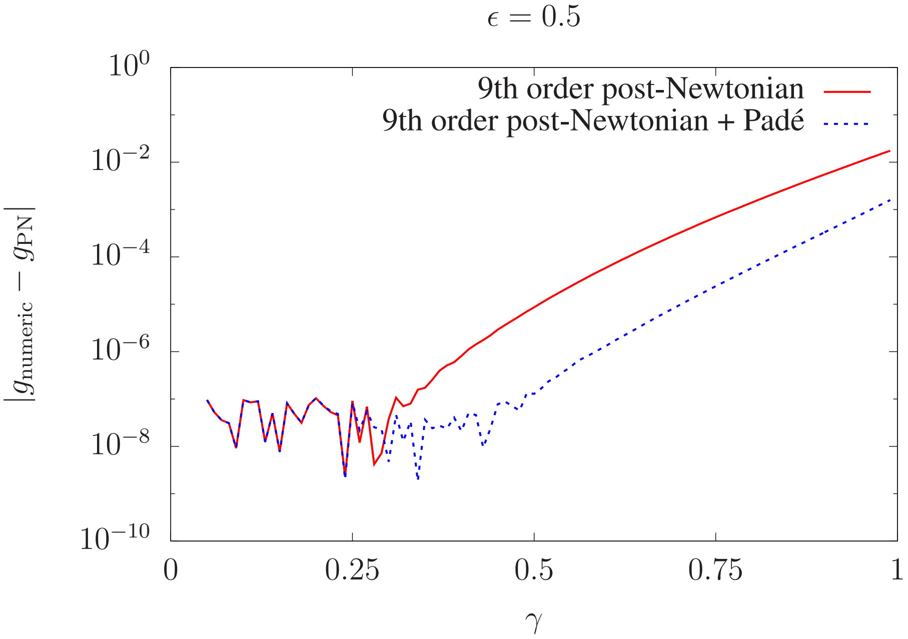

Figure 5.14: Comparing the error between the numerical and the post-Newtonian/Padé approximation.

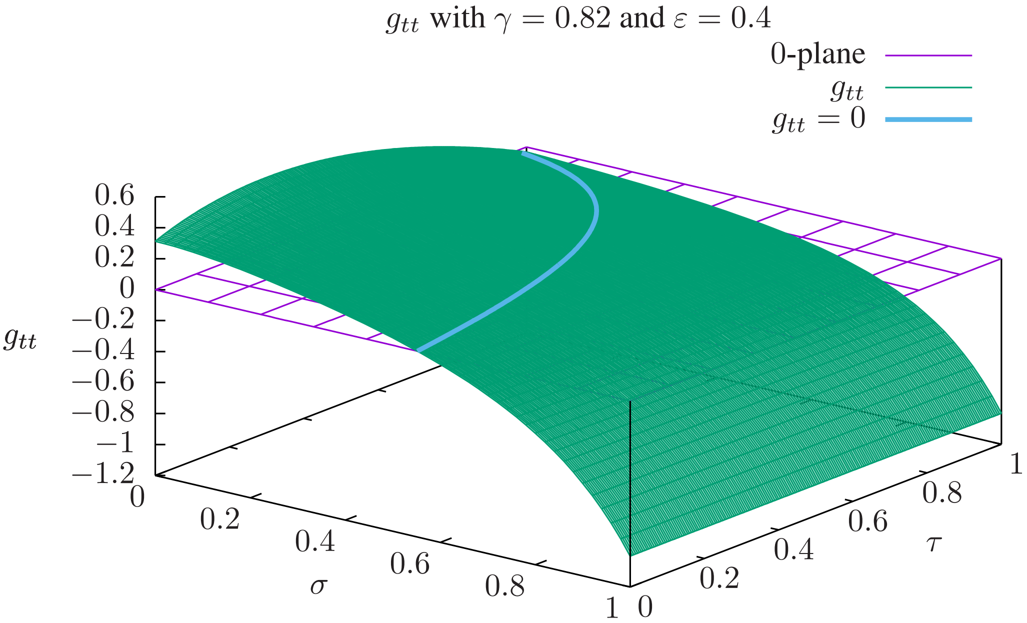

Figure 5.15: Pictorial result of the bisection method. Green denotes the g_{tt} surface, purple is the 0-plane, and blue is the cross section of $g_{tt} = 0$ where the boundary of the ergosphere occurs.

5.6 Ergosphere

As discussed in section 4.2, the bisection method is used to find the cross section of all the areas of σ and τ of the whole parameter space (γ, ε). In the case presented here, both σ and τ run from 0 to 1. Figure 5.15 shows an example of the pictorial result of finding the surface: After gaining the raw data of from the field equation, g_{tt} is obtained from

$$g_{tt} = -\tilde{\nu}^2 + \frac{e^{2\nu^c}(1-\tau)}{\cos^2\left(\frac{\pi\sigma}{2}\right)} \frac{\tilde{\omega}^2}{\tilde{\nu}^2}.$$

For every fixed τ, a σ_{ergo} is found at $g_{tt} = 0$ using the bisection method. Scanning through the whole area, the whole picture of the $(\sigma_{ergo}, \tau_{ergo})$ is found, where $g_{tt} = 0$ is located. The combined data is the surface of the ergosphere.

In [16], the properties of the ergosphere for the non-charged disc was discussed, including the appearance of the ergosphere with respect to the relativistic parameter γ. Here the discussion is expanded by introducing the electromagnetic factor, ranging from the non-charged case $\varepsilon = 0$ to the electrical counterpoised case $\varepsilon \to 1$.

Figure 5.16 shows the configuration of ergospheres under different scales of relativistic and charge intensity from the asymptotic perspective, namely, the system is normalised with $\Omega(\gamma, \varepsilon)$, the radii of the disc ρ_0 therefore differs, depending on angular velocity Ω, as discussed in section 4.1.2. From the figure, one sees that the larger the relativistic effect, the larger charge intensity required in order to trigger the formation of the ergosphere. Also notable is that, under the same relativistic influence, the larger the charge, the smaller the ergosphere appears to be.

Figure 5.17 shows a more direct comparison of the size of ergospheres for different γ's and ε's. The system is normalised with ρ_0 so that the disc radius consistently remains $\rho_0 = 1$. In this perspective, the observer is at the near-source region. The tendency of the decreasing of the ergosphere surface with increasing constant charge density ε is also observed. Further, the larger the relativistic parameter γ, the larger the ε value required for the appearance of the ergospheres.

In figure 5.18, instead of simply showing individuals, the whole parameter space (γ, ε) is covered and a precise overview of when the ergospheres start appearing provided. One sees that the transition can be formed into a smooth curve starting from $\gamma \approx 0.585$ all the way to $\gamma \to 1$, which indicates a simple relation that could potentially be summarised analytically. In the following a numerical fitting to the plot is provided: With the curve resembling the shape of a quarter of an oval, the curve is fitted into the oval equation

$$\frac{(\gamma-1)^2}{(1-0.585)^2} + \frac{(\varepsilon-0)^2}{1^2} = 1,$$

yielding

$$\varepsilon \approx 0.0120482\sqrt{-40000\gamma^2 + 80000\gamma - 33111}, \tag{5.2}$$

which provides a reasonable fitting, as shown in figure 5.19. The precise data are listed in the table presented in appendix D.

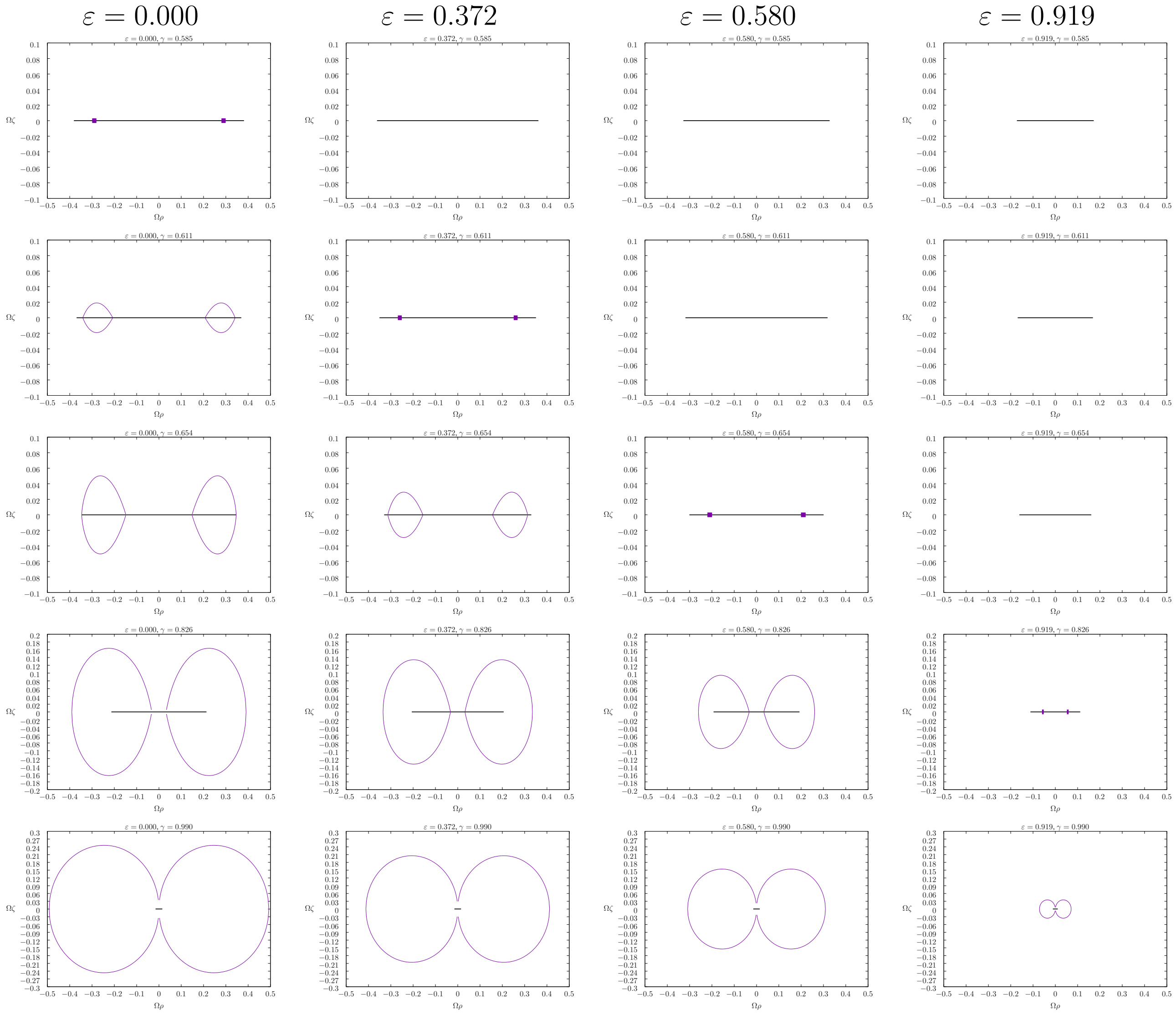

Figure 5.16: Examples of the ergosphere under different γ and ε. Shown in the Weyl coordinates (ρ, ζ) and normalised by Ω, from left to right is $\varepsilon = 0.000$, 0.372, 0.580, 0.919 and from top to bottom is $\gamma = 0.585$, 0.611, 0.654, 0.826, 0.990. The dots in the plots are where the ergosphere first appears: For $\varepsilon = 0.000$, $\gamma = 0.585$; for $\varepsilon = 0.372$, $\gamma = 0.611$; for $\varepsilon = 0.580$, $\gamma = 0.654$; for $\varepsilon = 0.919$, $\gamma = 0.826$. The solid black lines denote the radii of the disc under different Ω influence at far field.

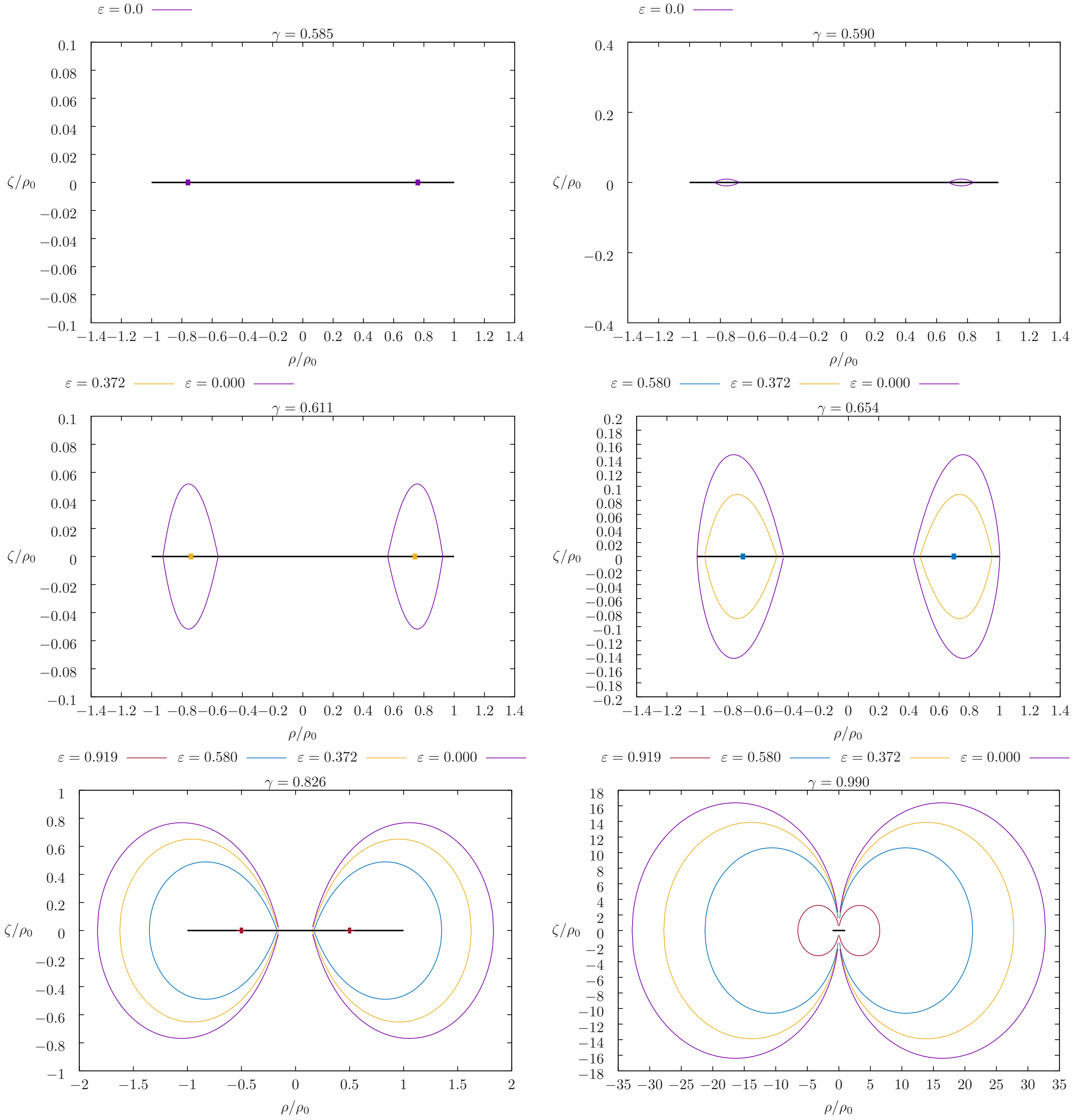

Figure 5.17: The size of the ergosphere compared under different (γ, ε). Shown in Weyl coordinates (ρ, ζ) and normalised by ρ_0. The disc is shown with the solid black line, with its radius ρ_0 is normalised to be 1. For all six subplots, the same colour represents the same ε: with $\varepsilon = 0.000$ in purple, $\varepsilon = 0.372$ in yellow, $\varepsilon = 0.580$ in blue and $\varepsilon = 0.919$ in red.

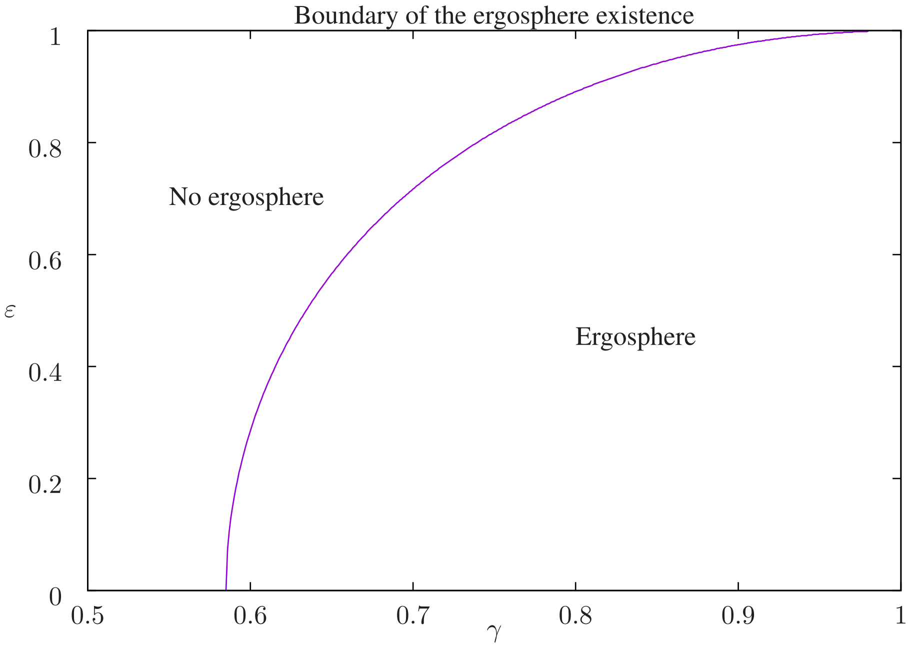

Figure 5.18: Boundary where the ergospheres start appearing under different γs and εs. For the non-charged($\varepsilon = 0$) case, as supported in [16], the ergosphere starts appearing at $\gamma \approx 0.585$.

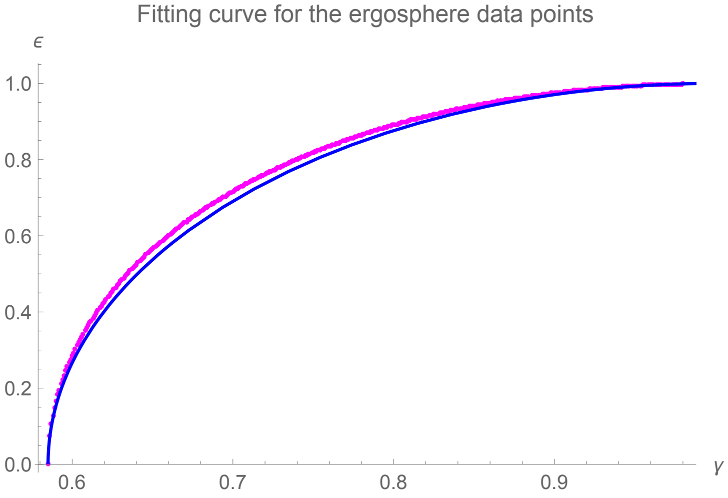

Figure 5.19: Fitting the ergosphere data points. Magenta denotes the actual ergosphere data points, whereas blue denotes the fitting curve (5.2) for the data points.

Chapter 6

Conclusion and Outlook

In this work, the pseudo-spectral method for solving the Einstein-Maxwell field equations for the rotating disc of charged dust was used. The field equations and the boundary conditions for the model structure were derived, then the numerical method to solve the equations system was applied. After obtaining the raw fields, they were converted into more concrete physical properties, which provided a more intuitive aspect towards the system. Furthermore, the accuracy of the numerical method was discussed and compared with other methods including the post-Newtonian expansion method. Finally, the gyromagnetic factor and the ergosphere of the system were evaluated and some interesting properties were found or justified.

The field equations were derived by gradually inserting the different characteristics into the Einstein-Maxwell equations: The Lewis-Papapetrou-Weyl metric introduced the stationarity and axial-symmetry into the system; the energy-momentum tensor defined the rotation and the fluid and the charge characteristics; the disc feature was obtained by applying the pill-box integration on the charged fluid field equation; and setting the pressure free configuration yielded the dust character. The outcome was the field equation system of the disc of charged dust. Even though having a more complex configuration, it can be separated explicitly into the fluid section and the charged section, where the fluid part is the non-charged field equation. Using the tetrad basis, the equations were written in a more compact form, which was beneficial to the numerical calculations.

For the numerical calculation, the pseudo-spectral method was used. The equation system was adjusted, so that it is applicable to the numerical method by transforming the coordinate system to the spectral compactificated coordinate and by rescaling the potentials. Despite the transformations, the field equations still preserved the form, in which the charged and non-charged parts are explicitly separated. The code was originally diverged at the ultra-relativistic region due to the high gradient of the potential curve. Increasing the grid points is a possible way of solving the problem, yet the calculation time will increase drastically, on the other hand, applying the analytical mesh-refinement method, ensured the convergence up to a higher γ, and still provides a calculation time that is similar to that of the original code.

The raw data fields $\tilde{\nu}$, $\tilde{\omega}$, A_φ and $\tilde{A}_t$ were the direct outcome of the solution. Although the data needed to be further processed into more intuitive properties such as the physical quantities, their distribution provided a control measure of the correctness of the calculation. Firstly, the result was confirmed by reducing the fields to $\varepsilon = 0$, which matched the outcome of the non-charged case. Furthermore, the result reflected and agreed with the boundary conditions.

The physical quantities mass M, angular momentum J, magnetic dipole moment μ_B and charge Q were derived from the raw data. The intrinsic properties of the physical quantities stayed the same, irrelevant of the normalisation, since the metric remained invariant under parametrisation of the potential and the coordinate. However, it made a difference depending from which perspective the physical quantities are observed. Normalising through the angular velocity Ω provided an asymptotic perspective, whereas normalising through the radius of the disc ρ_0 offers a near-source point of view. The physical properties diverged when presented using the ρ_0 normalisation but stayed finite using Ω normalisation, since they are derived from the asymptotic behaviour of the raw field, and thus made more sense to observe from the far-field. The result also coincided with the non-charged case, which has $\Omega M = 0.5$ and $\Omega^2 J = 0.25$ in the ultra-relativistic case.

The physical proprieties formed an parameter relation, which could be rewritten into an error equation, and could thus be used to inspect the correctness of the result. The error was precise up to a high order of 10^{-8}. Since the error equation was formed by a combination of physical properties, and the physical properties are in turn derived by the raw data, and the raw data were obtained by the equation system, the high precision of the result reassured the accuracy of the calculation, all the way back to the formation of the field equation system.

For the gyromagnetic factor, it could be shown that, for the system of the rotating disc of charged dust, $g = 1$ was observed for the classical limit $\gamma \ll 1$, as was the case for the post-Newtonian expansion. Furthermore, $g = 2$ could be reached with high precision at the ultra-relativistic limit $\gamma \to 1$ using the numerical approach. Since there are some relativistic and quantum systems that also have this limit, a link between these two regimes could be worthy of further investigation. In the parameter space, the value of the g-factor is connected smoothly and monotonically though the relativistic parameter γ, and has a milder connection with the constant charge ε. As with the comparison with the post-Newtonian method, it could be shown that the post-Newtonian method was accurate until $\gamma \approx 0.26$, and the refined post-Newtonian method with Padé extrapolation delivered the accuracy until $\gamma \approx 0.5$, onwards which the numerical result provided a higher precision of the order of 10^{-3} at the ultra-relativistic limit $\gamma \to 1$.

Part of the result of the physical properties, error and gyromagnetic factor are published in [17].

As for the ergosphere, the ergosphere surface was extracted using the bisection method where $g_{tt} = 0$. The ergosphere in both asymptotic and near-source perspectives in the entire parameter space was shown. Both perspectives showed that the size of the ergosphere decreases with increasing relativistic parameter γ. The larger the relativistic effect is, the higher the charge effect is required in order to trigger the appearance of the ergosphere. The boundary of the beginning of the ergosphere appearance with respect to the relativistic and the electromagnetic influence (γ, ε) could be neatly summarised, as shown in figure 5.18, and which fitted well to the oval equation, implying a possible analytical investigation and analysis.

In this work, though focused on the rigidly rotating model $\Omega = constant$, the calculation does not have to be limited to this aspect. With the numerical approach used for this work, one can also discuss the differential rotating case $\Omega = \Omega(\rho)$ using the same field equation and boundary condition settings. It will be interesting to see how the physical properties changes with the rotation of the disc, since the model will be even more similar to the astrophysical spiral disc galaxies or celestial bodies. Answering questions such as whether the gyromagnetic factor still remains between 1 and 2, as observed with several of the astrophysical and quantum systems, or how the ergosphere evolves and whether it still yields a nice gradual appearance in the parameter space that can be summarised into a compact and elegant fitting, remain interesting and achievable for the future.

Appendices

Appendix A

Detailed Calculation to the Field Equations

A.1 Overview

A.1.1 Einstein Equation

The Einstein equation
$$R_{ik} - \frac{1}{2} R g_{ik} = 8\pi T_{ik}$$
contains Ricci tensors R_{ik}, Ricci scalars R and energy-momentum tensors T_{ik}, which are obtained as follows

- Ricci tensors: $R_{ik} = R^a_{iak}$,

  with Riemann tensors
  $$R^a_{ibk} = \partial_b \Gamma^a_{ik} - \partial_k \Gamma^a_{ib} + \Gamma^c_{ik}\Gamma^a_{cb} - \Gamma^c_{ib}\Gamma^a_{ck},$$

  and Christoffel symbols
  $$\Gamma^a_{bc} = \frac{1}{2} g^{ad} \left(\partial_c g_{bd} + \partial_b g_{cd} - \partial_d g_{bc} \right).$$

- Ricci scalar: $R = g^{ik} R_{ik}$
- Energy-momentum tensors: $T_{ik} = {T_{ik}}^{(fluid)} + {T_{ik}}^{(em)}$

  with the fluid part
  $${T_{ik}}^{(fluid)} = (\mu + p) u_i u_k + p g_{ik},$$

  μ being the mass-energy density and p the pressure. and the electromagnetic part
  $${T_{ik}}^{(em)} = \frac{1}{4\pi} \left(F_{ij} {F_k}^j - \frac{1}{4\pi} F^{mn} F_{mn} g_{ik} \right),$$

F_{ik} being the electromagnetic tensor

$$F_{ik} = A_{k,i} - A_{i,k}, \tag{A.1}$$

A_k being the four-potential(vector potential).

A.1.2 Maxwell Equation

The Maxwell equation

$$F^{ik}{}_{;k} = 4\pi \jmath^i,$$

constains the covariant derivatives of the electromagnetic tensor $F^{ik}{}_{;k}$ and the convective four-current density $\jmath^i$, which are as follows

- Covariant derivatives of the electromagnetic tensor $F^{ik}{}_{;k}$

  $$F^{ik}{}_{;a} = F^{ik}{}_{,a} + \Gamma^i_{ab} F^{bk} + \Gamma^k_{ba} F^{ib}$$

- Convective four-current density $\jmath^i = \varepsilon \mu u^i$

  with the mass density μ, fluid four-velocity $u^i = e^{-V} \left(\xi^i + \Omega \eta^i\right)^1$ and constant specific charge $\varepsilon \in [-1, 1]$.

A.1.3 Different Reference of Frame

The Lewis-Papapetrou-Weyl metric describes the spacetime of a stationarily rotating and axisymmetric perfect fluid body

$$ds^2 = e^{2\alpha}(d\rho^2 + d\zeta^2) + \rho^2 e^{-2\nu}(d\varphi - \omega dt)^2 - e^{2\nu} dt^2,$$

Through the Tetrad transformation in [2]

$$\lambda_{(\rho)}{}^{\hat{i}} = e^{-\alpha} \delta^{\hat{i}}_{(\rho)}, \quad \lambda_{(\zeta)}{}^{\hat{i}} = e^{-\alpha} \delta^{\hat{i}}_{(\zeta)}, \quad \lambda_{(\varphi)}{}^{\hat{i}} = \frac{e^{\nu}}{\rho} \delta^{\hat{i}}_{(\varphi)}, \quad \lambda_{(t)}{}^{\hat{i}} = e^{-\nu} \delta^{\hat{i}}_{(t)} + \omega e^{-\nu} \delta^{\hat{i}}_{(\varphi)},$$

one transform the Lewis-Papapetrou-Weyl metric into the orthonormal tetrad basis

$$ds^2 = dx_1^2 + dx_2^2 + dx_3^2 - dt^2.$$

The field equations obtained directly through the metric and obtained via the tetrad basis only differ from the point of view of the observers. While the field equations obtain directly through the metric is being regarded from the point of view of the distant observer, the field equations obtained via the tetrad basis is being regarded from the point of view of the local Lorentz observer. Thus the Ricci scalar should be invariant, irrelevant of under which frame of reference we use to obtain the field equations. We thus use it to check the correctness of our calculation after obtaining the Ricci tensors using these two different frame of reference respectively.

---

[1] The Killing vectors $\xi^i = \delta^i_t$ and $\eta^i = \delta^i_\varphi$ denote the stationarity and and axisymmetry respectively.

A.1.4 Mathematica Code

- Setting up the environment:
  - Give number of Dimension:

$$Dim = 4;$$

  - Give the metric g_{ik} :

$$\begin{array}{l}
Do[gd[i,j] = 0, \{i, Dim\}, \{j, Dim\}] \\
gd[1,1] = e\alpha[\rho,\zeta]^2;\ gd[2,2] = e\alpha[\rho,\zeta]^2;\ gd[3,3] = \frac{\rho^2}{e\nu[\rho,\zeta]^2};\ gd[3,4] = -\frac{\rho^2\omega[\rho,\zeta]}{e\nu[\rho,\zeta]^2}; \\
gd[4,3] = -\frac{\rho^2\omega[\rho,\zeta]}{e\nu[\rho,\zeta]^2};\ g[4,4] = -e\nu[\rho,\zeta]^2 + \frac{\rho^2\omega[\rho,\zeta]}{e\nu[\rho,\zeta]^2};
\end{array}$$

  - Define the coordinate:

$$x[1] = \rho;\ x[2] = \zeta;\ x[3] = \varphi;\ x[4] = t;$$

  - Killing vectors: η(axis symmetry), ξ(stationary)

$$\begin{array}{l}
\xi[1] = 0;\ \xi[2] = 0;\ \xi[3] = 0; \xi[4] = 1; \\
\eta[1] = 0;\ \eta[2] = 0;\ \eta[3] = 1; \eta[4] = 0;
\end{array}$$

  - Four-velocity $u^i = e^{-V}(\xi^i + \Omega\eta^i)$:

$$\begin{array}{l}
v[\rho,\zeta] = \frac{\rho(\Omega-\omega[\rho,\zeta])}{e\nu[\rho,\zeta]^2}; \\
uu[1] = \frac{(\xi[1]+\eta[1])}{e\nu[\rho,\zeta]\sqrt{1-v[\rho,\zeta]^2}};\ uu[2] = \frac{(\xi[2]+\eta[2])}{e\nu[\rho,\zeta]\sqrt{1-v[\rho,\zeta]^2}};\ uu[3] = \frac{(\xi[3]+\eta[3])}{e\nu[\rho,\zeta]\sqrt{1-v[\rho,\zeta]^2}};\ uu[4] = \frac{(\xi[4]+\eta[4])}{e\nu[\rho,\zeta]\sqrt{1-v[\rho,\zeta]^2}};
\end{array}$$

  - Four-potential A_i:

$$A[1] = A\rho[\rho,\zeta];\ A[2] = A\zeta[\rho,\zeta];\ A[3] = A\varphi[\rho,\zeta];\ A[4] = At[\rho,\zeta];$$

- Calculation:
  - Inverse metric g^{ik}:

$$\begin{array}{l}
gtemp = FullSimplify[Inverse[Array[gd, \{Dim, Dim\}]]]; \\
Do[gu[i,j] = 0, \{i, Dim\}, \{j, Dim\}] \\
Do[gu[i,j] = Part[gtemp, i, j], \{i, Dim\}, \{j, Dim\}]
\end{array}$$

  - Christoffel Symbols ${\Gamma^i}_{jk}$:

$$\begin{array}{l}
Do[\Gamma[i,j,k] = 0, \{i, Dim\}, \{j, Dim\}, \{k, Dim\}] \\
Do[Do[\Gamma[i,j,k] + = \frac{1}{2} gu[i,\alpha](D[gd[j,\alpha], x[k]] + D[gd[k,\alpha], x[j]] - D[gd[j,k], x[\alpha]]), \{\alpha, Dim\}] \\
\qquad\qquad , \{i, Dim\}, \{j, Dim\}, \{k, Dim\}]
\end{array}$$

  - Riemann tensor ${R^p}_{qrs}$:

$$\begin{array}{l}
Do[Ruddd[p,q,r,s] = 0, \{p, Dim\}, \{q, Dim\}, \{r, Dim\}, \{s, Dim\}] \\
Do[TermsinRudd[p,q,r,s] = 0, \{p, Dim\}, \{q, Dim\}, \{r, Dim\}, \{s, Dim\}] \\
Do[Do[TermsinRudd[p,q,r,s] + = \Gamma[\beta,q,s]\Gamma[p,\beta,r] - \Gamma[\beta,q,r]\Gamma[p,\beta,s] \\
\qquad\qquad\qquad\qquad , \{\beta, Dim\}], \{p, Dim\}, \{q, Dim\}, \{r, Dim\}, \{s, Dim\}] \\
Do[Ruddd[p,q,r,s] = D[\Gamma[p,q,s], x[r]] - D[\Gamma[p,q,r], x[s]] + TermsinRudd[p,q,r,s] \\
\qquad\qquad , \{p, Dim\}, \{q, Dim\}, \{r, Dim\}, \{s, Dim\}]
\end{array}$$

  - Ricci tensor $R_{uv} = {R^\delta}_{u\delta v}$:

$$\begin{array}{l}
Do[RicciTensor[u,v] = 0, \{u, Dim\}, \{v, Dim\}] \\
Do[Do[RicciTensor[u,v] + = Ruddd[\delta,u,\delta,v], \{\delta, Dim\}], \{u, Dim\}, \{v, Dim\}]
\end{array}$$

  - Ricci scalar $R = g^{xy}R_{xy}$:

$$\begin{array}{l}
RicciScalar = 0; \\
Do[RicciScalar + = gu[x,y]RicciTensor[x,y], \{x, Dim\}, \{y, Dim\}]
\end{array}$$

- Einstein equations $R_{ik}-\frac{1}{2}Rg_{ik}-8\pi T_{ik}$:
  - Energy-momentum tensor $T_{ik}=T^{(fluid)}_{ik}+T^{(em)_{ik}}$:
    - four-velocity(covariant) $u_i=ud[i]$:

$$\boxed{\begin{array}{l} Do[ud[i]=0,\{i,Dim\}] \\ Do[Do[ud[i]+=gd[b,i]uu[b],\{b,Dim\}],\{i,Dim\}] \end{array}}$$

    - $T^{(fluid)}=(\mu+p)u_iu_k+pg_{ik}$:

$$\boxed{\begin{array}{l} Do[TerminT1[i,k]=0,\{i,Dim\},\{k,Dim\}] \\ Do[TerminT1[i,k]+=(\mu[\rho,\zeta]+p)ud[i]ud[k]+pgd[i,k],\{i,Dim\},\{k,Dim\}] \end{array}}$$

    - $T^{(charged-part\ I)}=\frac{F_{ij}F^j_k}{4\pi}=\frac{F_{ij}F_{km}g^{mj}}{4\pi}=\frac{1}{4\pi}\left((A_{j,i}-A_{i,j})\,g^{mj}\,(A_{m,k}-A_{k,m})\right)$:

$$\boxed{\begin{array}{l} Do[TerminT2[i,k]=0,\{i,Dim\},\{k,Dim\}] \\ Do[Do[TerminT2[i,k]+=\frac{1}{4\pi}((D[A[j],x[i]]-D[A[i],x[j]])gu[m,j](D[A[m],x[k]]-D[A[k],x[m]])) \\ \qquad\qquad\qquad\qquad ,\{j,Dim\},\{m,Dim\}],\{i,Dim\},\{k,Dim\}] \end{array}}$$

    - $T^{(charged-part\ II)}=-\frac{F^{mn}F_{mn}g_{ik}}{(4\pi)4}=-\frac{F_{jl}F_{mn}g_{ik}g^{jm}g^{ln}}{(4\pi)4}$:

$$=\frac{1}{4\pi}\left(-\frac{1}{4}g^{jm}g^{ln}\,(A_{l,j}-A_{j,l})\,(A_{n,m}-A_{m,n})\,g_{ik}\right):$$

$$\boxed{\begin{array}{l} Do[TerminT3[i,k]=0,\{i,Dim\},\{k,Dim\}] \\ Do[Do[TerminT3[i,k]+=-(\frac{1}{4\pi}(\frac{1}{4}gu[j,m]gu[l,n](D[A[l],x[j]]-D[A[j],x[l]])(D[A[n],x[m]] \\ \qquad\qquad -D[A[m],x[n]])gd[i,k]),\{j,Dim\},\{l,Dim\},\{m,Dim\},\{n,Dim\}],\{i,Dim\},\{k,Dim\}] \end{array}}$$

    - Energy-momentum tensor T_{ik}:

$$\boxed{\begin{array}{l} Do[T[i,k]=0,\{i,Dim\},\{k,Dim\}] \\ Do[T[i,k]=TerminT1[i,k]+TerminT2[i,k]+TerminT3[i,k],\{i,Dim\},\{k,Dim\}] \end{array}}$$

  - Einstein equations: $Einstein[i,k]=R_{ik}-\frac{1}{2}Rg_{ik}-8\pi T_{ik}$:

$$\boxed{Do[Einstein[i,k]=FullSimplify[RicciTensor[i,k]-\tfrac{1}{2}RicciScalargd[i,k]-8\pi T[i,k]],\{i,Dim\},\{k,Dim\}]}$$

- Maxwell equations: $Maxwell[i]=F^{ik}{}_{;k}-4\pi j^i$:
  - $F^{ij}{}_{;k}=F^{ij}{}_{,k}+F^{dj}\Gamma^i{}_{kd}+F^{id}\Gamma^j{}_{dk}$
    - $F^{ij}_{,k}=CoDerFTerm1[i,j,k]$:

$$\boxed{\begin{array}{l} Do[CoDerFTerm1[i,j,k]=0,\{i,Dim\},\{j,Dim\},\{k,Dim\}] \\ Do[Do[CoDerFTerm1[i,j,k]+=D[gu[m,i]gu[n,j](D[A[n],x[m]]-D[A[m],x[n]]),x[k]] \\ \qquad\qquad\qquad\qquad\qquad ,\{m,Dim\},\{n,Dim\}],\{i,Dim\},\{j,Dim\},\{k,Dim\}] \end{array}}$$

    - $F^{dj}\Gamma^i{}_{kd}+F^{id}\Gamma^j{}_{dk}=CoDerFTerm2[i,j,k]$:

$$\boxed{\begin{array}{l} Do[CoDerFTerm2[i,j,k]=0,\{i,Dim\},\{j,Dim\},\{k,Dim\}] \\ Do[Do[CoDerFTerm2[i,j,k]+=\Gamma[i,k,d]gu[m,d]gu[n,j](D[A[n],x[m]]-D[A[m],x[n]]) \\ \qquad\qquad\qquad\qquad +\Gamma[j,d,k]gu[m,i]gu[n,d](D[A[n],x[m]]-D[A[m],x[n]]) \\ \qquad\qquad\qquad\qquad\qquad ,\{d,Dim\},\{m,Dim\},\{n,Dim\}],\{i,Dim\},\{j,Dim\},\{k,Dim\}] \end{array}}$$

    - $F^{ij}{}_{;k}$:

$$\boxed{Do[CoDerF[i,j,k]=CoDerFTerm1[i,j,k]+CoDerFTerm2[i,j,k],\{i,Dim\},\{j,Dim\},\{k,Dim\}]}$$

- $F^{ik}{}_{;k}$:

$$Do[MaxwellFTerm[i] = 0, \{i, Dim\}]$$
$$Do[Do[MaxwellFTerm[i] + = CoDerF[i, k, k], \{k, Dim\}], \{i, Dim\}]$$

- $Maxwell[i] = F^{ik}{}_{;k} - 4\pi j^i$:

$$Maxwell[i] = F^{ik}{}_{;k} - 4\pi j^i$$
$$Do[Maxwell[i] = MaxwellFTerm[i] - 4\pi\varepsilon\mu[\rho, \zeta]uu[i], \{i, Dim\}]$$

- Equations in Tetrad basis:

  - Tetrad transformation: $\lambda_{(j)}{}^{\hat{i}}$

$$Do[Tetrad[i, j] = 0, \{i, Dim\}, \{j, Dim\}]$$
$$Tetrad[1, 1] = \frac{1}{e\alpha[\rho,\zeta]}; \ Tetrad[1, 2] = 0; \ Tetrad[2, 2] = \frac{1}{e\alpha[\rho,\zeta]}; \ Tetrad[3, 3] = \frac{e\nu[\rho,\zeta]}{\rho};$$
$$Tetrad[3, 4] = \frac{\omega[\rho,\zeta]}{e\nu[\rho,\zeta]}; \ Tetrad[4, 4] = \frac{1}{e\nu[\rho,\zeta]};$$

  - Ricci tensor $R_{\hat{a}\hat{b}}$:

$$Do[RicciTensorTetrad[u, v] = 0, \{u, Dim\}, \{v, Dim\}]$$
$$Do[Do[RicciTensorTetrad[a, b] + = Tetrad[u, a]Tetrad[v, b]RicciTensor[u, v]$$
$$, \{u, Dim\}, \{v, Dim\}], \{a, Dim\}, \{b, Dim\}]$$

  - Ricci tensor R:

$$RicciScalarTetrad = 0;$$
$$Do[RicciScalarTetrad + = guTetrad[x, y]RicciTensorTetrad[x, y], \{x, Dim\}, \{y, Dim\}]$$

  - Energy momentum tensor $T_{\hat{a}\hat{b}}$:

$$Do[TTetrad[i, k] = 0, \{i, Dim\}, \{k, Dim\}]$$
$$Do[Do[TTetrad[a, b] + = Tetrad[i, a]Tetrad[k, b]T[i, k], \{i, Dim\}, \{k, Dim\}], \{a, Dim\}, \{b, Dim\}]$$

  - Einstein equations:

$$Do[EinsteinTetrad[i, k] = FullSimplify[RicciTensorTetrad[i, k]$$
$$- \tfrac{1}{2}(-8\pi(TTetrad[1, 1] + TTetrad[2, 2] + TTetrad[3, 3] - TTetrad[4, 4]))gdTetrad[i, k]$$
$$- 8\pi TTetrad[i, k]], \{i, Dim\}, \{k, Dim\}]$$

  - Maxwell equations:

$$Do[Maxwelldown[i] = 0, \{i, Dim\}]$$
$$Do[Do[Maxwelldown[j] + = gd[i, j]Maxwell[i], \{i, Dim\}], \{j, Dim\}]$$
$$Do[MaxwelldownTetrad[a] = 0, \{a, Dim\}]$$
$$Do[Do[MaxwelldownTetrad[a] + = Tetrad[j, a]Maxwelldown[j], \{j, Dim\}], \{a, Dim\}]$$
$$Do[MaxwelldownTetradup[i] = 0, \{i, Dim\}]$$
$$Do[Do[MaxwelldownTetradup[b] + = guTetrad[b, a]MaxwelldownTetrad[a], \{a, Dim\}], \{b, Dim\}]$$

A.2 Results

A.2.1 Obtained Directly through the Metric

The following is the result of the calculation directly through the metric. For the Ricci tensors

$$
\begin{aligned}
R_{11} &= \frac{e^{-4\nu}}{2\rho}\left\{2e^{4\nu}\left[-\rho(\alpha_{,\zeta\zeta}+\alpha_{,\rho\rho})+\alpha_{,\rho}-2{\nu_{,\rho}}^{2}\rho+2\nu_{,\rho}\right]+\rho^{3}\omega_{,\rho}^{2}\right\},\\
R_{22} &= \frac{e^{-4\nu}}{2\rho}\left\{\rho^{3}{\omega_{,\zeta}}^{2}-2e^{4\nu}\left[\rho\left(\alpha_{,\zeta\zeta}+\alpha_{,\rho\rho}+2{\nu_{,\zeta}}^{2}\right)+\alpha_{,\rho}\right]\right\},\\
R_{33} &= \frac{e^{-2(\alpha+3\nu)}\rho}{2}\left\{2e^{4\nu}\left[\rho(\nu_{,\zeta\zeta}+\nu_{,\rho\rho})+\nu_{,\rho}\right]-\rho^{3}\left({\omega_{,\zeta}}^{2}+{\omega_{,\rho}}^{2}\right)\right\},\\
R_{44} &= \frac{e^{-2(\alpha+3\nu)}}{2\rho}\Big\{2e^{8\nu}\left[\rho(\nu_{,\zeta\zeta}+\nu_{,\rho\rho})+\nu_{,\rho}\right]-\rho^{5}\omega^{2}\left(\omega_{,\zeta}^{2}+\omega_{,\rho}^{2}\right)\\
&\qquad e^{4\nu}\rho^{2}\Big[2\rho\omega\Big(\omega(\nu_{,\zeta\zeta}+\nu_{,\rho\rho})-(\omega_{,\zeta\zeta}+\omega_{,\rho\rho})\Big)\\
&\qquad +8\rho\omega\nu_{,\zeta}\omega_{,\zeta}+2\nu_{,\rho}\omega(4\rho\omega_{,\rho}+\omega)-\rho\left(\omega_{,\zeta}^{2}+\omega_{,\rho}^{2}\right)-6\omega\omega_{,\rho}\Big]\Big\},\\
R_{12} &= \frac{e^{-4\nu}}{2\rho}\left[2e^{4\nu}(\alpha_{,\zeta}-2\nu_{,\zeta}\nu_{,\rho}\rho+\nu_{,\zeta})+\rho^{3}\omega_{,\zeta}\omega_{,\rho}\right],\\
R_{13} &= R_{14}=R_{23}=R_{24}=0,\\
R_{34} &= \frac{1}{2}\rho e^{-2(\alpha+3\nu)}\Big\{\rho^{3}\omega\left(\omega_{,\zeta}^{2}+\omega_{,\rho}^{2}\right)+e^{4\nu}\Big[-2\nu_{,\rho}(2\rho\omega_{,\rho}+\omega)+3\omega_{,\rho}\\
&\qquad +\rho\Big(-4\nu_{,\zeta}\omega_{,\zeta}-2\omega(\nu_{,\zeta\zeta}+\nu_{,\rho\rho})+\omega_{,\zeta\zeta}+\omega_{,\rho\rho}\Big)\Big]\Big\}.
\end{aligned}
$$

The Ricci scalar is

$$
R=\frac{e^{-2(\alpha+2\nu)}}{2\rho}\left\{\rho^{3}\left(\omega_{,\zeta}^{2}+\omega_{,\rho}^{2}\right)-4e^{4\nu}\left[\rho\left(\alpha_{,\zeta\zeta}+\alpha_{,\rho\rho}+\nu_{,\zeta}^{2}+\nu_{,\rho}^{2}\right)-\nu_{,\rho}\right]\right\}.
$$

The energy-momentum tensors are

$$
\begin{aligned}
T_{11} &= e^{2\alpha}p + \frac{e^{-2\nu}}{8\pi\rho^2}\left\{e^{4\nu}\left(A_{\varphi,\rho}^{\,2} - A_{\varphi,\zeta}^{\,2}\right) + \rho^2\Big[A_{t,\zeta} + A_{t,\rho} + \omega(A_{\varphi,\zeta} + A_{\varphi,\rho})\Big]\Big[A_{t,\zeta} - A_{t,\rho} + \omega(A_{\varphi,\zeta} - A_{\varphi,\rho})\Big]\right\}, \\
T_{22} &= e^{2\alpha}p + \frac{e^{-2\nu}}{8\pi\rho^2}\Big\{e^{4\nu}(A_{\varphi,\zeta}^{\,2} - A_{\varphi,\rho}^{\,2}) - \rho^2\left[A_{t,\zeta} - A_{t,\rho} + \omega(A_{\varphi,\zeta} - A_{\varphi,\rho})\right]\left[A_{t,\zeta} + A_{t,\rho} + \omega(A_{\varphi,\zeta} + A_{\varphi,\rho})\right]\Big\}, \\
T_{33} &= \frac{(e^{-2\nu}\rho^2)[\mu\rho^2(\omega-\Omega)^2 + e^{4\nu}p]}{e^{4\nu} - \rho^2(\omega-\Omega)^2} + \frac{e^{-2(\alpha+2\nu)}}{8\pi}\Big\{e^{4\nu}\left(A_{\varphi,\zeta}^{\,2} + A_{\varphi,\rho}^{\,2}\right) + \rho^2\left[(A_{t,\zeta} + A_{\varphi,\zeta}\omega)^2 + (A_{t,\rho} + A_{\varphi,\rho}\omega)^2\right]\Big\}, \\
T_{44} &= \frac{e^{2\nu}\rho^2\Omega^2(\mu+p)}{e^{4\nu} - \rho^2(\omega-\Omega)^2} - \mu e^{-2\nu}\rho^2\omega^2 + \mu e^{2\nu} + \frac{e^{4\nu-2\alpha}\left(A_{\varphi,\zeta}^{\,2} + A_{\varphi,\rho}^{\,2}\right)}{8\pi\rho^2} \\
&\quad + \frac{e^{-2\alpha}}{8\pi}\Big\{e^{-4\nu}\rho^2\omega^2\left[A_{t,\zeta}^{2} + 2A_{t,\zeta}A_{\varphi,\zeta}\omega + A_{t,\rho}^{2} + 2A_{t,\rho}A_{\varphi,\rho}\omega + \omega^2\left(A_{\varphi,\zeta}^{\,2} + A_{\varphi,\rho}^{\,2}\right)\right] \\
&\qquad\quad + A_{t,\zeta}^{2} - 2A_{t,\zeta}A_{\varphi,\zeta}\omega + A_{t,\rho}^{2} - 2\omega\left[A_{t,\rho}A_{\varphi,\rho} + \omega\left(A_{\varphi,\zeta}^{\,2} + A_{\varphi,\rho}^{\,2}\right)\right]\Big\}, \\
T_{12} &= \frac{e^{-2\nu}}{4\pi\rho^2}\left[A_{\varphi,\zeta}A_{\varphi,\rho}e^{4\nu} - \rho^2(A_{t,\zeta} + A_{\varphi,\zeta}\omega)(A_{t,\rho} + A_{\varphi,\rho}\omega)\right], \\
T_{13} &= T_{14} = T_{23} = T_{24} = 0, \\
T_{34} &= e^{-2\nu}\rho^2\left[\mu\omega - \frac{e^{4\nu}\Omega(\mu+p)}{e^{4\nu} - \rho^2(\omega-\Omega)^2}\right] + \frac{e^{-2\alpha}}{8\pi}\Big\{2A_{t,\zeta}A_{\varphi,\zeta} + 2A_{t,\rho}A_{\varphi,\rho} + \omega\left(A_{\varphi,\zeta}^{\,2} + A_{\varphi,\rho}^{\,2}\right) \\
&\qquad - e^{-4\nu}\rho^2\omega\left[A_{t,\zeta}^{2} + 2A_{t,\zeta}A_{\varphi,\zeta}\omega + A_{t,\rho}^{2} + 2A_{t,\rho}A_{\varphi,\rho}\omega + \omega^2\left(A_{\varphi,\zeta}^{\,2} + A_{\varphi,\rho}^{\,2}\right)\right]\Big\}.
\end{aligned}
$$

A.2.2 Obtained via Tetrad-Basis

The Ricci tensors are obtained in the orthonormal tetrad basis as

$$
\begin{aligned}
R_{\hat{1}\hat{1}} &= e^{-2\alpha}R_{11} \\
&= \frac{e^{-2(\alpha+2\nu)}}{2\rho}\left\{2e^{4\nu}\left[-\rho(\alpha_{,\zeta\zeta} + \alpha_{,\rho\rho}) + \alpha_{,\rho} - 2\nu_{,\rho}{}^2\rho + 2\nu_{,\rho}\right] + \rho^3\omega_{,\rho}^2\right\}, \\
R_{\hat{2}\hat{2}} &= e^{-2\alpha}R_{22} \\
&= \frac{e^{-2(\alpha+2\nu)}}{2\rho}\left\{\rho^3\omega_{,\zeta}{}^2 - 2e^{4\nu}\left[\rho\left(\alpha_{,\zeta\zeta} + \alpha_{,\rho\rho} + 2\nu_{,\zeta}{}^2\right) + \alpha_{,\rho}\right]\right\}, \\
R_{\hat{3}\hat{3}} &= R_{\hat{4}\hat{4}} = \frac{e^{2\nu}}{\rho^2}R_{33} \\
&= \frac{e^{-2(\alpha+2\nu)}}{2\rho}\left\{2e^{4\nu}\left[\rho(\nu_{,\zeta\zeta} + \nu_{,\rho\rho}) + \nu_{,\rho}\right] - \rho^3\left(\omega_{,\zeta}{}^2 + \omega_{,\rho}{}^2\right)\right\}, \\
R_{\hat{1}\hat{2}} &= e^{-2\alpha}R_{12} \\
&= \frac{e^{-2(\alpha+2\nu)}}{2\rho}\left[2e^{4\nu}(\alpha_{,\zeta} - 2\nu_{,\zeta}\nu_{,\rho}\rho + \nu_{,\zeta}) + \rho^3\omega_{,\zeta}\omega_{,\rho}\right], \\
R_{\hat{1}\hat{3}} &= R_{\hat{1}\hat{4}} = R_{\hat{2}\hat{3}} = R_{\hat{2}\hat{4}} = 0, \\
R_{\hat{3}\hat{4}} &= \frac{e^{-2(\alpha+\nu)}}{2}\left[-4\nu_{,\zeta}\rho\ \omega_{,\zeta} + \rho(-4\nu_{,\rho}\omega_{,\rho} + \omega_{,\zeta\zeta} + \omega_{,\rho\rho}) + 3\omega_{,\rho}\right].
\end{aligned}
$$

The Ricci scalar is

$$R = \frac{e^{-2(\alpha+2\nu)}}{2\rho}\left\{\rho^3\left(\omega_{,\zeta}^2 + \omega_{,\rho}^2\right) - 4e^{4\nu}\left[\rho\left(\alpha_{,\zeta\zeta} + \alpha_{,\rho\rho} + \nu_{,\zeta}^2 + \nu_{,\rho}^2\right) - \nu_{,\rho}\right]\right\}.$$

Furthermore the energy-momentum tensors are

$$\begin{aligned}
T_{\hat{1}\hat{1}} &= e^{-2\alpha}T_{11}\\
&= p + \frac{e^{-2(\alpha+\nu)}}{8\pi\rho^2}\Big\{e^{4\nu}\left({A_{\varphi,\rho}}^2 - {A_{\varphi,\zeta}}^2\right) + \rho^2\Big[A_{t,\zeta} + A_{t,\rho} + \omega(A_{\varphi,\zeta} + A_{\varphi,\rho})\Big]\Big[A_{t,\zeta} - A_{t,\rho} + \omega(A_{\varphi,\zeta} - A_{\varphi,\rho})\Big]\Big\},\\
T_{\hat{2}\hat{2}} &= e^{-2\alpha}T_{22}\\
&= p + \frac{e^{-2(\alpha+\nu)}}{8\pi\rho^2}\Big\{e^{4\nu}({A_{\varphi,\zeta}}^2 - {A_{\varphi,\rho}}^2) - \rho^2\left[A_{t,\zeta} - A_{t,\rho} + \omega(A_{\varphi,\zeta} - A_{\varphi,\rho})\right]\left[A_{t,\zeta} + A_{t,\rho} + \omega(A_{\varphi,\zeta} + A_{\varphi,\rho})\right]\Big\},\\
T_{\hat{3}\hat{3}} &= \frac{e^{2\nu}}{\rho^2}T_{33}\\
&= \frac{\mu\rho^2(\omega-\Omega)^2 + e^{4\nu}p}{e^{4\nu} - \rho^2(\omega-\Omega)^2} + \frac{e^{-2(\alpha+\nu)}}{8\pi\rho^2}\Big\{\rho^2\left[(A_{t,\zeta} + A_{\varphi,\zeta}\omega)^2 + (A_{t,\rho} + A_{\varphi,\rho}\omega)^2\right] + e^{4\nu}\left({A_{\varphi,\zeta}}^2 + {A_{\varphi,\rho}}^2\right)\Big\},\\
T_{\hat{4}\hat{4}} &= \frac{\mu e^{4\nu} + p\rho^2(\omega-\Omega)^2}{e^{4\nu} - \rho^2(\omega-\Omega)^2} + \frac{e^{-2(\alpha+\nu)}}{8\pi\rho^2}\Big\{\rho^2\left[(A_{t,\zeta} + A_{\varphi,\zeta}\omega)^2 + (A_{t,\rho} + A_{\varphi,\rho}\omega)^2\right] + e^{4\nu}\left({A_{\varphi,\zeta}}^2 + {A_{\varphi,\rho}}^2\right)\Big\},\\
T_{\hat{1}\hat{2}} &= \frac{e^{2\nu}}{\rho^2}T_{12}\\
&= \frac{e^{-2(\alpha+\nu)}}{4\pi\rho^2}\left[A_{\varphi,\zeta}A_{\varphi,\rho}e^{4\nu} - \rho^2(A_{t,\zeta} + A_{\varphi,\zeta}\omega)(A_{t,\rho} + A_{\varphi,\rho}\omega)\right],\\
T_{\hat{1}\hat{3}} &= T_{\hat{1}\hat{4}} = T_{\hat{2}\hat{3}} = T_{\hat{2}\hat{4}} = 0,\\
T_{\hat{3}\hat{4}} &= \frac{e^{2\nu}\rho(\mu+p)(\omega-\Omega)}{e^{4\nu} - \rho^2(\omega-\Omega)^2} + \frac{e^{-2\alpha}}{4\pi\rho}\left[A_{t,\zeta}A_{\varphi,\zeta} + A_{t,\rho}A_{\varphi,\rho} + \omega\left({A_{\varphi,\zeta}}^2 + {A_{\varphi,\rho}}^2\right)\right].
\end{aligned}$$

It can be seen that the configurations are compacter under the tetrad basis, which is one of the reasons why it is chosen to work under the set of field equations obtained from the tetrad basis. A quick check at the Ricci scalar and it can be seen that the outcome is the same for both the calculation obtain directly from the metric and from the tetrad basis, which confirms the correctness of the results, since the Ricci scalar should be invariant of the frame of reference.

Appendix B

Detailed calculations of the boundary conditions

B.1 Pill-box integration on the disc

B.1.1 Difference between the pill-box integration and the "conventional" integration

Suppose that one wants to integrate a function $f(x)$ between $\pm\epsilon$, one has

$$\begin{aligned}\int_{-\epsilon}^{\epsilon} f(x)dx &= \int_{-\epsilon}^{0} f(x)dx + \int_{0}^{\epsilon} f(x)dx \\ &= \int_{\epsilon}^{0} f(-x)d(-x) + \int_{0}^{\epsilon} f(x)dx \\ &= -\int_{0}^{\epsilon} f(x)dx + \int_{0}^{\epsilon} f(x)dx. \qquad \text{(B.1)}\end{aligned}$$

The difference between the pill-box integration and the conventional integration can be considered to be its "integration direction". Wilst for the conventional integration

$$d(-x) = d(x),$$

for the pill-box integration it is

$$d(-x) = -d(x).$$

Thus, judging if $f(x)$ is an even or an odd function, the following cases for (B.1) are observed:

	Even funciton: $f(-x)=f(x)$	Odd funciton: $f(-x)=-f(x)$
Conventional: $d(-x)=-dx$	$=-\int_0^\epsilon f(x)[-dx]+\int_0^\epsilon f(x)dx$ $=2\int_0^\epsilon f(x)dx$	$=-\int_0^\epsilon [-f(x)][-dx]+\int_0^\epsilon f(x)dx$ $=0$
Pill-box: $d(-x)=dx$	$=-\int_0^\epsilon f(x)dx+\int_0^\epsilon f(x)dx$ $=0$	$=-\int_0^\epsilon [-f(x)][dx]+\int_0^\epsilon f(x)dx$ $=2\int_0^\epsilon f(x)dx$

B.1.2 Pill-box integration for the disc

(I) Einstein $[\hat{4},\hat{4}]$ (2.19):

$$\underbrace{4\pi e^{\alpha}\sigma_p(\rho)\delta(\zeta)\left[\frac{1+v^2}{1-v^2}\right]}_{(1)}-\underbrace{\Delta\nu}_{(2)}+\underbrace{\frac{1}{\rho^2}e^{-2\nu}\left[e^{4\nu}(\nabla A_\varphi)^2+\rho^2(\nabla A_t+\omega\nabla A_\varphi)^2\right]}_{(3)}=0.$$

- (1): With $\int_{-\infty}^{\infty}\delta(x)dx=1$,

$$\lim_{\kappa\to0}\int_{\kappa^-}^{\kappa^+}4\pi e^{\alpha}\sigma_p(\rho)\delta(\zeta)\left[\frac{1+v^2}{1-v^2}\right]d\zeta=4\pi e^{\alpha}\sigma_p(\rho)\left[\frac{1+v^2}{1-v^2}\right].$$

- (2):

$$\int_{\kappa^-}^{\kappa^+}\Delta\nu d\zeta=\int_{\kappa^-}^{\kappa^+}\left(\underbrace{\frac{\partial^2\nu}{\partial\rho^2}+\frac{1}{\rho}\frac{\partial\nu}{\partial\rho}}_{\text{even function}}+\underbrace{\frac{\partial^2\nu}{\partial\zeta^2}}_{\text{odd function}}\right)d\zeta=2\int_0^{\kappa^+}\frac{\partial^2\nu}{\partial\zeta^2}d\zeta=2\left.\frac{\partial\nu}{\partial\zeta}\right|_{\zeta=\kappa^+},$$

$$\to\qquad\lim_{\kappa\to0}2\left.\frac{\partial\nu}{\partial\zeta}\right|_{\zeta=\kappa^+}=2\frac{\partial\nu}{\partial\zeta}.$$

- (3) is an even function.

Thus the first boundary equation for the disc (2.32)[1] is obtained.

$$2\pi e^{\alpha}\sigma_p(\rho)\left[\frac{1+v^2}{1-v^2}\right]=\nu_{,\zeta}.$$

(II) Einstein $[\hat{3},\hat{4}]$ (2.20):

$$\underbrace{16\pi\rho e^{\alpha-2\nu}\sigma_p(\rho)\delta(\zeta)\frac{v}{1-v^2}}_{(1)}+\underbrace{\nabla\cdot(\rho^2+e^{-4\nu}\nabla\omega)}_{(2)}-\underbrace{4e^{-2\nu}\left[\nabla A_\varphi\nabla A_t+\omega(\nabla A_\varphi)^2\right]}_{(3)}=0$$

- (1):

$$\lim_{\kappa\to 0}\int_{\kappa^-}^{\kappa^+}16\pi\rho e^{\alpha-2\nu}\sigma_p(\rho)\delta(\zeta)\frac{v}{1-v^2}d\zeta=16\pi\rho e^{2(\alpha-\nu)}\sigma_p(\rho)\frac{v}{1-v^2}.$$

- (2):

$$\begin{aligned}\int_{\kappa^-}^{\kappa^+}\nabla\cdot(\rho^2+e^{-4\nu}\nabla\omega)d\zeta&=\int_{\kappa^-}^{\kappa^+}\left(\underbrace{\frac{1}{\rho}\frac{\partial}{\partial\rho}\left[\rho^3+e^{-4\nu}\frac{\partial\omega}{\partial\rho}\right]}_{\text{even function}}+\underbrace{\frac{\partial}{\partial\zeta}\left[\rho^2e^{-4\nu}\frac{\partial\omega}{\partial\zeta}\right]}_{\text{odd function}}\right)d\zeta\\&=2\int_0^{\kappa^+}\frac{\partial}{\partial\zeta}\left[\rho^2e^{-4\nu}\frac{\partial\omega}{\partial\zeta}\right]d\zeta=2\rho^2e^{-4\nu}\frac{\partial\omega}{\partial\zeta}\Big|_{\zeta=\kappa^+},\end{aligned}$$

$$\to\qquad\lim_{\kappa\to 0}2\rho^2e^{-4\nu}\frac{\partial\omega}{\partial\zeta}\Big|_{\zeta=\kappa^+}=2\rho^2e^{-4\nu}\frac{\partial\omega}{\partial\zeta}.$$

- (3) is an even funciton.

Thus the second boundary equation for the disc (2.33) is obtained

$$-\frac{8\pi}{\rho}e^{\alpha+2\nu}\sigma_p(\rho)\frac{v}{1-v^2}=\omega_{,\zeta}.$$

(III) Maxwell $[\hat{3}]$ (2.21):

$$\underbrace{-\frac{4e^{\alpha-3\nu}\pi\varepsilon\rho^2\sigma_p(\rho)\delta(\zeta)(\Omega-\omega)}{\sqrt{1-e^{-4\nu}\rho^2(\Omega-\omega)^2}}}_{(1)}-\underbrace{\Delta A_\varphi}_{(2)}+\underbrace{e^{-4\nu}\rho^2\left[\nabla A_t\nabla\omega+\omega(\nabla A_\varphi\nabla\omega)\right]-2\nabla A_\varphi\nabla\nu+\frac{2A_{\varphi,\rho}}{\rho}}_{(3)}=0$$

- (1):

$$\lim_{\kappa\to 0}\int_{\kappa^-}^{\kappa^+}\frac{4e^{2\alpha-3\nu}\pi\varepsilon\rho^2\sigma_p(\rho)\delta(\zeta)(\Omega-\omega)}{\sqrt{1-e^{-4\nu}\rho^2(\Omega-\omega)^2}}d\zeta=\frac{4e^{2\alpha-3\nu}\pi\varepsilon\rho^2\sigma_p(\rho)(\Omega-\omega)}{\sqrt{1-e^{-4\nu}\rho^2(\Omega-\omega)^2}}.$$

---

[1] with $v:=1+e^{-4\nu}\rho^2(\Omega-\omega)^2$.

- (2):

$$\lim_{\kappa\to 0}\int_{\kappa^-}^{\kappa^+}\Delta A_\varphi d\zeta=\lim_{\kappa\to 0}\int_{\kappa^-}^{\kappa^+}-\left(\underbrace{\frac{\partial^2 A_\varphi}{\partial\rho^2}+\frac{1}{\rho}\frac{A_\varphi}{\partial\rho}}_{\text{even function}}+\underbrace{\frac{\partial^2 A_\varphi}{\partial\zeta^2}}_{\text{odd function}}\right)d\zeta 2=\int_0^{\kappa^+}\frac{\partial^2 A_\varphi}{\partial\zeta^2}d\zeta=2\frac{\partial A_\varphi}{\partial\zeta}\bigg|_{\zeta=\kappa^+},$$

$$\rightarrow\qquad\lim_{\kappa\to 0}2\frac{\partial A_\varphi}{\partial\zeta}\bigg|_{\zeta=\kappa^+}=2\frac{\partial A_\varphi}{\partial\zeta}.$$

- (3) is an even funciton.

Thus the third boundary equation of the disc (2.34) is obtained

$$-\frac{2e^{\alpha-3\nu}\pi\varepsilon\rho^2\sigma_p(\Omega-\omega)}{\sqrt{1-e^{-4\nu}\rho^2(\Omega-\omega)^2}}=A_{\varphi,\zeta}.$$

(IV) Maxwell $[\hat{4}]$ (2.22):

$$-\underbrace{\frac{4e^{\alpha+\nu}\pi\varepsilon\sigma_p(\rho)\delta(\zeta)}{\sqrt{1-e^{-4\nu}\rho^2(\Omega-\omega)^2}}}_{(1)}+\underbrace{\Delta A_t}_{(2)}+\underbrace{\omega\Delta A_\varphi}_{(3)}-\underbrace{2\nabla A_t\nabla\nu-2\omega\nabla A_\varphi\nabla\nu+\nabla A_\varphi\nabla\omega}_{(4)}=0$$

- (1)

$$\lim_{\kappa\to 0}\int_{\kappa^-}^{\kappa^+}\frac{\frac{4e^{\alpha+\nu}\pi\varepsilon\sigma_p(\rho)\delta(\zeta)}{\sqrt{1-e^{-4\nu}\rho^2(\Omega-\omega)^2}}}{\sqrt{1-e^{-4\nu}\rho^2(\Omega-\omega)^2}}d\zeta=\frac{4e^{\alpha+\nu}\pi\varepsilon\sigma_p(\rho)}{\sqrt{1-e^{-4\nu}\rho^2(\Omega-\omega)^2}}.$$

- (2)

$$\lim_{\kappa\to 0}\int_{\kappa^-}^{\kappa^+}\Delta A_t d\zeta=\lim_{\kappa\to 0}\int_{\kappa^-}^{\kappa^+}-\left(\underbrace{\frac{\partial^2 A_t}{\partial\rho^2}+\frac{1}{\rho}\frac{A_t}{\partial\rho}}_{\text{even function}}+\underbrace{\frac{\partial^2 A_t}{\partial\zeta^2}}_{\text{odd function}}\right)d\zeta 2=\int_0^{\kappa^+}\frac{\partial^2 A_t}{\partial\zeta^2}d\zeta=2\frac{\partial A_t}{\partial\zeta}\bigg|_{\zeta=\kappa^+},$$

$$\rightarrow\qquad\lim_{\kappa\to 0}2\frac{\partial A_t}{\partial\zeta}\bigg|_{\zeta=\kappa^+}=2\frac{\partial A_t}{\partial\zeta}.$$

- (3)

$$\omega\Delta A_\varphi=\omega\underbrace{\frac{1}{\rho}\frac{\partial}{\partial\rho}\left(\rho\frac{\partial A_\varphi}{\partial\rho}\right)}_{\text{even function}}+\omega\underbrace{\frac{\partial^2 A_\varphi}{\partial\zeta^2}}_{\text{odd function}},$$

$$\lim_{\kappa\to 0}\int_{\kappa^-}^{\kappa^+}\omega\frac{\partial^2 A_\varphi}{\partial\zeta^2}d\zeta=\lim_{\kappa\to 0}\left(\omega\frac{\partial A_\varphi}{\partial\zeta}\bigg|_{\kappa^-}^{\kappa^+}-\int_{\kappa^-}^{\kappa^+}\frac{\partial\omega}{\partial\zeta}\frac{\partial A_\varphi}{\partial\zeta}d\zeta\right)=2\omega\frac{\partial A_\varphi}{\delta\zeta}.$$

- (4) is an even funciton.

Thus the forth boundary equation of the disc (2.35) is obtained

$$\frac{2e^{\alpha+\nu}\pi\varepsilon\sigma_p}{\sqrt{1-e^{-4\nu}\rho^2(\Omega-\omega)^2}} = A_{t,\zeta} + \omega A_{\varphi,\zeta}.$$

(V) Trace equation $R^{\hat{i}}{}_{\hat{i}} + 8\pi T^{\hat{i}}{}_{\hat{i}} = 0$ (2.29):

$$\underbrace{8\pi e^{-\alpha}\sigma_p(\rho)\delta(\zeta)}_{(1)} - \frac{1}{2\rho}e^{-2\alpha-4\nu}\{\underbrace{\rho^3\left[\omega_{,\rho}{}^2+\omega_{,\zeta}{}^2\right] - 4e^{4\nu}[-\nu_{,\rho}+\rho\left(\nu_{,\rho}{}^2+\nu_{,\zeta}{}^2+\alpha_{,\rho\rho}\right.}_{(2)} + \underbrace{\alpha_{,\zeta\zeta}}_{(3)}]\} = 0.$$

- (1)

$$\lim_{\kappa\to 0}\int_{\kappa^-}^{\kappa^+} 8\pi e^{-\alpha}\sigma_p(\rho)\delta(\zeta)d\zeta = 8\pi e^{-\alpha}\sigma_p(\rho).$$

- (2) is an even function.
- (3)

$$\lim_{\kappa\to 0}\int_{\kappa_-}^{\kappa^+} 2e^{-2\alpha}\frac{\partial^2\alpha}{\partial\zeta^2}d\zeta = \lim_{\kappa\to 0}\left(2e^{-2\alpha}\frac{\partial\alpha}{\partial\zeta}\bigg|_{\kappa_-}^{\kappa^+} - \int_{\kappa_-}^{\kappa^+}\underbrace{2\frac{\partial e^{-2\alpha}}{\partial\zeta}\frac{\partial\alpha}{\partial\zeta}}_{\text{even funciton}}d\zeta\right) = 4e^{-2\alpha}\frac{\partial\alpha}{\partial\zeta}.$$

Thus, the forth boundary equation of the disc (2.36) is obtained

$$2\pi e^{\alpha}\sigma_p = \alpha_{,\zeta}.$$

Appendix C

Potential and coordinate transformation

C.1 Potential transformation

The aim is to transform the potentials according to that of section 3.2.1

$$\tilde{\nu} := e^{\nu}, \qquad \tilde{\alpha} := e^{\alpha}, \qquad \tilde{\omega} := \frac{\rho_0}{e^{\nu_c}}\omega, \qquad \tilde{A}_t := \frac{\rho_0}{e^{\nu_c}}A_t.$$

C.1.1 For $\tilde{\nu}$ and $\tilde{\alpha}$

With

$$\tilde{\nu} = e^{\nu},$$

the derivatives are

$$\tilde{\nu}_{,\rho} = e^{\nu}\nu_{,\rho}, \qquad \tilde{\nu}_{,\rho\rho} = e^{\nu}\left(\nu_{,\rho\rho} + \nu_{,\rho}^2\right), \qquad \tilde{\nu}_{,\zeta} = e^{\nu}\nu_{,\zeta}, \qquad \tilde{\nu}_{,\zeta\zeta} = e^{\nu}\left(\nu_{,\zeta\zeta} + \nu_{,\zeta}^2\right).$$

Reforming all 5 equations,

$$\nu_{,\rho} = \frac{\tilde{\nu}_{,\rho}}{\tilde{\nu}}, \qquad \nu_{,\rho\rho} = \frac{\tilde{\nu}\tilde{\nu}_{,\rho\rho} - \tilde{\nu}_{\rho}^2}{\tilde{\nu}}, \qquad \nu_{,\zeta} = \frac{\tilde{\nu}_{,\zeta}}{\tilde{\nu}}, \qquad \nu_{,\zeta\zeta} = \frac{\tilde{\nu}\tilde{\nu}_{,\zeta\zeta} - \tilde{\nu}_{\zeta}^2}{\tilde{\nu}}$$

are obtained. The same applies for $\tilde{\alpha}$.

C.1.2 For $\tilde{\omega}$ and $\tilde{A}_t$

With

$$\tilde{\omega} = \frac{\rho_0}{e^{\nu_c}}\omega,$$

the derivatives are

$$\tilde{\omega}_{,\rho} = \frac{\rho_0}{e^{\nu_c}}\omega_{,\rho}, \qquad \tilde{\omega}_{,\rho\rho} = \frac{\rho_0}{e^{\nu_c}}\omega_{,\rho\rho}, \qquad \tilde{\omega}_{,\zeta} = \frac{\rho_0}{e^{\nu_c}}\omega_{,\zeta}, \qquad \tilde{\omega}_{,\zeta\zeta} = \frac{\rho_0}{e^{\nu_c}}\omega_{,\zeta\zeta},$$

which gives

$$\omega_{,\rho} = \frac{e^{\nu^c}}{\rho_0}\tilde{\omega}_{,\rho}, \qquad \omega_{,\rho\rho} = \frac{e^{\nu^c}}{\rho_0}\tilde{\omega}_{,\rho\rho}, \qquad \omega_{,\zeta} = \frac{e^{\nu^c}}{\rho_0}\tilde{\omega}_{,\zeta}, \qquad \omega_{,\zeta\zeta} = \frac{e^{\nu^c}}{\rho_0}\tilde{\omega}_{,\zeta\zeta}.$$

The same applies for $\tilde{A}_t$.

C.2 Coordinate transformation

The relationship between the Weyl coordinates and spectral coordinates are as discussed in section 3.1.2

$$\rho = \frac{\rho_0\sqrt{1-\tau}}{\cos\left(\frac{\pi}{2}\sigma\right)}, \qquad \zeta = \rho_0\sqrt{\tau}\tan\left(\frac{\pi}{2}\sigma\right).$$

The first derivatives are thus

$$\begin{pmatrix} \frac{\partial F}{\partial \rho} \\ \\ \frac{\partial F}{\partial \zeta} \end{pmatrix} = \begin{pmatrix} \frac{\partial \sigma}{\partial \rho} & \frac{\partial \tau}{\partial \rho} \\ \\ \frac{\partial \sigma}{\partial \zeta} & \frac{\partial \tau}{\partial \zeta} \end{pmatrix} \begin{pmatrix} \frac{\partial F}{\partial \sigma} \\ \\ \frac{\partial F}{\partial \tau} \end{pmatrix},$$

with

$$\begin{aligned}
\frac{\partial \sigma}{\partial \rho} &= \frac{2\cos\left(\frac{\pi\sigma}{2}\right)\cot\left(\frac{\pi\sigma}{2}\right)}{\pi\rho_0\sqrt{1-\tau}}, \\
\frac{\partial \tau}{\partial \rho} &= -\frac{2\sqrt{1-\tau}\cos\left(\frac{\pi\sigma}{2}\right)}{\rho_0}, \\
\frac{\partial \sigma}{\partial \zeta} &= \frac{2\cos^2\left(\frac{\pi\sigma}{2}\right)}{\pi\rho_0\sqrt{\tau}}, \\
\frac{\partial \tau}{\partial \zeta} &= \frac{2\sqrt{\tau}\cot\left(\frac{\pi\sigma}{2}\right)}{\rho_0},
\end{aligned}$$

which gives[1]

$$f_{,\rho} = \frac{2\sqrt{1-\tau}\cos\left(\frac{\pi\sigma}{2}\right)\left[\sin(\pi\sigma) f_{,\sigma} - 2\pi\tau f_{,\tau}\right]}{\pi\rho_0\left[(\tau-1)\cos(\pi\sigma)+\tau+1\right]},$$

$$f_{,\zeta} = \frac{2\sqrt{\tau}\left[\left(\cos(\pi\sigma)+1\right) f_{,\sigma} - \left(\pi(\tau-1)\sin(\pi\sigma)\right) f_{,\tau}\right]}{\pi\rho_0\left[(\tau-1)\cos(\pi\sigma)+\tau+1\right]},$$

$$\begin{aligned}
f_{,\rho\rho} = {} & \frac{-\cos^2\left(\frac{\pi\sigma}{2}\right)}{\pi^2\rho_0^2\left[1+\tau+(-1+\tau)\cos(\pi\sigma)\right]^3} \\
& \cdot\Big\{\pi\sin(\pi\sigma)\left[8\left(\tau^2-1\right)\cos(\pi\sigma)+(\tau-1)^2\cos(2\pi\sigma)+7\tau^2-22\tau+7\right] f_{,\sigma} \\
& \quad + 2\pi^2\tau\left[4\left(\tau^2-4\tau+3\right)\cos(\pi\sigma)+(\tau-1)^2\cos(2\pi\sigma)+3\tau^2+18\tau-13\right] f_{,\tau}, \\
& \quad + 4(\tau-1)\left[(\tau-1)\cos(\pi\sigma)+\tau+1\right]\sin(\pi\sigma)\left[-4\pi\tau f_{,\sigma\tau}+\sin(\pi\sigma) f_{,\rho\rho}\right] \\
& \quad + 16\pi^2(\tau-1)\tau^2\left[(\tau-1)\cos(\pi\sigma)+\tau+1\right] f_{,\tau\tau}\Big\},
\end{aligned}$$

$$\begin{aligned}
f_{,\zeta\zeta} = {} & \frac{-2\cos^2\left(\frac{\pi\sigma}{2}\right)}{\pi^2\rho_0^2\left[1+\tau+(-1+\tau)\cos(\pi\sigma)\right]^3} \\
& \cdot\Big\{-2\pi\sin(\pi\sigma)\left[\left(\tau^2-1\right)\cos(\pi\sigma)+\tau^2-6\tau+1\right] f_{,\sigma} \\
& \quad + \pi^2(\tau-1)\left[4\left(\tau^2+4\tau-1\right)\cos(\pi\sigma)+(\tau-1)^2\cos(2\pi\sigma)+3\tau^2-14\tau+3\right] f_{,\tau} \\
& \quad + 8\pi\sin(\pi\sigma)(\tau-1)\tau\left[(\tau-1)\cos(\pi\sigma)+\tau+1\right] f_{,\sigma\tau} \\
& \quad - 8\tau\cos^2\left(\frac{\pi\sigma}{2}\right)\left[(\tau-1)\cos(\pi\sigma)+\tau+1\right] f_{,\sigma\sigma} \\
& \quad - 8\pi^2\sin^2\left(\frac{\pi\sigma}{2}\right)(\tau-1)^2\tau\left[(\tau-1)\cos(\pi\sigma)+\tau+1\right] f_{,\tau\tau}\Big\},
\end{aligned}$$

$$\begin{aligned}
f_{,\rho\zeta} = {} & \frac{4\sqrt{(1-\tau)\tau}\cos\left(\frac{\pi\sigma}{2}\right)}{\pi^2\rho_0^2\left[1+\tau+(-1+\tau)\cos(\pi\sigma)\right]^3} \\
& \cdot\Big\{2\pi\cos^2\left(\frac{\pi\sigma}{2}\right)\left[(\tau+3)\cos(\pi\sigma)+\tau-3\right] f_{,\sigma} \\
& \quad + 2\pi^2\sin(\pi\sigma)\left[-(\tau-1)\cos(\pi\sigma)+3\tau-1\right] f_{,\tau} \\
& \quad + \pi\cos^2\left(\frac{\pi\sigma}{2}\right)\left[-4(\tau-1)^2\cos(\pi\sigma)+(\tau-1)^2\cos(2\pi\sigma)-5\tau^2-6\tau+3\right] f_{,\sigma\tau} \\
& \quad + 4\cos^3\left(\frac{\pi\sigma}{2}\right)\sin\left(\frac{\pi\sigma}{2}\right)\left[(\tau-1)\cos(\pi\sigma)+\tau+1\right] f_{,\sigma\sigma} \\
& \quad + 2\pi^2\sin(\pi\sigma)(\tau-1)\tau\left[(\tau-1)\cos(\pi\sigma)+\tau+1\right] f_{,\tau\tau}\Big\}.
\end{aligned}$$

---

[1] With f representing a function.

Appendix D

Table of the data points of the appearance of the ergosphere

γ	ε	γ	ε	γ	ε	γ	ε	γ	ε	γ	ε
0.585	0.000	0.607	0.343	0.629	0.475	0.651	0.569	0.673	0.644	0.695	0.704
0.586	0.704	0.608	0.351	0.630	0.480	0.652	0.573	0.674	0.647	0.696	0.707
0.587	0.105	0.609	0.358	0.631	0.485	0.653	0.577	0.675	0.650	0.697	0.709
0.588	0.129	0.610	0.365	0.632	0.489	0.654	0.580	0.676	0.653	0.698	0.712
0.589	0.149	0.611	0.372	0.633	0.494	0.655	0.584	0.677	0.655	0.699	0.714
0.590	0.166	0.612	0.378	0.634	0.499	0.656	0.588	0.678	0.658	0.700	0.717
0.591	0.182	0.613	0.385	0.635	0.503	0.657	0.591	0.679	0.661	0.701	0.719
0.592	0.195	0.614	0.391	0.636	0.508	0.658	0.595	0.680	0.664	0.702	0.722
0.593	0.210	0.615	0.398	0.637	0.512	0.659	0.598	0.681	0.667	0.703	0.724
0.594	0.222	0.616	0.404	0.638	0.517	0.660	0.602	0.682	0.670	0.704	0.726
0.595	0.234	0.617	0.410	0.639	0.521	0.661	0.605	0.683	0.673	0.705	0.729
0.596	0.245	0.618	0.416	0.640	0.525	0.662	0.608	0.684	0.675	0.706	0.731
0.597	0.256	0.619	0.422	0.641	0.530	0.663	0.612	0.685	0.678	0.707	0.733
0.598	0.266	0.620	0.4 27	0.642	0.534	0.664	0.615	0.686	0.681	0.708	0.736
0.599	0.276	0.621	0.433	0.643	0.538	0.665	0.618	0.687	0.684	0.709	0.738
0.600	0.285	0.622	0.439	0.644	0.542	0.666	0.622	0.688	0.686	0.710	0.740
0.601	0.294	0.623	0.444	0.645	0.546	0.667	0.625	0.689	0.689	0.711	0.743
0.602	0.303	0.624	0.449	0.646	0.550	0.668	0.628	0.690	0.692	0.712	0.745
0.603	0.312	0.625	0.455	0.647	0.554	0.669	0.631	0.691	0.694	0.713	0.747
0.604	0.320	0.626	0.460	0.648	0.558	0.670	0.634	0.692	0.697	0.714	0.749
0.605	0.328	0.627	0.465	0.649	0.562	0.671	0.637	0.693	0.699	0.715	0.751
0.606	0.336	0.628	0.470	0.650	0.566	0.672	0.641	0.694	0.702	0.716	0.754

γ	ε	γ	ε	γ	ε	γ	ε	γ	ε	γ	ε
0.717	0.756	0.761	0.837	0.805	0.897	0.849	0.940	0.893	0.971	0.937	0.990
0.718	0.758	0.762	0.838	0.806	0.898	0.850	0.941	0.894	0.972	0.938	0.990
0.719	0.760	0.763	0.840	0.807	0.899	0.851	0.942	0.895	0.972	0.939	0.991
0.720	0.762	0.764	0.841	0.808	0.900	0.852	0.943	0.896	0.973	0.940	0.991
0.721	0.764	0.765	0.843	0.809	0.901	0.853	0.944	0.897	0.973	0.941	0.991
0.722	0.766	0.766	0.844	0.810	0.902	0.854	0.945	0.898	0.974	0.942	0.991
0.723	0.768	0.767	0.846	0.811	0.904	0.855	0.945	0.899	0.974	0.943	0.992
0.724	0.770	0.768	0.848	0.812	0.905	0.856	0.946	0.900	0.975	0.944	0.992
0.725	0.772	0.769	0.849	0.813	0.906	0.857	0.947	0.901	0.975	0.945	0.992
0.726	0.774	0.770	0.850	0.814	0.907	0.858	0.948	0.902	0.976	0.946	0.993
0.727	0.776	0.771	0.852	0.815	0.908	0.859	0.948	0.903	0.976	0.947	0.993
0.728	0.778	0.772	0.853	0.816	0.909	0.860	0.949	0.904	0.977	0.948	0.993
0.729	0.780	0.773	0.855	0.817	0.910	0.861	0.950	0.905	0.977	0.949	0.993
0.730	0.782	0.774	0.856	0.818	0.911	0.862	0.951	0.906	0.978	0.950	0.994
0.731	0.784	0.775	0.858	0.819	0.912	0.863	0.952	0.907	0.978	0.951	0.994
0.732	0.786	0.776	0.859	0.820	0.913	0.864	0.952	0.908	0.979	0.952	0.994
0.733	0.788	0.777	0.861	0.821	0.914	0.865	0.953	0.909	0.979	0.953	0.994
0.734	0.790	0.778	0.862	0.822	0.915	0.866	0.954	0.910	0.980	0.954	0.994
0.735	0.792	0.779	0.863	0.823	0.916	0.867	0.954	0.911	0.980	0.955	0.995
0.736	0.794	0.780	0.865	0.824	0.917	0.868	0.955	0.912	0.981	0.956	0.995
0.737	0.796	0.781	0.866	0.825	0.918	0.869	0.956	0.913	0.981	0.957	0.995
0.738	0.797	0.782	0.868	0.826	0.919	0.870	0.957	0.914	0.981	0.958	0.995
0.739	0.799	0.783	0.869	0.827	0.920	0.871	0.957	0.915	0.982	0.959	0.996
0.740	0.801	0.784	0.870	0.828	0.921	0.872	0.958	0.916	0.982	0.960	0.996
0.741	0.803	0.785	0.872	0.829	0.922	0.873	0.959	0.917	0.983	0.961	0.996
0.742	0.805	0.786	0.873	0.830	0.923	0.874	0.959	0.918	0.983	0.962	0.996
0.743	0.807	0.787	0.874	0.831	0.924	0.875	0.960	0.919	0.983	0.963	0.996
0.744	0.808	0.788	0.876	0.832	0.925	0.876	0.961	0.920	0.984	0.964	0.996
0.745	0.810	0.789	0.877	0.833	0.926	0.877	0.961	0.921	0.984	0.965	0.997
0.746	0.812	0.790	0.878	0.834	0.927	0.878	0.962	0.922	0.985	0.966	0.997
0.747	0.814	0.791	0.880	0.835	0.928	0.879	0.963	0.923	0.985	0.967	0.997
0.748	0.815	0.792	0.881	0.836	0.929	0.880	0.963	0.924	0.985	0.968	0.997
0.749	0.817	0.793	0.882	0.837	0.930	0.881	0.964	0.925	0.986	0.969	0.997
0.750	0.819	0.794	0.883	0.838	0.931	0.882	0.964	0.926	0.986	0.970	0.997
0.751	0.820	0.795	0.885	0.839	0.932	0.883	0.965	0.927	0.987	0.971	0.998
0.752	0.822	0.796	0.886	0.840	0.933	0.884	0.966	0.928	0.987	0.972	0.998
0.753	0.824	0.797	0.887	0.841	0.934	0.885	0.966	0.929	0.987	0.973	0.998
0.754	0.825	0.798	0.888	0.842	0.934	0.886	0.967	0.930	0.988	0.974	0.998
0.755	0.827	0.799	0.890	0.843	0.935	0.887	0.968	0.931	0.988	0.975	0.998
0.756	0.829	0.800	0.891	0.844	0.936	0.888	0.968	0.932	0.988	0.976	0.998
0.757	0.830	0.801	0.892	0.845	0.937	0.889	0.969	0.933	0.989	0.977	0.998
0.758	0.832	0.802	0.893	0.846	0.938	0.890	0.968	0.934	0.989	0.978	0.998
0.759	0.834	0.803	0.894	0.847	0.939	0.891	0.970	0.935	0.989	0.979	0.998
0.760	0.835	0.804	0.895	0.848	0.940	0.892	0.970	0.936	0.990	0.980	0.999

Bibliography

[1] J. M. Bardeen and R. V. Wagoner. Uniformly Rotating Disks in General Relativity. , 158:L65, November 1969.

[2] J. M. Bardeen and R. V. Wagoner. Relativistic Disks. I. Uniform Rotation. *The Astrophysical Journal*, 167:359, August 1971.

[3] G. Neugebauer and R. Meinel. The Einsteinian gravitational field of the rigidly rotating disk of dust. , 414:L97–L99, September 1993.

[4] G. Neugebauer and R. Meinel. General relativistic gravitational field of a rigidly rotating disk of dust: Axis potential, disk metric, and surface mass density. *Phys. Rev. Lett.*, 73:2166–2168, Oct 1994.

[5] R. Meinel and G. Neugebauer. Asymptotically flat solutions to the ernst equation with reflection symmetry. *Classical and Quantum Gravity*, 12(8):2045, 1995.

[6] G. Neugebauer and R. Meinel. General relativistic gravitational field of a rigidly rotating disk of dust: Solution in terms of ultraelliptic functions. *Phys. Rev. Lett.*, 75:3046–3047, Oct 1995.

[7] G. Neugebauer, A. Kleinwachter, and R. Meinel. Relativistically rotating dust. *Helv. Phys. Acta*, 69(4):472, 1996.

[8] M. Ansorg. Timelike geodesic motions within the general relativistic gravitational field of the rigidly rotating disk of dust. *Journal of Mathematical Physics*, 39:5984–6000, November 1998.

[9] M. Ansorg and R. Meinel. Differentially Rotating Disks of Dust. *General Relativity and Gravitation*, 32:1365–1380, July 2000.

[10] M. Ansorg. Differentially Rotating Disks of Dust: Arbitrary Rotation Law. *General Relativity and Gravitation*, 33:309–338, February 2001.

[11] A. Kleinwächter, H. Labranche, and R. Meinel. On the black hole limit of rotating discs and rings. *General Relativity and Gravitation*, 43:1469–1486, May 2011.

[12] D. Petroff and R. Meinel. Post-Newtonian approximation of the rigidly rotating disc of dust to arbitrary order. , 63(6):064012, March 2001.

[13] A. Kleinwächter, R. Meinel, and G. Neugebauer. The multipole moments of the rigidly rotating disk of dust in general relativity. *Physics Letters A*, 200:82–86, February 1995.

[14] S. Palenta and R. Meinel. Post-newtonian expansion of a rigidly rotating disc of dust with a constant specific charge. *Classical and Quantum Gravity*, 30(8):085010, 2013.

[15] M. Breithaupt, Y.-C. Liu, R. Meinel, and S. Palenta. On the black hole limit of rotating discs of charged dust. *Classical and Quantum Gravity*, 32(13):135022, 2015.

[16] R. Meinel and A. Kleinwächter. Dragging effects near a rigidly rotating disk of dust. *Einstein Studies*, 6:339–346, 1995.

[17] Y.-C. Liu Pynn, R. Panosso Macedo, M. Breithaupt, S. Palenta, and R. Meinel. Gyromagnetic factor of rotating disks of electrically charged dust in general relativity. *Phys. Rev. D*, 94:104035, Nov 2016.

[18] T. Lewis. Some special solutions of the equations of axially symmetric gravitational fields. *Proceedings of the Royal Society of London A: Mathematical, Physical and Engineering Sciences*, 136(829):176–192, 1932.

[19] A. Papapetrou. Champs gravitationnels stationnaires à symétrie axiale. *Annales de l'I.H.P. Physique théorique*, 4(2):83–105, 1966.

[20] F. J. Ernst. New formulation of the axially symmetric gravitational field problem. *Phys. Rev.*, 167:1175–1178, Mar 1968.

[21] F. J. Ernst. New formulation of the axially symmetric gravitational field problem. ii. *Phys. Rev.*, 168:1415–1417, Apr 1968.

[22] D. Kramer and G. Neugebauer. Zu axialsymmetrischen stationären lösungen der einsteinschen feldgleichungen für das vakuum. *Comm. Math. Phys.*, 10(2):132–139, 1968.

[23] R. Meinel, M. Breithaupt, and Y.-C. Liu. Black holes and quasiblack holes in einstein-maxwell theory. In *Proceedings, 13th Marcel Grossmann Meeting on Recent Developments in Theoretical and Experimental General Relativity, Astrophysics, and Relativistic Field Theories (MG13): Stockholm, Sweden, July 1-7, 2012*, pages 1186–1188, 2015.

[24] R. Meinel. Constructive proof of the kerr-newman black hole uniqueness including the extreme case. *Classical and Quantum Gravity*, 29(3):035004, 2012.

[25] R. Meinel and M. Hütten. On the black hole limit of electrically counterpoised dust configurations. *Classical and Quantum Gravity*, 28(22):225010, 2011.

[26] M. Ansorg. Lecture notes on spectral methods. *Theoretisch-Physikalisches Institut, Friedrich-Schiller-Universität Jena*, 2013.

[27] M. Kalisch. Pseudo-spektrale berechnung der gravitationsfelder differentiell rotierender staubscheiben in der einstein'schen theorie. *Master Thesis, Theoretisch-Physikalisches Institut, Friedrich-Schiller-Universität, Jena*, 2014.

[28] H. A. van der Vorst. Bi-cgstab: A fast and smoothly converging variant of bi-cg for the solution of nonsymmetric linear systems. *SIAM Journal on Scientific and Statistical Computing*, 13(2):631–644, 1992.

[29] R. Meinel, M. Ansorg, A. Kleinwächter, G. Neugebauer, and D. Petroff. *Relativistic Figures of Equilibrium.* Cambridge University Press, 2012.

[30] L. D. Landau and E. M. Lifshitz. *The Classical Theory of Fields, Course of Theoretical Physics, Volume 2.* Elsevier Butterworth-Heinemann, Oxford, 2004.

[31] B. Povh, K. Rith, C. Scholz, and F. Zetsche. *Particles and Nuclei.* Springer-Verlag Berlin Heidelberg, 2002.

[32] G. Gabrielse and D. Hanneke. Precision pins down the electron's magnetism. *CERN Courier.*, 46:35–37, 2013.

[33] C. Reina and A. Treves. Gyromagnetic ratio of einstein-maxwell fields. *Phys. Rev. D*, 11:3031–3032, May 1975.

[34] B. Carter. Global structure of the kerr family of gravitational fields. *Phys. Rev.*, 174:1559–1571, Oct 1968.

[35] J. M. Cohen, J. Tiomno, and R. M. Wald. Gyromagnetic ratio of a massive body. *Phys. Rev. D*, 7:998–1001, Feb 1973.

[36] C. Briggs, J. M. Cohen, G. L. DeWoolfson, and L. S. Kegeles. Slowly rotating bodies with arbitrary charge in general relativity. *Phys. Rev. D*, 23:1235–1243, Mar 1981.

[37] E. Mustafa, Jeffrey M. Cohen, and Kay R. Pechenick. Angular momentum, magnetic moment, andg-factor in general relativity. *International Journal of Theoretical Physics*, 26(12):1189–1217, 1987.

[38] H. Pfister and M. King. Rotating charged mass shell: Dragging, antidragging, and the gyromagnetic ratio. *Phys. Rev. D*, 65:084033, Apr 2002.

[39] B. K. Harrison. New solutions of the einstein-maxwell equations from old. *J. Math. Phys.*, 9(11):1744–1752, 1968.

[40] G. Neugebauer and D. Kramer. A method for the construction of stationary einstein-maxwell fields. (in german). *Annalen Phys.*, 24:62–71, 1969.

[41] G. Neugebauer. Gravitostatics and rotating bodies. *Gerneral Relativity (London, SUSSP Publications and Institute of Physics Publishing)*, pages 61–81, 1996.

Ehrenwörtliche Erklärung

Ich erkläre hiermit ehrenwörtlich, dass ich die vorliegende Arbeit selbstständig, ohne unzulässige Hilfe Dritter und ohne Benutzung andere als der angegebenen Hilfsmittel und Literatur angefertigt habe. Die aus andere Quellen direkt oder indirekt übernommenen Daten und Konzepte sind unter Angabe der Quelle gekennzeichnet.

Die Arbeit wurde bisher weder im In- noch im Ausland in gleicher oder ähnlicher Form einer anderen Prüfungsbehörde vorgelegt.

Die geltende Promotionsordnung der Physikalisch-Astronomischen Fakultät ist mir bekannt.

Ich versichere eherenwörtlich, dass ich nach bestem Wissen die reine Wahrheit gesagt und nichts verschwiegen habe.

Ort, Datum	Yu-Chun Pynn (geb. Liu)

Acknowledgements

I would like to thank my supervisor Prof. Dr. Reinhard Meinel for giving me the opportunity to work in the group and on such an interesting topic. I'm particularly grateful for his patience and guidance on the direction of the work. A huge thanks to Dr. Rodrigo Panosso Marcedo for giving me so much of his valuable time and effort in teaching me and discussing with me. Apart from his technical competencies, Dr. Marcedo has been a really encouraging force and support. I would like to thank my office mates Dr. Martin Breithaupt, Dr. Stefan Palenta and Dr. Andreas Schoepe for a nice working environment and making life in the office enjoyable. I would like to express my sincere gratitude to the late Prof. Dr. Marcus Ansorg for introducing me to the spectral-method, which is a vital tool for the thesis. I would to thank Dr. Michael Kalisch for useful discussions when starting out on the topic. I would also like to thank my husband Dr. Christopher Pynn for his support and proofreading the manuscript. A big thank you also to Christiane Schmalzl for proofreading the German translations of the work. Sincere thanks goes to the countless family members and friends that stood by me through the good and the bad times, you know who you are. I would also like to thank the referees Dr. habil. David Petroff, Prof. Dr. Wilhelm Kley and Prof. Dr. Thomas Wolf for their time and trouble in reviewing this work.

As a christian, my deepest thanks goes to Jesus Christ my saviour and provider, without whom this work would not have been possible.

This work was financed by DFG Graduate Academy, Research training group (1523/1) Quantum and Gravitational field, G3: Axisymmetric gravitational fields and Ministry of Education, Taiwan, under the program "Government Scholarship to Study Abroad (GSSA)."

Publications

Publications:

- Y.-C. Liu Pynn, R. Panosso Macedo, M. Breithaupt, S. Palenta, R. Meinel. *Gyromagnetic factor of rotating disks of electrically charged dust in general relativity*, Phys. Rev. D 94, 104035, 2016.
- M. Breithaupt, Y.-C. Liu, R. Meinel, S. Palenta. *On the black hole limit of rotating discs of charged dust*, Class.Quant.Grav.32:135022, 2015.
- R. Meinel, M. Breithaupt, Y.-C. Liu. *Black holes and quasiblack holes in Einstein-Maxwell theory*, Proceedings of the Thirteenth Marcel Grossmann Meeting on General Relativity, Singapore: World Scientific, p.1186-1188, 2015.
- R. A. Konoplya, Y.-C. Liu. *Motion of charged particles and quasinormal modes around the magnetically and tidally deformed black hole*, Phys.Rev. D86, 084007, 2012.